

**Precisely-Controlled Synthesis of Mesoporous Pt
Particles and Films with Various Nanoarchitectures**

Hongjing WANG

王 鴻靜

**Waseda University
Graduate School of
Advanced Science and Engineering
Major in Nanoscience and Nanoengineering
Research on Synthetic Chemistry of Nanomaterials**

July, 2012

Preface

Since the discovery of mesoporous materials in the early 1990s, various types of mesoporous materials have been synthesized under different conditions. Among the many framework compositions, mesoporous metals hold promise for a wide range of potential applications, such as in electronic devices, magnetic recording media, and metal catalysts, owing to their metallic frameworks. Although several approaches have been reported for the preparation of mesoporous/mesostructured metals, the lack of the controllability in the particle sizes and morphological shapes is serious problem for further development of mesoporous metals.

This dissertation focused on the development and evaluation of synthetic routes for mesoporous metals. Chapter 1 describes the background of this thesis by showing the overview of Pt-based meso/nanoporous materials and reviewing the previous synthetic approaches. Chapter 2, 3 and 4 demonstrate the use of hard-templating approach. Chapter 2 describes the preparation of mesoporous Co_3O_4 particles by using mesoporous silica KIT-6 as hard-template. Chapter 3 demonstrates synthesis of ordered mesoporous Pt nanoparticles with uniform rhombic dodecahedral shape and controllable particle size. Chapter 4 describes the extend concept for synthesizing well-ordered mesoporous Pt nanoparticles with uniform olive shapes by using two-dimensional (2D) hexagonal mesoporous silica (SBA-15) as a hard-template. Chapter 5, 6, and 7 demonstrate the development of soft-templating approach for dendritic Pt particles and mesoporous Pt films. Chapter 5 demonstrates a facile synthesis of three-dimensional (3D) branched platinum Nanoclusters with high surface area, by using simple microwave-assisted heat-treatment of an aqueous solution. Chapter 6 describes a new concept of “electrochemical micelle assembly” for synthesis of mesoporous Pt film by a simple electrodeposition method in an aqueous surfactant solution. Chapter 7 demonstrates the extended concept to synthesize mesoporous Pt-Pd and Pt-Ru alloy films with enhanced electrochemical performance for methanol electrooxidation. Chapter 8 describes general conclusions of this thesis and future prospects.

- Contents -

Chapter 1	1
<i>General Introduction</i>	
1.1. Introduction	2
1.1.1. Mesoporous Materials	2
1.1.2. Mesoporous Metals	3
1.2. General Synthetic Pathways for Mesoporous Materials	4
1.2.1. Soft-Templating Method	4
1.2.2. Hard-Templating Method	10
1.2.3. Other Methods	12
1.3. Potential Applications of Mesoporous Metals	13
1.3.1. Direct Methanol Fuel Cells (DMFCs)	14
1.3.2. Clean Energy Production and Storage	15
1.3.3. Optical Applications	16
1.3.4. Biomedical Applications	17
References	19
Chapter 2	26
<i>Synthesis of Mesoporous Co₃O₄ for Low Temperature CO Oxidation</i>	
2.1. Introduction	27
2.2. Experimental Process	30
2.2.1. Preparation of Mesoporous Silica KIT-6	30
2.2.2. Preparation of Mesoporous Co₃O₄	30
2.2.3. Measurement of Catalytic Activity	31
2.2.4. Characterizations	31

2.3.	<i>Results and Discussion</i>	32
2.3.1.	Synthesis and Characterization of Mesoporous Co_3O_4	32
2.3.2.	Catalytic Activity of Mesoporous Co_3O_4	39
2.4.	<i>Conclusion</i>	43
	<i>References</i>	44

Chapter 3	47
-----------	-------	----

Shape- and Size-Controlled Synthesis in Hard Templates: Sophisticated Chemical Reduction for Mesoporous Monocrystalline Platinum Nanoparticles

3.1.	<i>Introduction</i>	48
3.2.	<i>Experimental Process</i>	49
3.2.1.	Synthesis of mesoporous silica KIT-6	49
3.2.2.	Preparation of mesoporous Pt nanoparticles (<i>meso</i> -Pt).....	50
3.2.3.	Characterization	50
3.3.	<i>Results and Discussion</i>	51
3.4.	<i>Conclusion</i>	67
	<i>References</i>	68

Chapter 4	71
-----------	-------	----

Synthesis of Olive-Shaped Mesoporous Platinum Nanoparticles with Hard-Templating Method Using Mesoporous Silica (SBA-15)

4.1.	<i>Introduction</i>	72
4.2.	<i>Experimental Process</i>	75
4.2.1.	Synthesis of mesoporous silica SBA-15.....	75
4.2.2.	Preparation of mesoporous Pt nanoparticles.....	75
4.2.3.	Characterization	76

4.3.	<i>Results and Discussion</i>	77
4.4.	<i>Conclusion</i>	91
	<i>References</i>	92
Chapter 5		95
	<i>Microwave-Assisted Rapid Synthesis of Branched Platinum Nanoclusters with High Surface Area</i>	
5.1.	<i>Introduction</i>	96
5.2.	<i>Experimental Process</i>	98
	5.2.1. Materials	98
	5.2.2. Synthesis of platinum nanoclusters	98
	5.2.3. Characterization	98
5.3.	<i>Results and Discussion</i>	99
5.4.	<i>Conclusion</i>	105
	<i>References</i>	106
Chapter 6		109
	<i>Synthesis of Mesoporous Pt Films with Tunable Pore Sizes from Aqueous Surfactant Solutions</i>	
6.1.	<i>Introduction</i>	110
6.2.	<i>Experimental Process</i>	112
	6.2.1. Materials	112
	6.2.2. Electrodeposition	112
	6.2.3. Characterizations	112
6.3.	<i>Results and Discussion</i>	114
6.4.	<i>Conclusion</i>	136

<i>References</i>	137
Chapter 7	140
<i>Synthesis of Mesoporous Pt-Pd Alloy Films by Electrochemical Plating in Aqueous Surfactant Solutions</i>	
7.1. <i>Introduction</i>	141
7.2. <i>Experimental Process</i>	143
7.2.1. <i>Electrodeposition of mesoporous Pt-Pd alloy films</i>	143
7.2.2. <i>Characterization</i>	143
7.3. <i>Result and Discussion</i>	145
7.4. <i>Conclusion</i>	155
<i>References</i>	156
Chapter 8	158
<i>General Conclusions and Future Perspective</i>	
8.1. <i>Overview of My Achievement</i>	159
8.2. <i>Significant Advances in Hard-templating Method</i>	164
8.3. <i>Significant Advances in Soft-templating Method</i>	166
8.4. <i>Future Perspective</i>	169
<i>References</i>	172
<i>List of Publications</i>	174
ACKNOWLEDGEMENTS	180

Chapter 1

General

Introduction

1.1. Introduction

1.1.1. Mesoporous Materials

Porous materials widely exist in the earth. To some extent, most all of the earth's solid contents are porous, except metals and ceramics that are fired at high temperatures. As shown in **Figure 1.1**, according to the pore size, porous materials are generally classified into macroporous materials with a porous size over 50 nm, mesoporous materials with a porous size ranged from 2 nm to 50 nm and microporous materials with a porous size lower than 2nm.



Figure 1.1 Classification of porous materials.

Compared with macroporous materials, which owns low surface area and large non-uniform pores, micro- and mesoporous materials have wide applications for chemical sensors, shape-selective catalysis, chemical separations and electronic applications. With the presence of well-ordered microstructures (e.g., zeolites and molecular sieves), the shape selectivity and sorptive capacity of porous materials are enhanced. Because of the limitations of the microporous materials, approaches and routes to expand the pore size beyond the micropore region are highly desired. Owing to the need for higher accessible surface area and pore volume for efficient chemical processes, there is a growing demand for highly stable porous materials.

In the early 1990s, the first family of silicate mesoporous molecular sieves known as M41S was reported [1-3]. With their unique properties such as ultrahigh surface area, uniform and tunable pore sizes, and narrow pore size distribution, ordered mesoporous materials became a focus of attention in a very short time. Much effort has focused on synthesis and application of ordered mesoporous materials. A large variety

of mesoporous materials with different mesostructures have been synthesized, such as 2D hexagonal, space group $p6mm$, 3D hexagonal $P6_3/mmc$, 3D cubic Pmm , Pmn , Fdm , Fmm , Imm , bicontinuous cubic Iad , etc. The development of ordered mesoporous materials provides a series of materials with large uniform pore sizes between 2 to 50 nm, highly ordered nanochannels, and high surface areas.

In comparison with traditional industrial porous materials (such as zeolite), mesoporous materials break through the size restriction of conventional microporous materials because their uniform and tunable pores sizes can afford enough void spaces for large molecules [4, 5], which makes mesoporous materials have a wider range of applications, such as adsorption [6], the separation of large molecules, catalysis [7-9], drug and DNA delivery [10-13], sensors [14], devices [15, 16], Li-ion batteries and fuel cells [17]. Their high surface area provides adequate reaction sites for interface-related processes.

1.1.2. Mesoporous Metals

Since the discovery of ordered mesoporous silica, various mesoporous materials with different framework compositions have been synthesized, such as carbons, metals, metal oxides and sulfides, inorganic-organic hybrid materials, and polymers. Although there have been some successful studies to synthesis of non-siliceous mesoporous materials, it still remains a grand challenge because the mesostructures of such materials may collapse during the removal of templates [18, 19]. In contrast, mesoporous metals, especially noble metallic mesoporous materials, have currently been attracting considerable interests [20].

In material science and technology, bulk metals have been used for a long time, and they are irreplaceable in a variety of industrial production. The synthesis of ordered mesoporous metals is still a great challenge, because metals have high surface energies that favor low surface areas. The emergence of mesoporous metals has endowed nano-sized metal materials a new stage. Due to their fascinating physicochemical properties, such as electrical and thermal conductivity, nanostructured metals have been used in a various applications such as bio-sensors, surface-enhanced Raman scattering, surface plasmon resonance, hydrogen storage, and catalysis [21-24]. Although a growing amount of research has focused on the synthesis of mesoporous metals in recent years

[25], the development of facile and efficient methods to synthesis of mesoporous metal materials with large surface areas and superior activities is highly desired. Therefore, new strategies and techniques are continuously being developed for the tailored synthesis of mesoporous metal materials.

1.2. General Synthetic Pathways for Mesoporous Materials

The soft-templating approach and hard-templating approach are two general routes to synthesis of mesoporous metals shown as **Figure 1.2**.

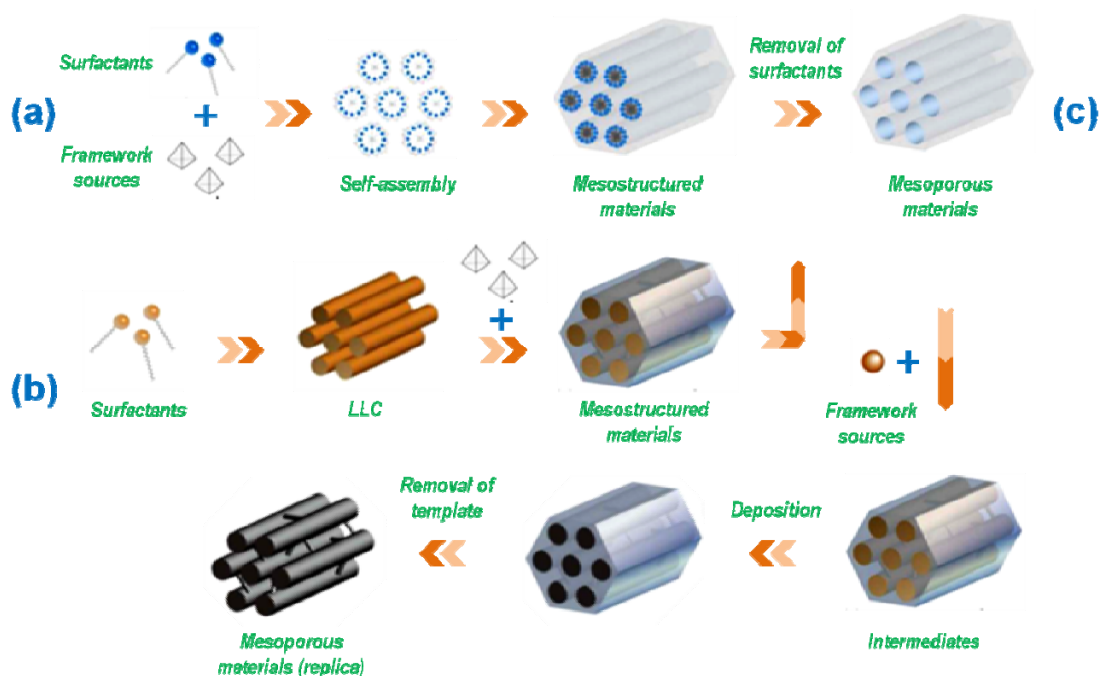


Figure 1.2 Systematic presentations for synthesis of mesoporous materials by different routes. (a) Co-assembly of inorganic precursor and organic surfactant assisted self-assembly for mesoporous materials. (b) “True” liquid-crystal templating process for mesoporous materials. (c) Hard-templating route.

1.2.1. Soft-Templating Method

Investigation on the role of soft-organic materials, serving as a template in the preparation of mesoporous materials, has attracted tremendous interest since the first

reports on the synthesis of mesoporous silicas [1-3]. The products (M41S) in Mobil's report by using quaternary ammonium cationic surfactants such as cetyltrimethylammonium bromide ($C_{16}H_{33}N(CH_3)_3Br$, CTAB) showed highly ordered mesopores with uniform pore size, which is different from the previously investigated nanoporous materials with disordered, widely-distributed pore structure. Since then, a great variety of mesoporous metallic materials with controllable pore sizes and pore structures, tunable morphologies, and varying framework compositions have been synthesized via the soft-templating approach. In general, the soft-templating syntheses are accomplished through the cooperative assembly of inorganic precursors and amphiphilic surfactants based on electrostatic interaction, hydrogen binding, *etc.* To date, various soft templates, including small-molecular surfactants (cationic, nonionic, or anionic) and high-molecular weight amphiphilic block copolymers, have been exploited to synthesize ordered mesoporous metallic materials. Surfactants are amphiphilic organic compounds containing hydrophilic groups as well as hydrophobic groups. According to the nature of hydrophilic moieties, surfactants can be classified as anionic, cationic, and nonionic types. After dissolving in solution, the surfactants self-assemble into aggregates such as micelles, liquid crystals, or microemulsions due to their amphiphilic characteristics. There are two soft-templating routes for the synthesis of mesoporous metallic materials; cooperative self-assembly route (**Figure 1.2a**) and lyotropic liquid-crystal (LLC) route (**Figure 1.2b**), respectively.

A large number of studies have been carried out to investigate the formation and assembly of mesostructures on the basis of surfactant self-assembly. Self-assembly, generally, refers to a spontaneous organization of building blocks driven by noncovalent interactions, such as hydrogen bonding, hydrophobic interactions, π - π stacking, and electrostatic interactions. In **Figure 1.2a**, surfactant monomers self-associate to form aggregates known as micelles when the concentration of surfactants is above the critical micelle concentration (CMC). Further increase of the concentration of surfactants will result in the formation of an ordered mesophase, which is composed of micelles. Micellization is a process of force balance between attractive and repulsive forces. The attractive driving force is usually hydrophobic, which makes the hydrophobic moieties of surfactant molecules come close to each other. The repulsive force is usually electrostatic repulsion and/or a steric hindrance effect, which induces the hydrophilic

moieties to separate from each other. Formation of micelles results from the balance of these two opposite forces. When the concentration of surfactant is higher than CMC, some isolated monomers start to self-assemble into micelles. Depending on the properties of solvents, there are normal micelles and reverse micelles. The primarily formed micelles are usually spherical. However, this spherical structure of micelles can evolve into rod-like, wormlike, or ellipsoidal micelles, since the new force becomes balanced after changing some parameters, such as increasing the surfactant concentration [26] and adding some salts as counter ions [27]. After the condensation, the organic templates can be removed by calcination, extraction, *etc.* This kind of approach provides a general way for the production of mesoporous metals as well as related nanomaterials.

Another soft-templating approach for the synthesis of mesoporous materials is the LLC-template route (**Figure 1.2b**) [28]. Surfactant micelles undergo a self-assembly to form liquid crystal mesophases with the increase of the surfactant concentration (**Figure 1.2b**). Typical liquid crystal mesophases are lamellar with 1D periodicity, hexagonal with 2D periodicity, and cubic with 3D periodicity. Lamellar and hexagonal liquid crystals are composed of bilayers and micellar rods, respectively. There are cubic liquid crystal mesophases, such as $Fm-3m$ with spherical micellar building blocks, and other well-reported cubic liquid crystal mesophases, such as bicontinuous gyroid $Ia-3d$ and clathrate $Pn-3m$ with building blocks derived from primitive spherical micelles. Such LLC can be used as direct template for synthesis of mesoporous materials, as shown in **Figure 1.2b**.

Many kinds of mesoporous metals and related metal alloys have been successfully prepared by various methods. Mesoporous metals can be obtained by reducing metal ions in lyotropic liquid crystals followed by removing the templates (**Figure 1.2b**). The mesostructure of metals can be rationally designed and tailored. A large number of highly ordered mesoporous metal materials with controllable pore sizes and pore structures, tunable morphologies, and varying framework compositions have been synthesized via the surfactant templating approach.

When the surfactant concentration increases to a high concentration (normally more than 40 wt %), the lyotropic liquid-crystal (LLC) phases appear [29]. The mesostructures of the LLCs formed strongly depend on the molecular structure,

concentration, and temperature. Since the pioneering work by Attard *et al.* in 1997 [30, 31], various ordered mesoporous metals have been prepared *via* LLC phases. The mesopore diameters can be easily controlled by the choice of surfactant and the addition of lipophilic substances. Other metal-based nanostructures, such as nanotubes [32], nanorods [33], nanosheets [34], and nanoparticles [35], have been designed by modifying the LLCs-template routes. Yamauchi *et al.* deposited Pt and Pt-based alloys from LLC-template films with 2D hexagonal symmetry *via* vapor infiltration of a reducing agent of DMAB (**Figure 1.3**) [36]. The prepared LLC films with metal ions were placed in a closed container together with DMAB as a reducing agent, and mesoporous metal was deposited through vapor infiltration of the reducing agent. This method can also be combined with the hard-templates (such as porous anodic alumina membrane, PAAM) to synthesize nanorods with a mesoporous structure. Furthermore, in the same system, by applying a reduced pressure process before metal deposition, mesoporous Pt nanotubes could be successfully prepared [37].

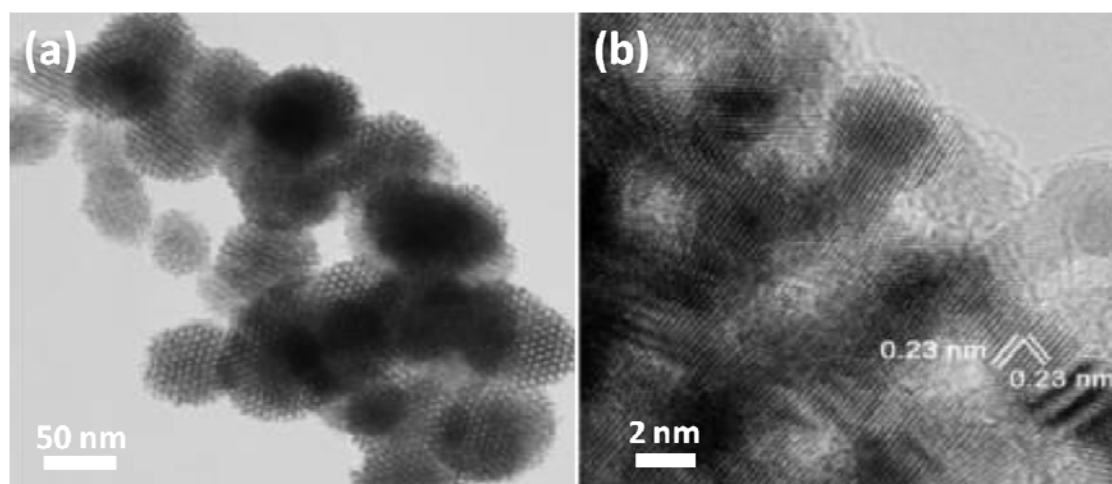


Figure 1.3 (a) TEM images of the typical mesoporous Pt particles prepared by vapor infiltration method. (b) High-magnification TEM image. Remade with permission from Ref 36. Copyright © 2008 American Chemical Society.

The synthetic process is based on either a solution assembly or an evaporation-induced self-assembly (EISA). The solution-assembly approach involves the reaction of building blocks in a surfactant-containing solution in which the surfactant concentration

greatly exceeds the critical micelle concentration. The EISA approach utilizes precursor solutions containing building surfactant concentration is above or below the critical micelle concentration. Solvent evaporation during a coating, spraying, fiber-spinning, or microwriting process increases the surfactant and building-block concentrations and promotes their assembly into ordered mesostructures. Compared to the solution assembly approach, the EISA approach allows a more rapid formation of mesostructured materials in the forms of thin films, particles, fibers, and arrays for device applications. For a convenient operation, a LLC-templating can be directly formed from a diluted surfactant solution by evaporation-mediated direct templating method (EDIT) without heating-aging process.

In addition to chemical reduction, for metal deposition, electrochemical deposition is another important process for synthesizing mesoporous metals. By electrochemical deposition, mesoporous metallic films have been formed on a conductive substrate. Electrodeposition using an external power source is one of the main methods for reducing metal ions. The electrodeposition system involves a three-electrode cell consisting of a working electrode, a reference electrode and a counter electrode, respectively. Mesoporous metal thin films are deposited onto conductive substrates (such as an Au-coating substrate and an ITO substrate) that act as a working electrode. Attard and co-workers reported the synthesis of mesoporous platinum films with a H_1 -ePt structure by electrodeposition from an electroplating mixture, which contained a 42 wt% nonionic surfactant ($C_{16}EO_8$) [31]. The electrodeposition of platinum from the liquid crystalline plating mixture was conducted onto polished gold electrodes. Chung *et al.* [38] fabricated 3D nanoporous Pt film via electrochemical deposition in a reverse micelle (L_2) solution of a nonionic surfactant. Edler *et al.* [39] and Kijima *et al.* [40] applied the LLC-template approach to prepare mesoporous Ag films and nanogroove network-structured Pt nanosheets, respectively.

Various organic templates, including small-molecular surfactants and high-molecular weight amphiphilic block copolymers, have been utilized to synthesize ordered mesoporous metals so far (**Figure 1.4**). The pore size is mainly determined by the hydrophobic volume of the used templates. Therefore, block copolymers with long hydrophobic chains enable ordered mesoporous metallic materials with large pores. The large mesopores can accommodate large-size guest objects in adsorption immobilization

of biomacromolecules and for catalysis without blocking the pore channels. One of the most widely used high-molecular weight templates is commercially available poly (ethylene oxide)-*b*-polystyrene (PEO-*b*-PS) [41]. Alternatively, Wiesner and co-workers recently reported a new route to synthesis of mesoporous metal thin films by assembling platinum and palladium nanoparticles stabilized in the presence of amphiphilic block copolymers [42, 43].

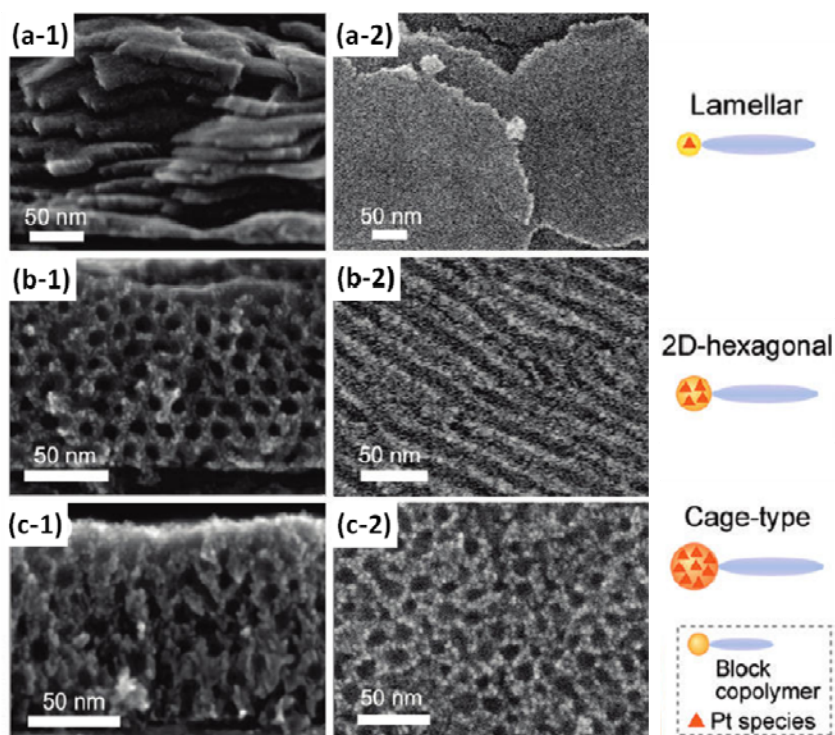


Figure 1.4 SEM images of Pt films with three types of mesostructure (two-dimensional-hexagonal, lamellar, and cage-type) which can be synthesized by controlling compositional ratios between block copolymers and Pt species in the used precursor solutions. Remade with permission from Ref 41. Copyright © 2010 American Chemical Society

Amphiphilic block copolymers consisting of two or more polymeric blocks of different hydrophilicity are widely used as soft-templates [44]. Microphase separation is usually induced by a selective solvent good for one of the blocks, resulting in micelles similar to surfactants. Similarly, block copolymer micelles can further organize into liquid crystal mesophases under certain conditions [45]. The use of block copolymers as

the structure-directing agent is superior to that of surfactants with low molecular weight in terms of pore size expansion and thick inorganic frameworks. The larger pore size offers enough space for large molecules and facilitates guest transportation in the framework.

1.2.2. Hard-Templating Method

Since mesoporous silicates were first discovered, organic- inorganic assembly combined with sol-gel processes using surfactants as structure-directing agents had been considered to be the major pathway for creating mesoscaled periodic materials. Unfortunately, many mesostructured materials can not be prepared by the sol-gel process. Nanocasting (hard-templating route) using highly ordered mesoporous silica as a template has brought forward incredible possibilities in preparing novel mesostructured materials. In a hard-templating route, preformed porous materials, such as silica and silica-replicated carbon, are employed, as the template and the porous spacing are filled with precursors of targeted materials (**Figure 1.2c**) [46]. Different from one-pot soft-templating method, the hard-templating method usually involves three steps, which are preparing the original template, depositing metal elements into the mesopores of templates by sorption, phase transition, ion exchange, complex or covalent grafting. After removal of the templates, the nanomaterials can completely maintain the topologies of the templates to achieve interesting replica mesostructures. This process was firstly applied to the preparation of mesoporous carbon, and then large numbers of related materials with different components, mainly including metals, metal oxides and metal sulfides, were successfully synthesized.

In the hard-templating method, precise control of replica structures is possible by changing the original mesostructures of the used mesoporous templates, such as silica and carbon. Mesoporous silica with a robust framework and high thermal stability is often used as a hard template to synthesize a metal replica. To date, various metal nanostructures, such as 1D nanowires and 3D nanowire networks, have been prepared by using MCM-41 (*p6mm*) [47], SBA-15 (*p6mm*) [48], KIT-6 (*Ia-3d*) [49], and MCM-48 (*Ia-3d*) [50] as hard templates. There are some reports on the formation of small organized silver network domains in MCM-48 [51]. Stucky *et al.* prepared silver nanowires using SBA-15 as the template [52, 53]. Ryoo and co-workers reported

nanoporous Pt with 3D networks by the impregnation of a Pt precursor followed by H₂ reduction within the mesopores of the MCM-48 (*Ia3d*) template [54]. By using SBA-15 as a hard template, UV/Vis irradiation was an efficient method for the reduction of metal precursors to synthesis of nanoparticles and nanowires [55]. Uniformly dispersed metallic nanoparticles were successfully formed by inducing simultaneous nucleation in mesoporous silica matrices (FSM-16).

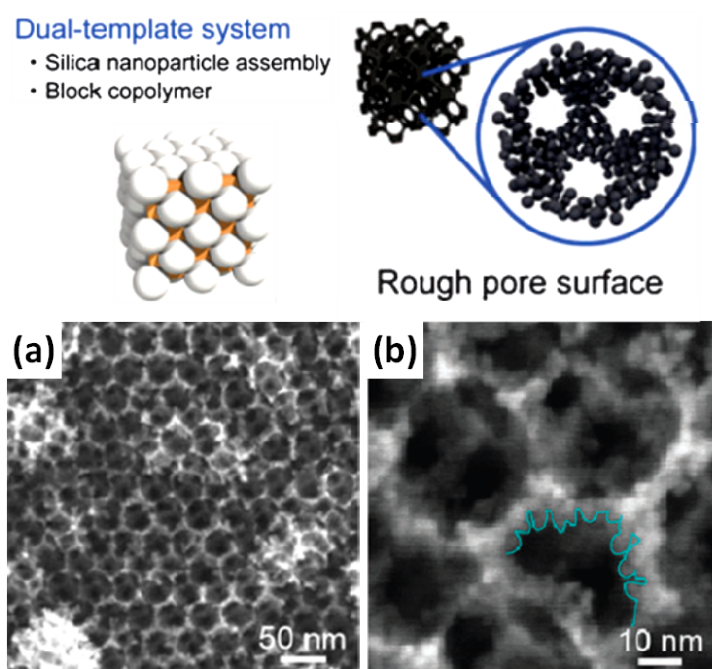


Figure 1.5 Cage-type mesoporous Pt with tunable large mesopores possessing smooth and rough pore surfaces prepared by Pt deposition in the absence and presence of block copolymer in hard-templates, respectively. Remade with permission from Ref 56. Copyright © 2010 Royal Society of Chemistry.

Recently, Kuroda and Yamauchi *et al.* used silica nanoparticles (with 30 nm diameter) as a hard template and prepared cage-type mesoporous Pt (**Figure 1.5**) [56]. Then, they tried to make copolymer surfactant (P123) into the precursor solution to serve as a soft template. After removing the surfactant and silica, mesoporous Pt with a rough surface wall was obtained. Due to its huge surface area, this mesoporous Pt material could be considered as a promising catalyst with high catalytic activity. Ye *et al.* synthesized highly ordered mesoporous Pd by using face-centered cubic silica super

crystal (with a pore diameter of 40 nm) as a template (**Figure 1.6**) [57]. This method can precisely control the mesopore sizes of the products by changing the diameters of the used silica nanoparticles.

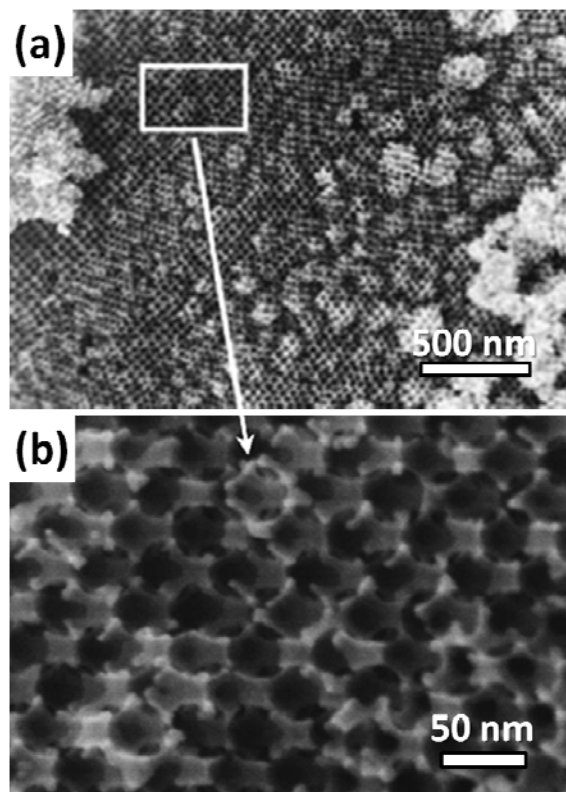


Figure 1.6 High-resolution SEM images of (a) Pd infiltrated silica super crystal and (b and c) silica-free Pd networks. Remade with permission from Ref 57. Copyright © 2010 Royal Society of Chemistry.

1.2.3. Other Methods

Dealloying or selective removal of one or more components from an alloy has become a routine technique for the rapid and direct generation of nanoporous metals. The obtained nanopores are randomly arranged, which is contrast to mesoporous metals by using soft-templates. Historically, dealloying was used for depletion gilding in ancient societies [58, 59]. In 1927, Raney invented the well-known Raney nickel, which is used as a heterogeneous catalyst for hydrogenation reaction [60]. In this century, the selective dissolution of less noble metal from bimetallic alloy systems has been mostly

studied in the corrosion realm to produce nanoporous materials for catalytic and sensory applications [61, 62]. The dealloying process gives rise to a unique bicontinuous nanostructure consisting of mesosized metallic ligaments, which enables nanoporous metals and alloys to have good electrical conductivity and large effective surfaces as ideal electrodes for electrocatalysis. When placed in a controlled corrosive environment, the electrochemically active metal of an alloy can be leached, resulting in a continuous sponge-like structure. This method is widely used in industry, usually for preparing mesoporous noble metals, such as Au, Pt, Pd, and their based alloys. In earlier reports, the obtained nanoporous metals always have uncontrollable pore size and a wide pore size distribution. However, with the improvement of the synthesis condition, various nanoporous metals are currently prepared.

In recent years, focused electron-beam induced deposition (FEBID) has shown impressive advance as a micro- and nanofabrication tool. Its application ranges from photomask repair [63], single-crystal nanowires [64], and nanopores [65] to magnetic sensors [66-68] or tunable strain sensors [69]. For the FEBID process, typically, a single precursor gas is used in order to create a solid deposit by dissociation of the precursor molecules that are adsorbed on the substrate. M. Huth and co-workers extended the standard FEBID approach to binary systems and successfully synthesized Pt-Si nanostructure materials. They extends the base of accessible materials to a large degree and in addition offers a pathway for the formation of materials far away from thermal equilibrium conditions, therefore enabling the formation of metastable phases that are not accessible by standard deposition techniques.

1.3. Potential Applications of Mesoporous Metals

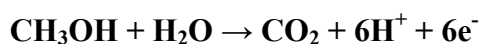
Metals, especially noble metals (e.g. Pt, Ru, Pd, Au), are used in industrial production for several decades. Mesoporous structures with large surface areas are technologically important. In particular, noble metals with high surface area are routinely employed as catalysts in fuel cells, as substrates for surface-enhanced Raman spectroscopy, and for sensor application.

1.3.1. Direct Methanol Fuel Cells (DMFCs)

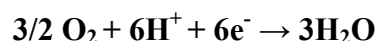
Recent years, direct methanol fuel cells (DMFCs) have attracted considerable attention as a promising power sources for portable electronics due to their ease of handling, high-energy densities, and low operation temperatures. Compared to hydrogen, methanol has several advantages, such as modest cost, ease of handling and storing. In addition, the toxicity is relatively low among organic fuels [70, 71].

The electrode reactions are as follows:

Anode – Methanol oxidation reaction (MOR)



Cathode – Oxygen reduction reaction (ORR)



Overall: $\text{CH}_3\text{OH} + 3/2 \text{O}_2 \rightarrow \text{CO}_2 + 2\text{H}_2\text{O}$

Pt and Pt-based nanomaterials are the most effective catalytic materials toward both the oxygen reduction reaction (ORR) and methanol oxidation reaction (MOR) [72-74]. The use of platinum for fuel cell catalysts is a result of the relatively fast kinetic rates for oxidation and reduction of the fuel and oxidant, used in these low-temperature fuel cells. It is also well known that the catalytic activity of platinum is strongly dependent on the particle shape and size. One of the main issues relating to the catalyst is to reduce the weight of the expensive catalyst. Thus, mesostructured shape with high surface areas is highly desirable. Meso/nanoporous Pt has been successfully employed commercially as a catalyst for such applications. A number of previous works showed that the electrocatalytic activities of Pt could be improved by tailoring the shape of Pt nanostructures. For example, Pt nanowires and nanocubes exhibited higher ORR performances than spherical Pt nanoparticles [75]. Accordingly, nanoporous Pt is frequently used in chemical engineering for organic reactions, such as hydrogenations, refining petroleum, and automotive exhaust. Mesoporous Pt electrodes are applied in the electrochemical detection of glucose [76], pH [76], dissolved oxygen [78] and hydrogen peroxide [79].

In fuel cells porous Pt serves as catalyst for the electro-oxidation of fuels such as hydrogen, methanol, ethanol, formic acid or glucose as well as the electroreduction of oxygen [80-82]. This is because Pt shows the highest catalytic activities of all pure metals for the corresponding reactions [83]. The high surface area of porous Pt enables a high fuel turnover rate at low electrode polarization and hence a high power output of the fuel cell. A big drawback of Pt is its price. The price of one ounce has increased from \$583 in 2000 to \$1581 in 2010 [84]. Therefore a main goal in fuel cell research is to reduce the mass of Pt per surface area during fabrication. One strategy to minimize the amount of Pt is to control its size and shape [85].

Control of Pt particle size is important. For instance, decreasing Pt particle size enables an increase in surface, thus increasing the numbers of catalytically active sites per mass, which means higher Pt utilization [86]. Another strategy is to replace a fraction of Pt by a cheaper element such as ruthenium [87]. In many fuel cell systems the application of alloy catalysts is also desired. For instance, in methanol fuel cells alloy catalysts show a better resistance towards CO poisoning at the anode and an improved tolerance towards methanol crossover effects at the cathode compared to pure Pt.

Special attention has been focused on bimetallic alloys for meso/nanoporous materials because such structures have unusual catalytic, electronic, optical, and magnetic properties [88]. Meso/nanoporous metal thin films have great potential in various applications, such as catalysis, electrical contacts, plasmonics, energy storage, and conversion.

1.3.2. Clean Energy Production and Storage

Future energy supply is dependent on hydrogen as a clean energy carrier. Hydrogen can be produced from fossil fuels, water electrolysis and biomass. However, the current debates on the hydrogen economy are intimately linked to the clean production of hydrogen from fossil fuels such as natural gas and coal. Hydrogen storage will be essential in hydrogen economy infrastructure. Currently there are no optimal systems for hydrogen storage. Hydrogen can be stored in gaseous, liquid or more recently in solid forms. Mesostructured materials, such as mesoporous Pd, are promise adsorbent.

1.3.3. Optical Applications

As another application, the optical properties of nanoporous gold are significantly different from those of bulk gold. Since the pore size is usually much smaller than the wavelength of visible light, which is between 400 nm and 700 nm, significant surface plasmon resonance (SPR) can be achieved [89]. A significantly higher density of atomic step edges on nanoporous gold compared with bulk gold makes nanoporous gold to be good catalysts for O₂ reduction in gas phase catalysis of methanol oxidation [90]. Nanoporous gold is an effective biological platform with respect to its low electrode-electrolyte impedance, which provides a superior signal-to-noise ratio for detection of neural activity [91].

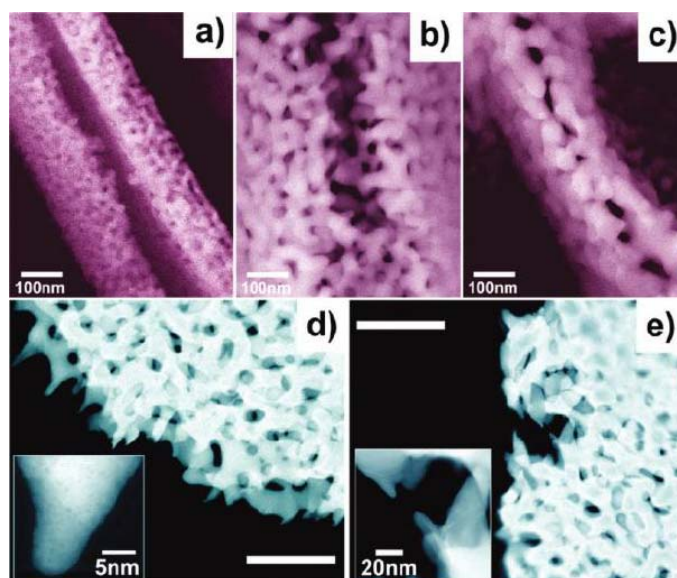


Figure 1.7 SEM and STEM micrographs of wrinkled nanoporous gold. (a-c) The ridges of the wrinkled nanoporous gold with the nanopore sizes of ~12 (a), 26 (b) and 38 (c). (d,e) STEM images of the fractured ridges of the wrinkled nanoporous gold with nanopore size of 26 nm. The insets of d and e show individual sharp nanotips. The scale bars shown in panels d and e are 200 nm. Remade with permission from Ref 95. Copyright © 2011 American Chemical Society.

Surface-enhanced Raman spectroscopy (SERS) combines the capability of molecular fingerprinting with ultrahigh sensitivity, allowing single-molecule detection [92]. Nanoporous gold is also a suitable material for tunable SERS [93]. Surface enhanced Raman scattering (SERS) has been widely used for uniquely identifying

molecules with very high detection sensitivities and, thus, is an excellent platform for chemical and biological sensing. SERS provides a drastic enhancement in scattering efficiency over traditional Raman scattering, primarily due to the presence of intense electromagnetic fields localized at the metal surface where molecules are adsorbed. Nanoporous gold films have been demonstrated to enable highly sensitivity detection [94]. Recently, Chen *et al.*[95] synthesized a kind of wrinkled nanoporous gold, which was prepared by selective dissolution of silver from Au-Ag alloy leaves using nitric acid at room temperature (**Figure 1.7**). The prepared nanoporous gold films have a vertical 3D mesostructure with plentiful nanogaps and sharp nanotips that act as electromagnetic “hot-spots” when interacting with incident light. The SERS enhancement of the wrinkled nanoporous gold is more than 100 times higher than that of the prepared mesoporous gold, which yields a local enhancement factor of $\sim 10^9$.

Nanostructured silvers have been widely investigated as antimicrobial materials, bio-sensors, catalysts, and advanced materials exhibiting surface Plasmon resonance and surface enhanced Raman scattering [96].

1.3.4. Biomedical Applications

Technologic evolution has led the field of catalysis to focus on smaller and smaller dimensions. State of the art performing catalyst materials are commonly tailored in crystalline structure, composition, porosity, size and precise placement within an application. Directed control and manipulation of catalyst morphology is important because high surface area or high activity phase dispersions, as well as facilitation of rapid mass transfer of reactants and products, are key to the performance of an active catalyst. Several techniques have been used to increase catalyst performance through use of high surface area supporting structures, increasing the internal surface area of the catalyst themselves, and optimizing catalyst morphology to enhance reaction activity. With large specific surface area, relatively large pore size and the regularity of the pore structure, ordered mesoporous metallic materials can be excellent shape-selective catalysts for macromolecules, such as DNA and protein.

Research on mesoporous materials for biomedical purposes has experienced a notably increase during recent years. Since 2001, when MCM-41 was first proposed as drug-delivery system, silica based materials, such as SBA-15 or MCM-48, and some

metal-organic frameworks have been discussed as drug carriers and controlled-release system. Mesoporous materials are intended for both systemic delivery systems and implantable local-delivery devices. The latter application provides very promising possibilities in the field of bone tissue repair because of the excellent behavior of these materials as bioceramics.

Controlled drug-delivery system (DDSs) is one of the most promising applications for human health care and represents an ever-evolving field for biomedical materials science [97]. A drug delivery system can be described as a formulation that controls the rate and period of drug delivery (i.e. time-release dosage) and targets specific areas of the body [98].

The field of nanotechnology in recent years has motivated researchers to develop nanostructured materials for biomedical application. The high pore volume and high surface area make mesoporous materials excellent candidates for controlled drug delivery systems.

References

- [1] C. T. Kresge, M. E. Leonowicz, W. J. Roth, J. C. Vartuli, and J. S. Beck, *Nature*, **359**, 710 (1992).
- [2] J. S. Beck, J. C. Vartuli, W. J. Roth, M. E. Leonowicz, C. T. Kresge, K. D. Schmitt, C. T. W. Chu, D. H. Olson, E. W. Sheppard, S. B. McCullen, J. B. Higgins, and J. L. Schlenker, *J. Am. Chem. Soc.*, **114**, 10834 (1992).
- [3] T. Yanagisawa, T. Shimizu, K. Kuroda, and C. Kato, *Bull. Chem. Soc. Jpn.*, **63**, 988 (1990).
- [4] M. E. Davis, *Nature*, **417**, 813 (2002).
- [5] M. Hartmann, *Chem. Mater.*, **17**, 4577 (2007).
- [6] Y. H. Deng, D. W. Qi, C. H. Deng, X. M. Zhang, and D. Y. Zhao, *J. Am. Chem. Soc.*, **130**, 28 (2008).
- [7] Y. H. Deng, Y. Cai, Z. K. Sun, J. Liu, C. Liu, J. Wei, W. Li, C. Liu, Y. Wang, and D. Y. Zhao, *J. Am. Chem. Soc.*, **132**, 8466 (2010).
- [8] G. C. Ma, X. Q. Yan, Y. L. Li, L. P. Xiao, Z. J. Huang, Y. P. Lu, and J. Fan, *J. Am. Chem. Soc.*, **132**, 9596 (2010).
- [9] M. Vallet-Regi, A. Ramila, R. P del Real, and J. Perez-Pariente, *Chem. Mater.*, **13**, 308 (2001).
- [10] J. L. Vivero-Escoto, I. I. Slowing, C. W. Wu, and V. S. Y. Lin, *J. Am. Chem. Soc.*, **131**, 3462 (2009).
- [11] R. Liu, Y. Zhang, X. Zhao, a. Agarwal, L. J. Mueller, and P. Y. Feng, *J. Am. Chem. Soc.*, **132**, 1500 (2010).
- [12] D. R. Radu, C. Y. Lai, K. Jeftinija, E. W. Rowe, S. Jeftinija, and V. S. Y. Lin, *J. Am. Chem. Soc.*, **126**, 13216 (2004).
- [13] C. Y. Lai, B. G. Trewyn, D. M. Jeftinija, K. Jeftinija, S. Xu, S. Jeftinija, and V. S. Y. Lin, *J. Am. Chem. Soc.*, **125**, 4451 (2003).
- [14] F. Jiao, and P. G. Bruce, *Adv. Mater.*, **19**, 657 (2007).
- [15] Y. F. Shi, B. K. Guo, S. A. Corr, Q. H. Shi, Y. S. Hu, K. R. Heier, L. W. Chen, R. Seshadri, and G. D. Stucky, *Nano Lett.*, **9**, 4215 (2009).

- [16] E. Rossinyol, A. Prim, E. Pellicer, J. Arbiol, F. Hernandezramirez, F. Peiro, A. Cornet, J. R. Morante, L. A. Solovyov, B. Tian, T. Bo, and D. Zhao, *Adv. Funct. Mater.*, **17**, 1801 (2007).
- [17] F. Pereira, K. Valle, P. Belleville, A. Morin, S. Lambert, and C. Sanchez, *Chem. Mater.*, **20**, 1710 (2008).
- [18] C. Marquez-Alvarez, N. Zilkova, J. Perez-Pariente, and J. Cejka, *Catal. Rev. Sci. Eng.*, **50**, 222 (2008).
- [19] J. N. Kondo, and K. Domen, *Chem. Mater.*, **20**, 835 (2008).
- [20] Y. Yamauchi, and K. Kuroda, *Chem.-Asian J.*, **3**, 664 (2008).
- [21] N. C. Bigall, A. K. Herrmann, M. Vogel, M. Rose, P. Simon, W. Carrillo-Cabrera, D. Dorfs, S. Kaskel, N. Gaponik, and A. Eychmuller, *Angew. Chem. Int. Ed.*, **48**, 9731 (2009).
- [22] A. Tao, F. Kim, C. Hess, J. Goldberger, R. R. He, Y. G. Sun, Y. N. Xia, and P. D. Yang, *Nano Lett.*, **3**, 1229 (2003).
- [23] C. Lofton, and W. Sigmund, *Adv. Funct. Mater.*, **15**, 1197 (2005).
- [24] X. Sun, and Y. Li, *Adv. Mater.*, **17**, 2626 (2005).
- [25] V. Chiola, J. E. Ritsko, and C. D. Vanderpool, US patent No. 3556725 (1971).
- [26] D. J. Mitchell, G. J. T. Tiddy, L. Waring, T. Bostock, and M. P. McDonald, *J. Chem. Soc. Faraday Trans.*, **79**, 975 (1983).
- [27] E. Leontidis, *Curr. Opin. Colloid Interface Sci.*, **7**, 81 (2002).
- [28] G. S. Attard, J. C. Glyde, and C. G. Göltner, *Nature*, **378**, 366 (1995).
- [29] N. R. B. Coleman, and G. S. Attard, *Microporous Mesoporous Mater.*, **44**, 73 (2001).
- [30] G. S. Attard, J. M. Corker, C. G. Goltner, D. C. S. Henke, and R. H. Templer, *Angew. Chem., Int. Ed.*, **36**, 1315 (1997).
- [31] G. S. Attard, *Science*, **278**, 838 (1997).
- [32] T. Kijima, T. Yoshinura, M. Uota, T. Ikeda, D. Fujikawa, S. Mouri, and S. Uoyama, *Angew. Chem., Int. Ed.*, **116**, 230 (2004).
- [33] Q. Zhou, X. Y. Liu, Y. M. Zhao, N. Q. Jia, L. Liu, M. M. Yan, and Z. Y. Jiang, *Chem. Commun.*, 4941 (2005).
- [34] L. Y. Wang, X. Chen, Y. C. Chai, and J. C. Hao, *Colloids Surf. A*, **293**, 95 (2007).

- [35] H. Kawasaki, M. Uota, T. Yoshimura, D. Fujikawa, G. Sakai, and T. Kijima, *J. Colloid Interface Sci.*, **300**, 149 (2006).
- [36] Y. Yamauchi, A. Takai, M. Komatsu, M. Sawada, T. Ohsuna, and K. Kuroda, *Chem. Mater.*, **20**, 1004 (2008).
- [37] A. Takai, Y. Yamauchi, and K. Kuroda, *Chem. Comm.*, 4171 (2008).
- [38] S. Park, S. Y. Lee, H. Boo, H. M. Kim, K. B. Kim, H. C. Kim, *Chem. Mater.*, **19**, 3373 (2007).
- [39] K. Luo, C. T. Walker, and K. J. Edler, *Adv. Mater.*, **19**, 1506 (2007).
- [40] Sakai, G. Yoshimura, T. Isohata, S. et al. *Adv. Mater.*, **19**, 237 (2007).
- [41] A. Takai, Y. Yamauchi, and K. Kuroda, *J. Am. Chem. Soc.*, **132**, 208 (2010).
- [42] S. C. Warren, L. C. Messina, L. S. Slaughter, M. Kamperman, Q. Zhou, S. M. Gruner, F. J. DiSalvo, and U. Wiesner, *Science*, **320**, 1748 (2008).
- [43] H. Arora, Z. Li, H. Sai, M. Kamperman, S. C. Warren, and U. Wiesner, *Macromol. Rapid Commun.*, **31**, 1960 (2010).
- [44] D. Zhao, Q. Huo, J. Feng, B. F. Chmelka, and G. D. Stucky, *J. Am. Chem. Soc.*, **120**, 6024 (1998).
- [45] S. Forster, and M. Antonietti, *Adv. Mater.*, **10**, 195 (1998).
- [46] M. Tiemann, *Chem. Mater.*, **20**, 961 (2008).
- [47] Z. Liu, Y. Sakamoto, T. Ohsuna, K. Hiraga, O. Terasaki, C. H. Ko, H. J. Shin, and R. Ryoo, *Angew. Chem., Int. Ed.*, **39**, 3107 (2000).
- [48] A. Takai, Y. Doi, Y. Yamauchi, and K. Kuroda, *J. Phys. Chem. C*, **114**, 7586 (2010).
- [49] Y. Doi, A. Takai, Y. Sakamoto, O. Terasaki, Y. Yamauchi, and K. Kuroda, *Chem. Comm.*, **46**, 6365 (2010).
- [50] X. J. Guo, C. M. Yang, P. H. Liu, M. H. Cheng, and K. J. Chao, *Crystal Growth & Design*, **5**, 33 (2005).
- [51] L. Z. Wang, J. L. Shi, W. H. Zhang, M. L. Ruan, J. Yu, and D. S. Yan, *Chem. Mater.*, **11**, 3015 (1999).
- [52] M. H. Huang, A. Choudrey, and P. Yang, *Chem. Commun.*, 1063 (2000).
- [53] Y. Han, J. M. Kim, and G. D. Stucky, *Chem. Mater.*, **12**, 2068 (2000).
- [54] H. J. Shin, R. Ryoo, Z. Liu, and O. Terasaki, *J. Am. Chem. Soc.*, **123**, 1246 (2001).

- [55] A. Fukuoka, J. I. Kimura, T. Oshio, Y. Sakamoto, and M. Ichikawa, *J. Am. Chem. Soc.*, **129**, 10120 (2007).
- [56] Y. Kuroda, Y. Yamauchi, and K. Kuroda, *Chem. Comm.*, **46**, 1827 (2010).
- [57] L. Ye, Y. Wang, X. Chen, B. Yue, S. C. Tsang, and H. He, *Chem. Comm.*, **47**, 7389 (2011).
- [58] L. B. Hunt, *Gold Bull.*, **9**, 134 (1976).
- [59] H. Lechtman, *Sci. Am.*, **250**, 56 (1984).
- [60] M. Raney, U. S. Pat. No. 1628190 (1927).
- [61] A. Pareek, S. Borodin, A. Bashir, G. N. Ankah, P. Keil, G. A. Eckstein, M. Rohwerder, M. Stratmann, Y. Grunder, and F. U. Renner, *J. Am. Chem. Soc.*, **133**, 18264 (2011).
- [62] M. Oezaslan, M. Heggen, and P. Strasser, *J. Am. Chem. Soc.*, **134**, 514 (2012).
- [63] T. Liang, E. Frendberg, B. Lieberman, and A. Stivers, *J. Vac. Sci. Technol.*, **23**, 3101 (2005).
- [64] K. L. Klein, S. J. Randolph, J. D. Fowlkes, L. F. Allard, H. M. Meyer, M. L. Simpson, and P. D. Rack, *Nanotechnology*, **19**, 345705 (2008).
- [65] C. Danelon, C. Santschi, J. Brugger, and H. Vogel, *Langmuir*, **22**, 10711 (2006).
- [66] M. Gabureac, L. Bernau, I. Utke, and G. Boero, *Nanotechnology*, **21**, 115503 (2010).
- [67] A. Fernandez-Pacheco, J. M. De Teresa, R. Cordoba, M. R. Ibarra, D. Petit, D. E. Read, L. O'Brien, E. R. Lewis, H. T. Zeng, and R. P. Cowburn, *Appl. Phys. Lett.*, **94**, 192509 (2009).
- [68] L. Serrano-Ramon, R. Cordoba, L. A. Rodriguez, C. Magen, E. Snoeck, C. Gatel, I. Serrano, M. R. Ibarra, and J. M. De Teresa, *ACS Nano*, **5**, 7781 (2011).
- [69] C. H. Schwalb, C. Grimm, M. Baranowski, R. Sachser, F. Porrati, H. Reith, P. Das, J. Muller, F. Volklein, A. Kaya, and M. Huth, *Sensors*, **10**, 9847 (2010).
- [70] A. Kundu, J. H. Jang, J. H. Gil, C. R. Jung, H. R. Lee, S. H. Kim, B. Ku, and Y. S. Oh, *J. Power Sources*, **170**, 67 (2007).
- [71] U. B. Demirci, *J. Power Sources*, **169**, 239 (2007).
- [72] C. Koenigsmann, and S. S. Wong, *Energy Environ. Sci.*, **4**, 1161 (2011).
- [73] E. Antolini, and J. Perez, *J. Mater. Sci.*, **46**, 1 (2011).
- [74] A. Morozan, B. Joussetme, and S. Palacin, *Energy Environ. Sci.*, **4**, 1238 (2011).

- [75] C. Koenigsmann, W. P. Zhou, R. R. Adzic, E. Sutter, and S. S. Wong, *Nano Lett.*, **10**, 2806 (2010).
- [76] J. J. Li, R. Yuan, Y. Q. Chai, X. Che, W. J. Li, and X. Zhong, *Microchim. Acta.*, **172**, 163 (2011).
- [77] J. Noh, S. Park, H. Boo, H. C. Kim, and T. D. Chung, *Lab Chip*, **11**, 664 (2011).
- [78] Y. J. Lee, and J. Y. Park, *J. Kor. Phys. Soc.*, **58**, 1505 (2011).
- [79] Y. J. Lee, J. Y. Park, Y. Kim, and J. W. Ko, *Curr. Appl. Phys.*, **11**, 211 (2011).
- [80] X. Y. Zhang, W. Lu, J. Y. Da, H. T. Wang, D. Y. Zhao, and P. A. Webley, *Chem. Commun.*, 195 (2009).
- [81] H. F. Wang, and Z. P. Liu, *J. Am. Chem. Soc.*, **130**, 10996 (2008).
- [82] H. Wang, H. Y. Jeong, M. Imura, L. Wang, L. Radhakrishnan, N. Fujita, T. Castle, O. Terasaki, and Y. Yamauchi, *J. Am. Chem. Soc.*, **133**, 14562 (2011).
- [83] A. Kloke, F. Stetten, R. Zengerle, and S. Kerzenmacher, *Adv. Mater.*, **23**, 4976 (2011).
- [84] <http://www.platinum.matthey.com/pgm-prices/price-charts/>, in 2010.
- [85] J. Y. Chen, B. Lim, E. P. Lee, and Y. N. Xia, *Nano Today*, **4**, 81 (2009).
- [86] Y. Xia, Y. J. Xiong, B. Lim, and S. E. Skrabalak, *Angew. Chem. Int. Ed.*, **48**, 60 (2009).
- [87] J. H. Choi, K. J. Jeong, Y. Dong, J. Han, T. H. Lim, J. S. Lee, and Y. E. Sung, *J. Power Sources*, **163**, 71 (2006).
- [88] F. Matsumoto, C. Roychowdhury, F. J. DiSalvo and H. D. Abruna, *J. Electrochem. Soc.*, **155**, B148 (2008).
- [89] Y. Ding, and M. Chen, *MRS Bulletin*, **34**, 569 (2009).
- [90] A. Wittstock, V. Zielasek, J. Biener, C. M. Friend, and M. Baumer, *Science*, **327**, 319 (2010).
- [91] E. Seker, Y. Berdichevsky, M. R. Begley, M. L. Reed, K. J. Staley, and M. L. Yarmush, *Nanotechnology*, **21**, 125504 (2010).
- [92] E. C. Le Ru, M. Meyer, and P. Etchegoin, *J. Phys. Chem. B.*, **110**, 1944 (2006).
- [93] M. C. Dixon, T. A. Daniel, M. Hieda, D. M. Smilgies, M. H. V. Chan, and D. L. Allara, *Langmuir*, **23**, 2414 (2007).
- [94] Y. Jiao, J. D. Ryckman, P. N. Ciesielski, C. A. Escobar, G. K. Jennings, and S. M. Weiss, *Nanotechnology*, **22**, 295302 (2011).

- [95] L. Zhang, X. Lang, A. Hirata, and M. Chen, *ACS Nano*, **5**, 4407 (2011).
- [96] A. Tao, F. Kim, C. Hess, J. Goldberger, R. He, Y. Sun, Y. Xia, and P. Yang, *Nano Lett.*, **3**, 1229 (2003).
- [97] M. Malmsten, *Soft Mater.*, **2**, 760 (2006).
- [98] M. Vallet-Regí, F. Balas, D Arcos, *Angew. Chem. Int. Ed.*, **46**, 7548 (2006).

Chapter 2

Synthesis of Mesoporous Co_3O_4 for Low Temperature CO Oxidation

2.1. Introduction

Ordered mesoporous materials are promising and successful candidates in many fields of applications such as catalyst, adsorbent, biocompatible material, and storage [1-4]. Mesoporous materials can be fabricated by either a soft-templating or a hard-templating (i.e., nanocasting) pathway. When compared with soft-templating, it is easy for the hard-templating pathway to prepare ordered mesoporous structures with various compositional and well-developed crystalline frameworks [5]. Mesoporous silica materials, such as KIT-6 with *Ia-3d* symmetry and SBA-15 with *p6mm* symmetry, are most often utilized as hard-templates [6-11]. In particular, KIT-6 mesoporous silica represents as a bicontinuous mesoporous network. Such a 3-dimensional (3D) mesostructure is highly branched and is highly accessible, making it an excellent template to synthesize various mesoporous materials with a wide range of framework compositions (e.g., NiO, Cr₂O₃, Co₃O₄, MgO) [12-14].

The mesoporous materials have high surface area and hence can be used as efficient catalysts. So far, excellent progress has been shown by these mesoporous materials especially in the field of catalysis. One of the most extensively studied reactions is low-temperature oxidation of CO, which is very important for many applications such as air purification, pollution control devices, automotive emission control, and gas purification of the hydrogen to feed fuel cells, closed-cycle CO₂ lasers. The CO and many related hydrocarbons are emitted into the atmosphere during cold start of automobile engines. Though heat-up catalysts are used to control the emission, the emissions are released before the catalyst reaches light-off temperature which causes series environmental issues such as global warming and other extreme weather changes. Therefore, it is quite necessary for the need of new low-temperature oxidation catalysts which further reduces the length of cold start and the amount of emission of CO and hydrocarbons.

Precious metal catalysts with various morphologies have been generally utilized for the CO oxidation reaction, showing high catalytic activity [15-17]. Although the most often studied materials for the low-temperature CO oxidation are Au-based catalysts, the cost of these catalysts is high, which urges the necessity for the search of

an alternative catalyst. Among the various materials, it was well known that Co_3O_4 material showed very high catalytic activity for CO oxidation even at low temperature. However, their catalytic activities are strongly dependent on the preparation methods and deactivated by small amount of water vapor in feed stream [18-22]. For example, Jia *et al.* reported the preparation of Co_3O_4 by using dodecylbenzene sulfonic acid sodium salt (DBS) as the structure directing agent and found that Co_3O_4 can be able to oxidize CO completely at low temperature [20]. However, their method faced a major setback due to the limitation that the absence of DBS resulted in poor catalytic activity. Cunningham *et al.* showed that Co_3O_4 is intrinsically active and reported light-off temperature (temperature at 50% conversion, T_{50}) as $-54\text{ }^\circ\text{C}$, but only under dried conditions [21]. In a normal operation condition, T_{50} was around $40\text{ }^\circ\text{C}$. This is because, in a normal feed gas condition, most of the active sites of Co_3O_4 are covered by the trace amount of moisture present in the normal feed gas and hence the adsorption of CO and oxygen are obstructed.

Several researchers have focused on synthesis of mesoporous Co_3O_4 catalysts with high surface areas and investigation of their CO conversion reactions [23-31]. Among these, Schüth *et al.* have demonstrated the application of mesoporous Co_3O_4 as a highly active catalyst for low temperature CO oxidation for the first time [31]. It was shown that the activity strongly depended on surface area and pore systems of the catalysts. They found the low aging temperature ($40\text{ }^\circ\text{C}$) of KIT-6 gave the highest catalytic activity of mesoporous Co_3O_4 particle which gave T_{50} of CO conversion at $4\text{ }^\circ\text{C}$. Very recently, Ren *et al.* reported that pretreated mesoporous Co_3O_4 particle before catalytic measurement at high temperature, $400\text{ }^\circ\text{C}$, gave 100% CO conversion at $-20\text{ }^\circ\text{C}$ (T_{50} was $-62\text{ }^\circ\text{C}$) [14]. These previous reports showed some optimized synthesis or catalytic measurement conditions to obtain high active mesoporous Co_3O_4 . I consider that the high temperature of pretreatment decreases OH site on surface leads to improvement of water-resistant property of mesoporous Co_3O_4 particle. Accordingly, raising calcination temperature may give a higher catalytic activity. It is well known that calcination temperature controls surface area and pore system of the catalysts to easily alter the number of active sites and sometimes the property of active site [32]. In a hard-templating system on mesoporous materials, raised calcination temperature may bring

about some unique variation and give some new insights in the effect of calcination on catalytic activity.

In this chapter, I carefully investigated the effect of the calcination temperatures (during conversion from Co salts to Co_3O_4 crystals inside mesopores) on the CO oxidation. A series of mesoporous Co_3O_4 particles were prepared by applying different calcination temperatures (450, 500, 600, 700, and 800 °C) using the same hard template of mesoporous silica KIT-6. The variation of surface area, pore size, and catalytic activity in CO oxidation of the mesoporous Co_3O_4 particles was investigated. Since kinetic measurement in CO oxidation by using Co_3O_4 catalyst was improved to be a precise method to express active site and its change [33, 34], kinetic behavior was also compared in terms of apparent activation energy (E_a) and pre-exponential factor (A) per unit area to evaluate catalytic activity together with light-off curves.

2.2. Experimental Process

2.2.1. Preparation of Mesoporous Silica KIT-6

Mesoporous silica (KIT-6) particles were synthesized according to the literature [35, 36]. In a typical synthesis, 4.0 g of poly(ethylene glycol)-block-poly(propylene glycol)-block-poly(ethylene glycol) triblock copolymer (Pluronic P123, PEO₂₀-PPO₇₀-PEO₂₀) was dissolved in 144 g of distilled water and 7.9 g of conc. HCl (35 %) and stirred for 3 h. Then, 4.0 g of n-butanol (Aldrich, 99.4 %) was added under stirring and after one hour, 8.6 g of TEOS (ACROS, 98 %) was added to the reaction mixture. The compositional mole ratios of the reaction mixture were as follows: TEOS: P123: HCl: H₂O: BuOH = 1.00: 0.0170: 1.83: 195: 1.31. The mixture was left under stirring for 24 h at 35 °C, and subsequently hydrothermally heated for 24 h at 100 °C under static conditions in a closed polypropylene bottle. The solid product obtained after hydrothermal treatment was filtered without washing and dried at 80 °C. The surfactant was removed by extraction with solvents followed by calcination at 550 °C. The final product was used as the template for preparation of mesoporous Co₃O₄.

2.2.2. Preparation of Mesoporous Co₃O₄

4.0 g of KIT-6 was soaked in 10.0 ml of 1.6 M Co(NO₃)₂ aqueous solution and subsequently heated for 12 h at 60 °C in a closed vessel. It was known that the melting point of Co(NO₃)₂·6H₂O is 55 °C. Therefore, the nitrate precursor is in the liquid phase at 60 °C and easily moves inside the mesopores of the KIT-6 template. The composite was heated at 200 °C for 6 h and dried. Then, the composite was re-impregnated by 10.0 ml of 1.6 M Co(NO₃)₂ aqueous solution. Then, the composites were calcined under different temperatures (450 °C, 500 °C, 600 °C, 700 °C, and 800 °C) for 6 h to lead the decomposition of the nitrate precursor and the conversion into respective oxides. The silica templates were removed with 8 wt% HF aqueous solution and washed by distilled water. A black powder product of mesoporous Co₃O₄ particles was obtained by centrifugation and dried at room temperature. The obtained samples were denoted as Co₃O₄-“T”, where “T” indicated the calcination temperatures.

2.2.3. Measurement of Catalytic Activity

The catalytic activity of mesoporous Co_3O_4 (Co_3O_4 -“T”) for CO oxidation was measured by using a flow-type fixed-bed pyrex reactor (i.d. = 5 mm) with a “U” shape as described in the literature [21]. In general, a standard gas containing 1 vol % CO and 21 vol % O_2 balanced with He was passed through the reactor filled with a catalyst sample in an amount of 100 mg at a rate of flow of $33.3 \text{ ml}\cdot\text{min}^{-1}$ (space velocity = $20,000 \text{ ml}\cdot\text{g}_{\text{-cat}}^{-1}\cdot\text{h}^{-1}$) under atmospheric pressure. Pretreatment was conducted at $450 \text{ }^\circ\text{C}$ for 30 min before catalytic tests and then cooled to a starting reaction temperature in the same stream of 21 vol % O_2 in He. The concentration of CO, O_2 , and CO_2 in the outlet streams were measured by using a gas chromatography (GL Science Inc.) equipped with active carbon column, and TCD and FID detectors. Automatic gas sampling interval of 15 min was employed to measure the conversion of CO under a steady state. Experiments at temperatures below $0 \text{ }^\circ\text{C}$ were controlled by using ethanol/liquid nitrogen or ethanol/dry ice cooling solution. Kinetic measurements for CO oxidation over mesoporous Co_3O_4 (Co_3O_4 -“T”) were conducted in the temperature range of -87 to $-49 \text{ }^\circ\text{C}$ by changing the space velocity in the range of 2.0×10^4 to $5.2\times 10^5 \text{ ml}\cdot\text{g}_{\text{-cat}}^{-1}\cdot\text{h}^{-1}$.

2.2.4. Characterizations

Powder X-ray diffraction were characterized on a Rigaku Ultima III X-ray diffractometer with $\text{CuK}\alpha$ radiation ($\lambda = 0.154 \text{ nm}$). The SAXS (Small Angle X-ray Scattering) measurement ($\text{Cu } 0.154 \text{ nm}$) was carried out using Nano Viewer (Rigaku Corp., Japan). The surface morphology of the materials was observed with Hitachi S-4800 and S-5500 SEM by using an acceleration voltage of 5.0 kV. The microstructures of the mesoporous Co_3O_4 were confirmed by high-resolution transmission electron microscopy (HRTEM) on a JEOL JEM-2000 operated at 200kV. Selected-area electron diffraction (ED) was used to determine the atomic crystallinity of the materials. N_2 adsorption-desorption analysis was carried out using a Quantachrome Autosorb-1C at liquid nitrogen temperature 77 K with prior degassing at $120 \text{ }^\circ\text{C}$ for 6 h. The typical sample weight used in the measurement was 100-200 mg. Specific surface area, S_{BET} , was deduced from the relative pressure range of 0.05-0.2, the region at which BET plot

is linear. Average pore diameter, D_{BJH} , was calculated from the pore size distribution curves of the adsorption branch isotherm by using BJH method.

2.3. Results and Discussion

2.3.1. Synthesis and Characterization of Mesoporous Co_3O_4

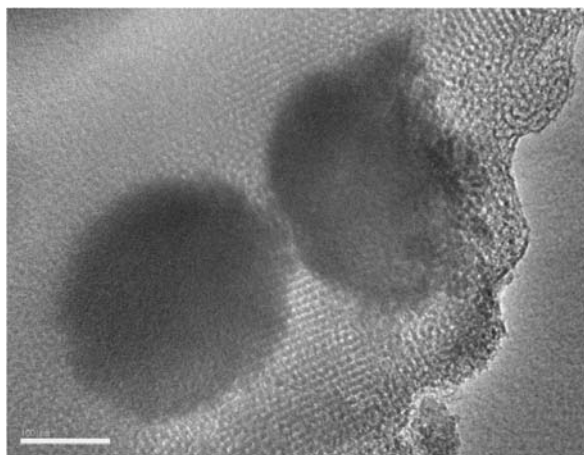


Figure 2.1 Typical TEM image of mesoporous silica KIT-6 with Co sources before the calcination (conversion to Co_3O_4 crystals).

Figure 2.1 shows typical TEM image of the KIT-6 composite with the impregnated Co sources before the calcination (conversion to Co_3O_4 crystals). The mesopores were partially filled with Co sources (as indicated by the dark areas). Any deposited Co sources were not observed outside the silica particles. The size of the Co sources was uniform and the particle size was about 250 nm in diameter. From the images, it is observed that the silica particles cannot be entirely filled by the Co sources. Even if all the mesopores of the KIT-6 are completely filled by $\text{Co}(\text{NO}_3)_2$ aqueous solution, the volume of the cobalt compound would be significantly reduced during the conversion to Co_3O_4 crystals. The important step of nanocasting utilizing hard templates is the successful loading of precursor into the pores by impregnation. There have been several different ways, such as surface modification method, two solvents method, evaporation method, melt impregnation method (template is ground with the solid precursor and then melted for the impregnation), and solid-liquid method. Among all

the methods, I consider that the incipient wetness impregnation method is suitable for easy loading of the precursor. In this method, the precursor solution is loaded into the pores by capillary forces and the volume of the saturated precursor solution is restricted to the total pore volume of the matrix (or mesoporous template). In the present work, mesoporous silica KIT-6 powders were mixed with cobalt nitrate solution and kept static at 60 °C over 12 hours. Thus, by simplifying the method, long periods of stirring and the uncontrollable effects of grinding can be avoided, realizing a high reproductively.

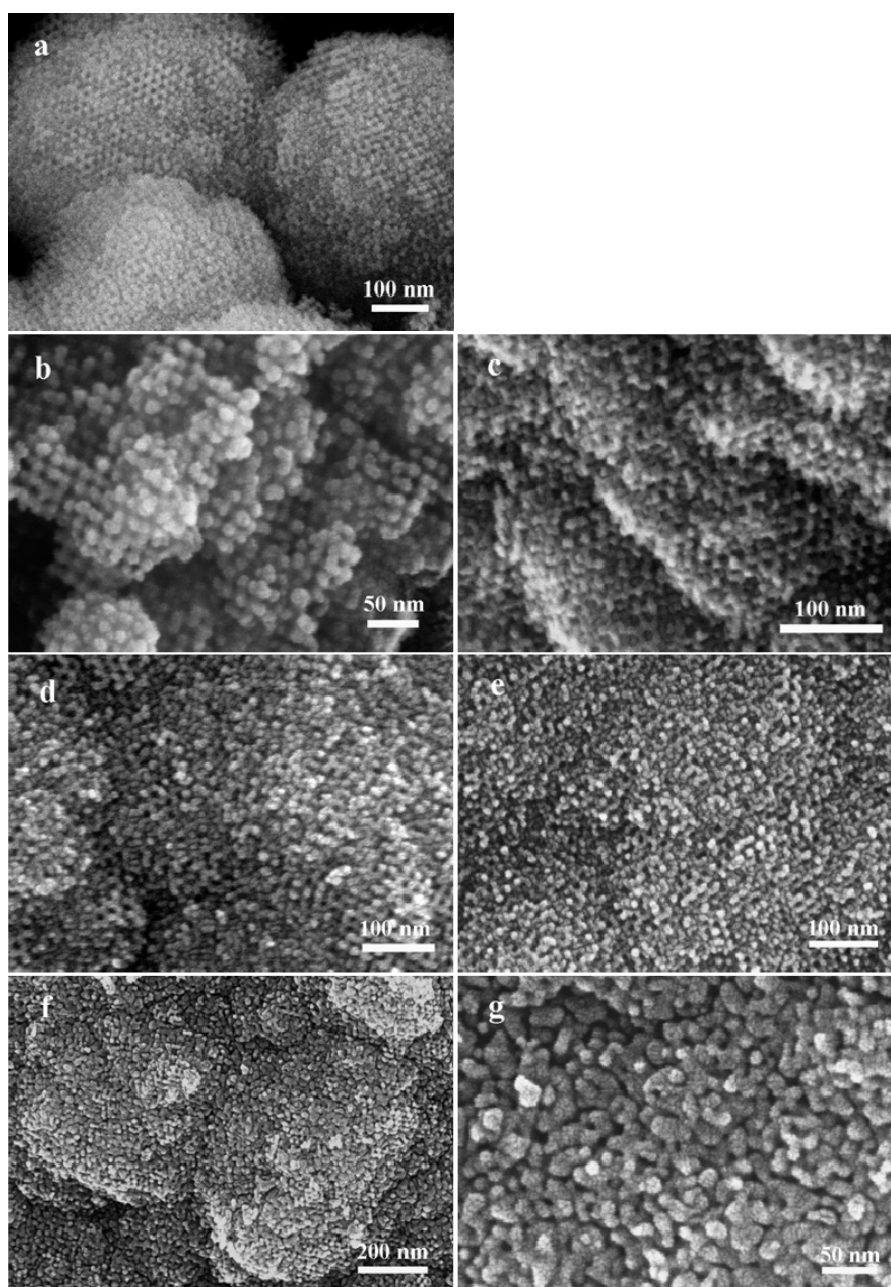


Figure 2.2 Highly magnified SEM images of mesoporous Co_3O_4 prepared at the different calcination temperatures (a: 450 °C, b-c: 500 °C, d: 600 °C, e: 700 °C, and f-g: 800 °C).

The mesostructures of the obtained Co_3O_4 replicas (Co_3O_4 -“T”) was examined by SEM and TEM observation (**Figure 2.2** and **2.3**). The highly ordered mesostructures were observed uniformly for all the particles. Two types of the replica structures were mixed. In almost all the parts, an inverse double gyroid mesostructure was formed. In this case, the Co_3O_4 was deposited inside the both sides of *Ia-3d* mesopore system. But, in a very few cases, the Co_3O_4 deposition in only one side pore was confirmed [36].

Although it was previously reported that the surface of the original KIT-6 mesoporous silica particles shows distorted (or disordered) mesostructures [37], no disorderly arranged Co_3O_4 nanowires were observed on the entire top surface of the particles (**Figure 2.2**). The Co_3O_4 crystallization started from the inside areas of the mesoporous silica particles and did not reach until the particle surface (**Figure 2.1**). This idea is well supported by the fact that the size of the obtained Co_3O_4 particle was much smaller rather than that of the original KIT-6 particles (micrometer scale) [36, 37].

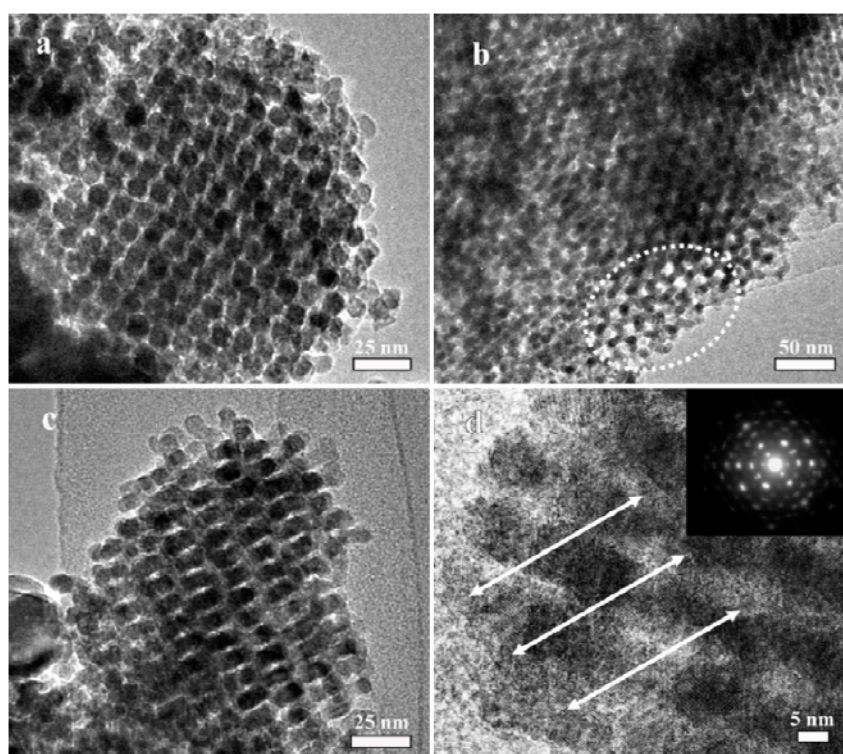


Figure 2.3 (a-c) TEM images of the mesoporous Co_3O_4 -450. The area in which the Co_3O_4 deposition happened in one side pore was indicated by circle. (d) Highly magnified TEM image and the corresponding electron diffraction (ED) patterns. The lattice fringes running in the same direction are indicated by arrows.

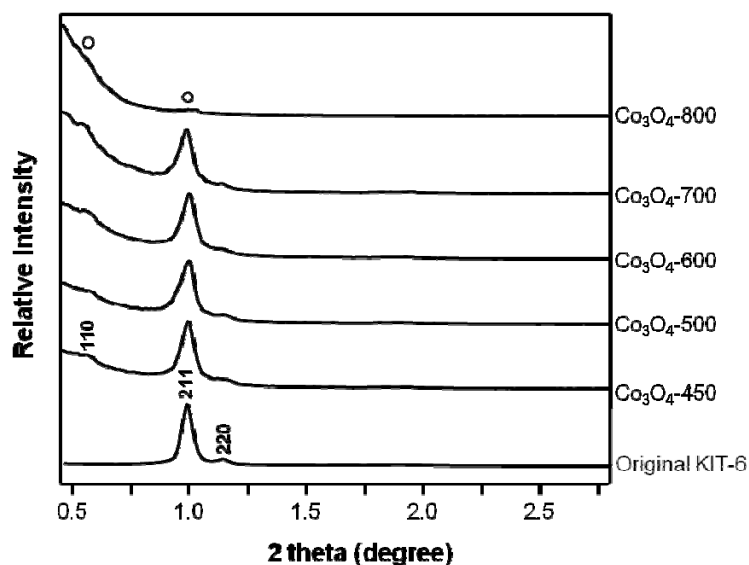


Figure 2.4 Small Angle X-ray Scattering (SAXS) profiles of mesoporous KIT-6 and Co_3O_4 materials. The circles are drawn to point the peak positions of 110 and 211 reflections.

From the above SEM and TEM observation and SAXS measurements, it was proved that almost the entire nitrate precursor was impregnated or moved into the mesopores of the parent KIT-6 templates during the calcination steps. Such a high level of infiltration using the solution precursor is necessary for replication without Co_3O_4 bulk deposition outside the mesopores. The crystallinity in the pore walls of mesoporous Co_3O_4 particles was investigated by high resolution TEM image and selected-area electron diffraction (ED) patterns (**Figure 2.3d**). Several lattice fringes oriented in the same direction were observed. The ED patterns corresponded to the face centered cubic phase of a spinel Co_3O_4 structure.

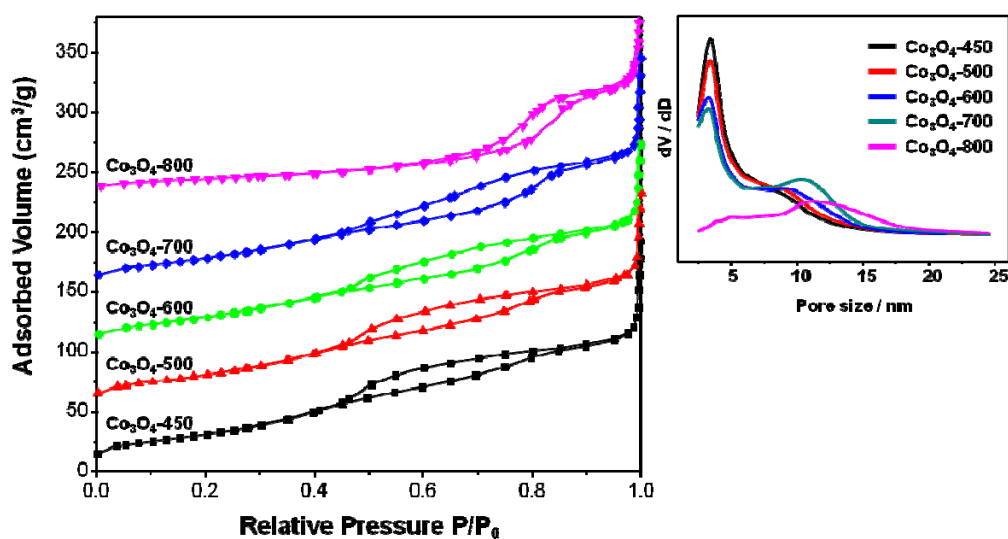


Figure 2.5 Nitrogen adsorption/desorption isotherms of mesoporous Co_3O_4 materials prepared at different calcination temperatures. The inset image represents the average pore size distributions.

Figure 2.5 shows the N_2 adsorption-desorption isotherms and BJH pore size distributions of Co_3O_4 -“T” calcined at different temperatures. The isotherms obtained for Co_3O_4 -“T” were type IV patterns with sharp capillary condensation with hysteresis loops. All the samples except Co_3O_4 -800 exhibited adsorption isotherms with a broad capillary condensation starting about $P/P_0 = 0.45$. The surface areas and pore-size distribution in the mesoporous Co_3O_4 -“T” were examined by the adsorption isotherms, the results of which are summarized in **Table 2.1**. In general, the BET surface areas and the pore volumes of the porous metal oxides (prepared using a “soft” template) decrease with the increase of calcination temperature. In this study, significant changes were not observed for the BET surface areas and the pore volumes in the Co_3O_4 -“T” except Co_3O_4 -800 (**Table 2.1**). The textural parameters can be retained even at 700 °C. The average pore-sizes for all the Co_3O_4 -“T” (except Co_3O_4 -800) were almost the same (around 3.3 nm). The narrow pore size distribution around 3.0 nm corresponds to the mesopore that was produced by the removal of pore walls of the KIT-6 template. This value is good agreement with the wall thickness of the original KIT-6 (**Table 2.1**). Apart from the mesopore distribution at around 3.3 nm, a broad pore distribution in the range of 8-12 nm was confirmed, which is derived from voids caused by lower symmetry between the Co_3O_4 nanowires which were deposited inside one side

mesopores [36]. The broad pore size distribution centered at 8 nm (Co₃O₄-450) was gradually shifted to 12 nm (Co₃O₄-800) with the increase in the applied calcination temperatures.

Table 2.1 Structural parameters of mesoporous Co₃O₄ and KIT-6 mesoporous silica.

Sample (Co ₃ O ₄ -“T”)	S _{BET} (m ² •g ⁻¹)	V _t (cm ³ •g ⁻¹)	D _{BJH} (nm)	Co ₃ O ₄ crystal size (nm)
Co ₃ O ₄ -450	123	0.197	3.3, 8.5	14.5 ± 0.5
Co ₃ O ₄ -500	119	0.194	3.3, 8.7	15.4 ± 0.5
Co ₃ O ₄ -600	117	0.190	3.3, 9.2	15.2 ± 0.5
Co ₃ O ₄ -700	114	0.189	3.2, 10.3	14.7 ± 0.5
Co ₃ O ₄ -800	54	0.176	4.0, 11.0	19.5 ± 0.5
KIT-6	731	0.998	7.8*, 3.2*	---

*The pore-size distribution curve of mesoporous silica KIT-6 shows both the main mesopore (7.8 nm) and the complementary pore (3.2 nm). The pore wall thickness can be calculated to be 3.4 nm, because the unit cell of an *Ia-3d* mesostructure is measured to be 22.3 nm by SAXS profile (**Figure 2.4**).

To make it clear the reason why the mesostructural ordering was dramatically decreased after 800 °C calcination, I focused on the crystallinity of the pore walls and measured wide-angle XRD patterns for each sample. The wide angle XRD patterns shown in **Figure 2.6** revealed that all the peaks are indexed as face centered cubic phase of spinel Co₃O₄ with lattice constant 8.08 Å. Any significant changes were not observed from the wide angle XRD patterns. To investigate more in detail, I have calculated the crystal size by the following Scherer’s equation:

$$D_p = K \cdot \lambda / (\beta \cdot \cos \theta)$$

(Where the D_p is the mean size of the ordered domains of the crystallite, the K is the shape factor 0.84 for cubic lattices, the λ is the x-ray wavelength, the β is full width at half maximum (FWHM) in radians, and θ is the Bragg angle.)

The crystallite sizes of the mesoporous Co₃O₄-“T” particles were calculated from the 311 reflections of the wide angle XRD patterns (**Figure 2.6**) and were given in **Table 2.1**. When the calcination temperatures were changed from 450 °C to 700 °C, the

crystallite size did not change significantly. But, the size of the Co_3O_4 -800 particles increased appreciably and significantly than the other samples. Hence it was clear from wide angle XRD patterns and the Scherer equation that the crystallite size increased notably upon further increasing the calcination temperature beyond 700 °C. Upon increasing the calcination temperature beyond 700 °C, the further crystal growth proceeds to form much larger size Co_3O_4 crystals in the mesoporous silica matrix. In other words, the silica matrix could not prevent the crystal growth under such higher temperatures. Therefore, the samples after the removal of silica showed the loss of an ordered structure, which was also observed in SAXS patterns (**Figure 2.4**).

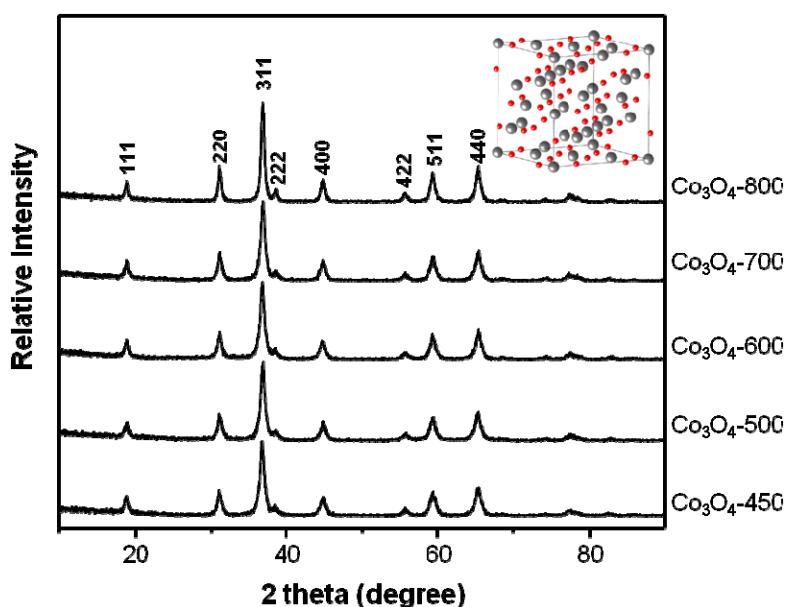


Figure 2.6 Wide-angle XRD patterns of mesoporous Co_3O_4 materials prepared at different calcination temperatures.

2.3.2. Catalytic Activity of Mesoporous Co_3O_4

Figure 2.7 shows light-off curves of mesoporous Co_3O_4 calcined at various temperatures (from 450 °C to 800 °C) in CO oxidation reaction conducted under the same space velocity. All samples gave a quite high catalytic activity, for example, 50% conversion temperature (T_{50}) appeared at -72 °C over the sample calcined at 450 °C. The difference of T_{50} between the highest and lowest catalytic activity within 10 °C,

indicating the catalytic activities of these samples were at a similar level. The catalytic activity of our mesoporous Co_3O_4 was higher than those of Co_3O_4 nanomaterials reported by others [14, 21, 31, 33]. For example, T_{50} of mesoporous Co_3O_4 prepared by using KIT-6 templates aged at different hydrothermal temperatures appeared at 4 °C [31]. Also, Ren *et al* recently reported the catalytic activity of mesoporous Co_3O_4 prepared by using KIT-6 as a hard template and reported the T_{50} at -62 °C [14].

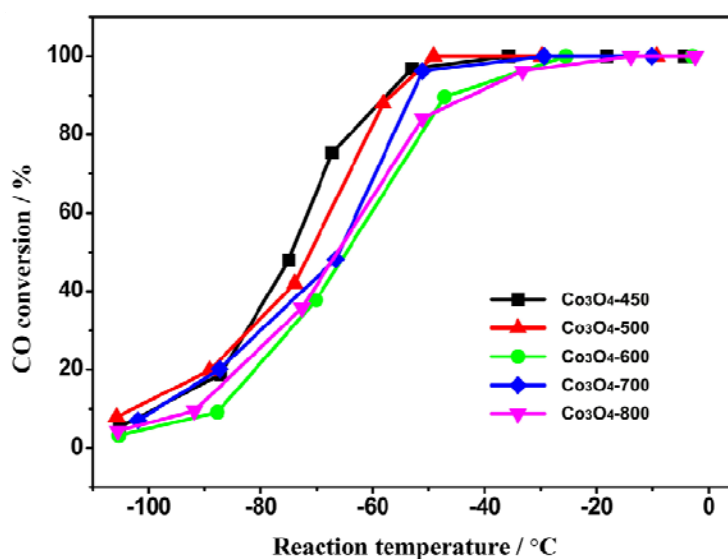


Figure 2.7 Conversion as a function of reaction temperature for CO oxidation on mesoporous Co_3O_4 samples prepared at different calcination temperatures. The stream consisted of 1 vol% CO and 21 vol% O_2 in He, and the gas hourly space velocity was $2 \times 10^4 \text{ ml} \cdot \text{h}^{-1} \cdot \text{g}_{\text{cat}}^{-1}$ (■: 450°C, ▲: 500°C, ●: 600°C, ◆: 700°C, ▼: 800 °C).

Figure 2.8 displays Arrhenius plots for CO oxidation over mesoporous Co_3O_4 nanoparticles calcined at 450 °C and 800 °C. The apparent activation energies (E_a) calculated from the Arrhenius plots were the same $25 \text{ kJ} \cdot \text{mol}^{-1}$ for both the samples. The mass-normalized pre-exponential factors (A) were 4.4×10^{22} and 4.7×10^{22} molecules $(\text{m}^2)^{-1} \cdot \text{s}^{-1}$ (5.4×10^{24} and 2.6×10^{24} molecules $\cdot \text{g}^{-1} \cdot \text{s}^{-1}$) for mesoporous Co_3O_4 calcined at 450 °C and 800 °C, respectively. The same values of E_a and much closer values of A per unit area indicated that samples calcined at low and high temperature possessed same catalytic property, which is coincided with the results obtained from light-off

curves in **Figure 2.7**. Even though the surface area was drastically reduced to $54 \text{ m}^2\cdot\text{g}^{-1}$ after $800 \text{ }^\circ\text{C}$ calcination, the catalytic activities were not changed substantially.

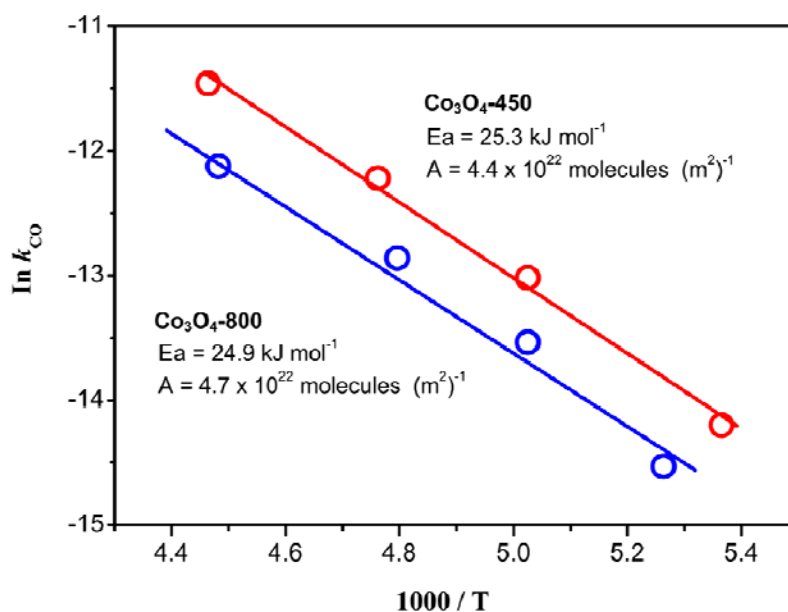


Figure 2.8 Arrhenius plots for the reaction rate constant (activation energy, E_a) in the temperature range of $-87 \text{ }^\circ\text{C}$ to $-49 \text{ }^\circ\text{C}$. The stream consisted of 1 vol% CO and 21 vol% O₂ in He, and the gas hourly space velocity was changed in the range of 2.0×10^4 to $5.2 \times 10^5 \text{ ml}\cdot\text{h}^{-1}\cdot\text{g}_{\text{cat}}^{-1}$ in order to obtain CO conversion below 15 % for differential reactor assumption.

The activation energy of our mesoporous Co₃O₄ was much higher than Co₃O₄ with irregular shape ($E_a=50 \text{ kJ}\cdot\text{mol}^{-1}$) [33], though still not over Co₃O₄ rod ($E_a=22 \text{ kJ}\cdot\text{mol}^{-1}$, $A=8.0 \times 10^{24} \text{ molecules g}^{-1}\cdot\text{s}^{-1}$) that is the most catalytic active Co₃O₄ nanocrystals until now [34]. It was previously reported that the high catalytic activity of the Co₃O₄ rod was driven by the plenty of Co³⁺ exposed to the surfaces on {110} plane [34] and the Co₃O₄ nanocrystals possessed 41% of all the rod surface. From the above background, I consider that the percentage of {110} planes exposed on the whole surface more critically affects the activity for low temperature CO oxidation.

As seen in the results of HR-TEM observation (**Figure 2.3d**), the single crystallinity was extended across over several mesopores. Therefore, several planes including {110} planes were thought to be exposed on the mesopore surface of the

mesoporous Co_3O_4 , although the exposure of crystal plane was difficult to be determined. It was reported that $\{110\}$ exposed on mesoporous Co_3O_4 particle to give a high catalytic activity in ethylene oxidation [38]. From the wide-angle XRD profiles for mesoporous Co_3O_4 calcined at various temperatures, the relative intensities for each peak were not changed, although the values of the FWHM were varied (*i.e.*, the crystal size were increased with the increase of the calcination temperatures.) Any crystal growth in any particular lattice direction was not observed. Therefore, we can roughly understand that the percentage of the exposed $\{110\}$ planes is almost the same among all samples. Therefore, both Ea and A values were similar between Co_3O_4 -450 and Co_3O_4 -800. A little difference of T_{50} is derived from large difference of the surface areas.

2.4. Conclusion

I have prepared mesoporous Co_3O_4 catalysts *via* hard templating method at different calcination temperatures. In the range of calcination temperatures from 450 °C to 700 °C, significant changes were not observed in the textural parameters of these mesoporous Co_3O_4 catalysts. Upon increasing the calcination temperature up to 800 °C, the size of the crystallite increased drastically and the surface areas and mesostructural orderings decreased. But, crystal growth in any particular lattice direction was not confirmed. When all Co_3O_4 -“T” were tested in low temperature CO oxidation reaction, all the materials showed higher catalytic activity compared to other mesoporous Co_3O_4 catalysts reported previously [14, 31]. T_{50} appeared at -72 °C over the sample calcined at 450 °C. Both E_a and A values were essentially similar between Co_3O_4 -450 and Co_3O_4 -800, although there was large difference in the surface areas. This information will help the design of new mesoporous materials with a high oxidation catalytic activity.

References

- [1] T. Yanagisawa, T. Shimizu, and K. Kuroda, *Bull. Chem. Soc. Jpn.*, **63**, 988 (1990).
- [2] S. Inagaki, Y. Fukushima, and K. Kuroda, *J. Chem. Soc. Chem. Commun.*, 680 (1993).
- [3] C. T. Kresge, M. E. Leonowicz, W. J. Roth, J. C. Vartuli, and J. S. Beck, *Nature*, **359**, 710 (1992).
- [4] J. S. Beck, J. C. Vartuli, W. J. Roth, M. E. Leonowicz, C. T. Kresge, K. D. Schmitt, C. T. W. Chu, D. H. Olsen, E. W. Sheppard, S. B. McCullen, J. B. Higgins, and J. L. Schlenker, *J. Am. Chem. Soc.*, **114**, 10834 (1992).
- [5] A. H. Lu, and F. Schüth, *Adv. Mater.*, **18**, 1793 (2006).
- [6] K. P. Gierszal, T. W. Kim, R. Ryoo, and M. Jaroniec, *J. Phys. Chem. B*, **109**, 23263 (2005).
- [7] K. P. Gierszal, M. Jaroniec, T. W. Kim, J. Kim, and R. Ryoo, *New J. Chem.*, **32**, 981(2008).
- [8] Z. X. Wu, Y. X. Yang, D. Gu, Q. Li, D. Feng, Z. X. Chen, B. Tu, P. A. Webley, and D. Y. Zhao, *Small*, **5**, 2738 (2009).
- [9] W. B. Yue, X. X. Xu, J. T. S. Irvine, P. S. Attidekou, C. Liu, H. Y. He, D. Y. Zhao, and W. Z. Zhou, *Chem. Mater.*, **21**, 2540 (2009).
- [10] Y. F. Shi, Y. Wan, R. Y. Zhang, and D. Y. Zhao, *Adv. Funct. Mater.*, **18**, 2436 (2008).
- [11] A. Takai, Y. Doi, Y. Yamauchi, and K. Kuroda, *J. Phys. Chem. C*, **114**, 7586 (2010).
- [12] M. Cabo, E. Pellicer, E. Rossinyol, O. Castell, S. Surinach, and M. D. Baro, *Crystal Growth & Design*, **9**, 4814 (2009).
- [13] B. Tian, X. Liu, H. Yang, S. Xie, C. Yu, B. Tu, and D. Zhao, *Adv. Mater.*, **15**, 1370 (2003).
- [14] Y. Ren, Z. Ma, L. Qian, S. Dai, H. He, and P. G. Bruce, *Catal. Lett.*, **131**, 146 (2009).
- [15] Y. Kim, S. K. Shi, and J. H. White, *J. Catal.*, **61**, 61 (1980).
- [16] Y. Y. Yao, *J. Catal.*, **89**, 152 (1984).

- [17] M. Olsbye, R. Wendelbo, and T. Akporiaye, *Appl. Catal. A*, **152**, 127 (1997).
- [18] Y.Z. Wang, Y.X. Zhao, C.G. Ga, and D.S. Liu, *Catal. Lett.*, **116**, 136 (2007).
- [19] H. Tüysüz, L. Yong, C. Weidenthaler, and F. Schüth, *J. Am. Chem. Soc.*, **130**, 14108 (2008).
- [20] M. J. Jia, X. X. Zhang, Y. G. Tao, G. Y. Wang, X. H. Cui, C. L. Zhang, and T. H. Wu, *Chem. J. Chin. Univ.*, **20**, 637 (1999).
- [21] D. A. H. Cunningham, T. Kobayashi, N. Kamijo, and M. Haruta, *Catal. Lett.*, **25**, 257 (1994).
- [22] P. Thormählen, M. Skoglundh, E. Fridell, and B. Andersson, *J. Catal.*, **188**, 300 (1999).
- [23] W. Yue, A.H. Hill, A. Harrison, and W. Zhou, *Chem. Commun.*, 2518 (2007).
- [24] S. Feng, M. Zheng, N. Li, G. Ji, and J. Cao, *Chem. Lett.*, **38**, 1050 (2009).
- [25] C. Dickinson, W. Zhou, R.P. Hodgkins, Y. Shi, D. Zhao, and H. He, *Chem. Mater.*, **18**, 3088 (2006).
- [26] W. Yue, and W. Zhou, *Chem. Mater.*, **19**, 2359 (2007).
- [27] A. Ruplecker, F. Kleitz, E.L. Salabas, and F. Schüth, *Chem. Mater.*, **19**, 485 (2007).
- [28] P. Shu, J. Ruan, C. Gao, H. Li, and S. Che, *Microporous Mesoporous Mater.*, **123**, 314 (2009).
- [29] B. Tian, X. Liu, L.A. Solovyov, Z. Liu, H. Yang, Z. Zhang, S. Xie, F. Zhang, B. Tu, C. Yu, O. Terasaki, and D. Zhao, *J. Am. Chem. Soc.*, **126**, 865 (2004).
- [30] M. Zheng, J. Cao, S. Liao, J. Liu, H. Chen, Y. Zhao, W. Dai, G. Ji, J. Cao, and J. Tao, *J. Phys. Chem. C*, **113**, 3887 (2009).
- [31] H. Tüysüz, M. Comotti, and F. Schüth, *Chem. Commun.*, 4022 (2008).
- [32] W. H. Yang, M. H. Kim, and S. W. Ham, *Catal. Today*, **123**, 94 (2007).
- [33] Y. Yu, T. Takei, H. Ohashi, H. He, X. Zhang, and M. Haruta, *J. Catal.*, **267**, 121 (2009).
- [34] X. Xie, Y. Li, Z.Q. Liu, M. Haruta, and W. Shen, *Nature*, **458**, 746 (2009).
- [35] T. Kim, F. Kleitz, B. Paul, and R. Ryoo, *J. Am. Chem. Soc.*, **127**, 7601. (2005).
- [36] Y. Doi, A. Takai, Y. Sakamoto, O. Terasaki, Y. Yamauchi, and K. Kuroda, *Chem. Commun.*, **46**, 6365 (2010).

- [37] H. Tüysüz, C.W. Lehmann, H. Bongard, B. Tesche, R. Schmidt, and F. Schüth, *J. Am. Chem. Soc.*, **130**, 11510 (2008).
- [38] C. Y. Ma, Z. Mu, J. J. Li, Y. G. Jin, J. Cheng, G. Q. Lu, Z. P. Hao, and S. Z. Qiao, *J. Am. Chem. Soc.*, **132**, 2608 (2010).

Chapter 3

*Shape- and Size-Controlled Synthesis in Hard Templates:
Sophisticated Chemical Reduction for Mesoporous
Monocrystalline Platinum Nanoparticles*

3.1. Introduction

Since the discovery of mesoporous materials [1-3], various types of ordered mesoporous materials have been synthesized under different conditions and extensively studied with regard to mesostructural controllability, compositional diversity, and morphological flexibility [4]. Currently, mesoporous silica [5-11] and carbon [12-14] nanoparticles (NPs) with controlled particle size have attracted great interest in many potential applications of chromatography, catalysis, catalyst support, and adsorption because the NPs can provide outstanding pore accessibility of guest species from outside. Especially, mesoporous NPs below submicrometer size (normally, below 500 nm) can be utilized in biomedical applications [15-17]. To date, many efforts have been made in the synthesis of mesoporous NPs.

In comparison with silica and carbon, mesoporous metals have fascinating properties inherent to metal frameworks (e.g., high electroconductivity, catalytic activities, etc.) along with the general characteristics of mesoporous materials [18-20]. Therefore, we can anticipate various electrochemical applications that cannot be realized by traditional mesoporous silica. Several approaches for the preparation of mesoporous/mesostructured metals have been reported. Lyotropic liquid crystals made of highly concentrated surfactants or block copolymers have been utilized as soft templates [21-25]. Through chemical or electrochemical reduction, ordered mesoporous metal powders or films, respectively, can be synthesized. However, the ordered arrangement of the rod self-assemblies in the liquid crystals is often distorted during the metal deposition process, and thus, long-range order of the mesoporous structures in the final product is lacking [26]. In comparison with the soft templating method, hard templating is a very attractive pathway that is widely applicable to various compositions [27-34]. Mesoporous silica with a robust framework and high thermal stability is used as a hard template to synthesize a metal replica [35-38]. To date, various Pt nanostructures such as 1D nanowires and 3D nanowire networks have been prepared by using MCM-41 (*p6mm*), SBA-15 (*p6mm*), KIT-6 (*Ia3d*), and MCM-48 (*Ia3d*) as hard templates [35-38]. Chao and co-workers [39, 40] used transmission electron microscopy

(TEM) to investigate the growth mechanism of Pt nanostructures in mesoporous silica matrixes (MCM-48 and MCM-41).

Despite these recent advances in soft and hard templates, the obtained morphologies of mesoporous metals have been very limited to only powders with irregular morphology or films on conductive substrates. The lack of control over the particle sizes and morphologies is a serious problem for further development of mesoporous metals. The shape and size distribution of the NPs are critical parameters of the function and utility for applications. To bring out shape- and size-dependent physicochemical properties, it is extremely important to prepare uniform-sized particles with the same shapes in high yields.

In this chapter, I proposed a new concept for the shape- and size-controlled synthesis of mesoporous metals in hard templates. I demonstrate the facile synthesis of uniformly sized mesoporous Pt NPs by using mesoporous silica KIT-6 (*Ia3d*) as the hard template and ascorbic acid (AA) as the reducing agent. The unit cell parameters and mesopore sizes of the original templates were 21 and 7.9 nm for KIT-6.

3.2. Experimental Process

3.2.1. Synthesis of mesoporous silica KIT-6

Mesoporous silica KIT-6 powder was synthesized according to the previous paper [41]. 4.00 g of Pluronic P123 (PEO₂₀-PPO₇₀-PEO₂₀, Aldrich, Purity 99 %) was dissolved in 144 g of distilled water and 7.90 g of conc. HCl solution (35 wt %) under vigorous stirring. After the complete dissolution, 4.0 g of *n*-butanol (Aldrich, Purity 99.4%) was added under stirring at 35 °C for 1 h. After that, 8.60 g of TEOS (Acros, Purity 98 %) was added to get the homogeneous clear solution. The mixture was further stirred for 24 h at 35 °C, and subsequently hydrothermally heated for 24 h at 100 °C under static conditions in a closed polypropylene bottle. The solid product was filtered without washing and dried up at 80 °C. The surfactant was removed by extraction with water and ethanol followed by calcination at 550 °C for 6 h. From the SAXS measurement, the unit cell for KIT-6 was 21 nm (**Figure 3.4a**). From N₂ adsorption-desorption isotherms, average mesopore was around 7.9 nm (**Figure 3.5a**). Therefore, the silica wall thickness was calculated to be 2.6 nm. Therefore, the silica wall thickness

was calculated to be 3.3 nm. SEM images of both the mesoporous silica KIT-6 and SBA-15 materials as original hard-templates are shown in **Figure 3.1**.

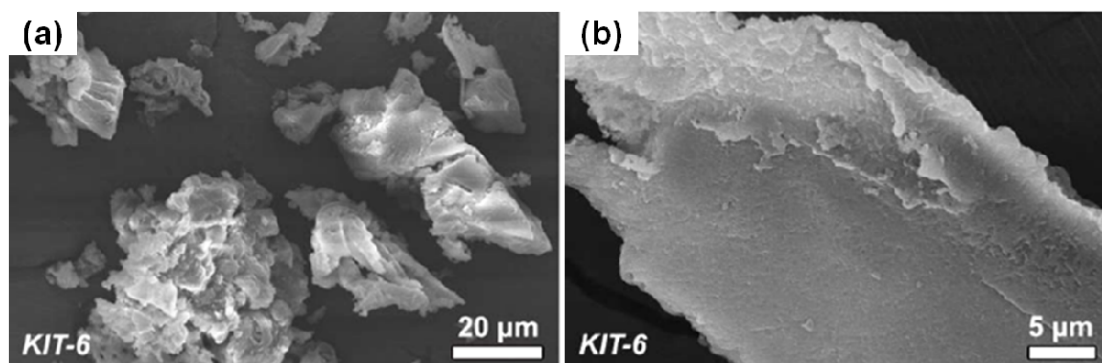


Figure 3.1 SEM images of mesoporous silica KIT-6 as original hard-templates.

3.2.2. Preparation of mesoporous Pt nanoparticles (*meso*-Pt)

All the experimental was carried out at room temperature. In the Pt deposition process, 0.60 g KIT-6 powder was immersed into 2.0 g of K_2PtCl_4 aqueous solution (24.0 wt%). Then, the composite was dried under reduced vacuum condition. After the complete drying, orange-colored powder was obtained. Then, a small amount of 1.0 M ascorbic acid aqueous solution (2.0 ml) was dropped on the powder. The Pt deposition was carried out in a closed vessel for 10 min, 1 h, and 12 h, respectively. Then, the color was gradually changed to black. After the Pt deposition, the samples were washed with 10 % hydrofluoric acid solution. Black powder were centrifuged and washed with distilled water, then dried up at room temperature. The obtained samples were denoted as *meso*-Pt.

3.2.3. Characterization

Small-angle X-ray scattering (SAXS) patterns were obtained by using a Rigaku NANO-Viewer with monochromated Cu $K\alpha$ radiation. The morphology of the samples was observed by using a Hitachi S-4800 field emission scanning electron microscopy (FE-SEM). Transmission electron microscopic (TEM) images were taken by JEOL JEM 2010 (200 kV) to observe the formation of periodic mesostructures inside the particles. To understand an orientation relationship between *Ia-3d* mesostructure and Pt *fcc*

structure, I performed HRTEM and STEM observation by using conventional JEOL JEM-3010 and Cs-corrected JEOL ARM-200F. N₂ adsorption-desorption isotherms were measured by using a Quantachrome Autosorb-1 at liquid nitrogen temperature 77 K with prior degassing at 60 °C for 12 h. The specific surface areas and average pore sizes were calculated by the BET method and the BJH method using the adsorption branches, respectively.

3.3. Results and Discussion

First, mesoporous silica powders were immersed into an aqueous solution of K₂PtCl₄. Next, the composites were dried under reduced vacuum conditions, giving an orange powder. Aqueous AA as a reducing agent was dropped on the powder. After 12 hours, the sample color had totally changed from orange to black, giving a product hereafter called the meso-Pt/silica composite. Finally, to remove the silica, the black powder was washed with HF solution to give mesoporous Pt (meso-Pt). All of the experiments were carried out at room temperature.

Figure 3.2 shows the morphology of the obtained meso-Pt after the removal of the silica template. The low-magnification scanning electron microscopy (SEM) image confirmed that the NPs were isolated from each other and had a narrow particle size distribution. Interestingly, almost all of the NPs showed rhombic dodecahedral morphology (as indicated by the yellow lines in **Figure 3.2b**), although some appeared to be different in the SEM images because different projections were viewed (**Figure 3.3**). The external surface was bounded by 12 planes. The crystal morphology was commensurate with cubic m3m point-group symmetry.

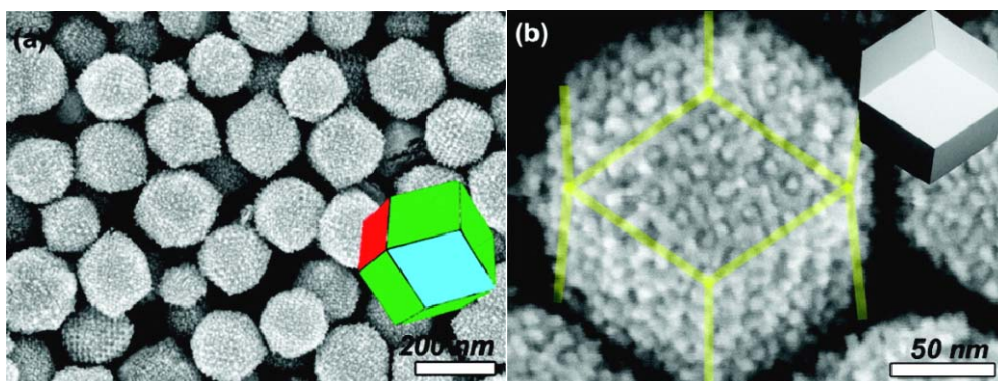


Figure 3.2 (a) Low- and (b) high-magnification SEM images of the obtained mesoporous Pt nanoparticles (*meso*-Pt) prepared with mesoporous silica KIT-6.

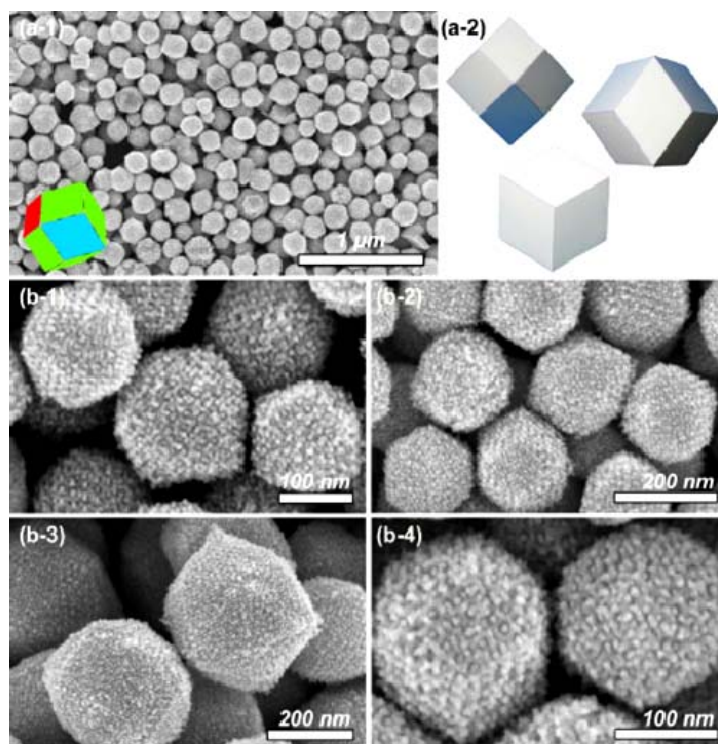


Figure 3.3 (a) Low-magnified and (b) high-magnified SEM images of the obtained mesoporous Pt nanoparticles (*meso*-Pt) prepared with mesoporous silica KIT-6. Several projection images viewed along different directions are shown in (a-2).

From high-magnification SEM images (**Figure 3.2b** and **Figure 3.3b**), it was observed that Pt nanowires replicated from both side pores of a double gyroid mesostructure (i.e., inverse double gyroid structure). Also, the small-angle X-ray scattering (SAXS) peaks were assignable to $Ia3d$, giving the same SAXS profile as for the original KIT-6 mesoporous silica (**Figure 3.4**). This is evidence that the replication of Pt from KIT-6 retained the original symmetry. However, a very weak 110 reflection that was not observed in the profile of the original KIT-6 appeared in the SAXS pattern of *meso*-Pt/silica, meaning that formation of a lower symmetry material partially takes place at this stage. This results from Pt deposition occurring in one side pores of the bicontinuous structure, as indicated by the dotted ellipse in **Figure 3.3**.

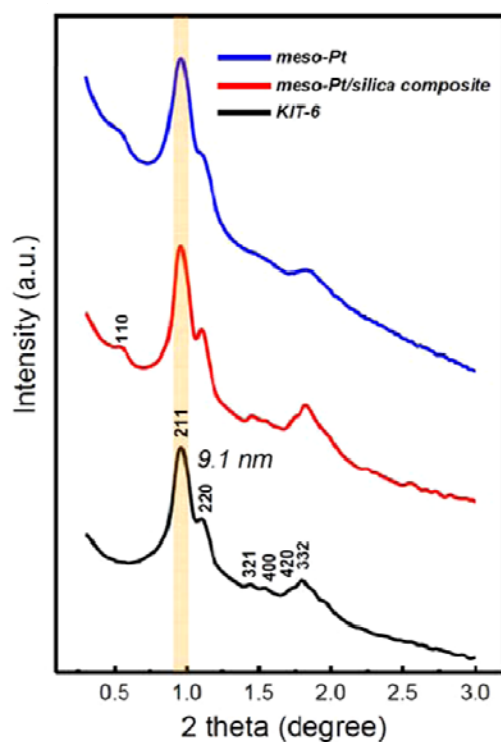


Figure 3.4 SAXS profiles of original mesoporous silica, *meso*-Pt/silica composites (before the silica removal), and *meso*-Pt (after the silica removal). (a) Mesoporous silica KIT-6 system with *Ia-3d* symmetry. The unit cell parameters are 21 nm for KIT-6.

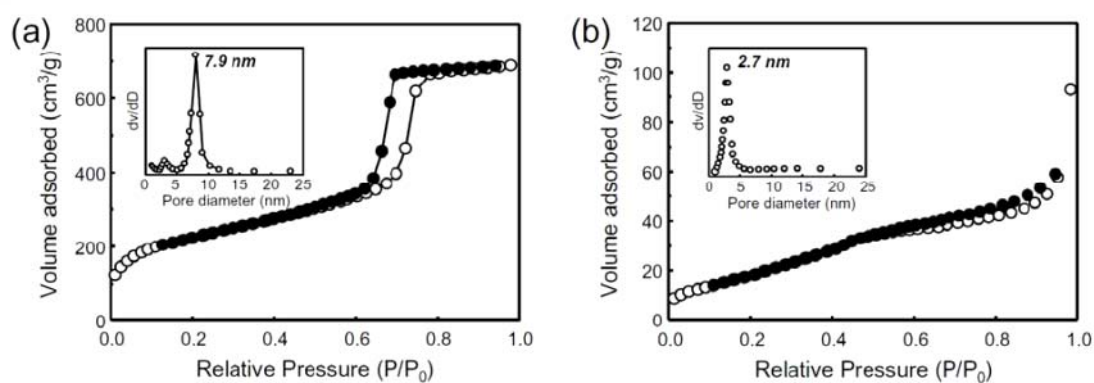


Figure 3.5 N₂ adsorption-desorption isotherms and pore-size distribution curves of (a) original mesoporous silica KIT-6, (b) *meso*-Pt prepared from KIT-6. The BET surface areas are calculated to be 772 m²·g⁻¹ (for original KIT-6), 39.0 m²·g⁻¹ (for *meso*-Pt prepared from KIT-6), respectively.

The N₂ adsorption-desorption isotherm of meso-Pt was a typical type-IV isotherm (**Figure 3.5b**), characteristic of mesoporous materials. The BET surface area and BJH average pore size were calculated to be 39.0 m²·g⁻¹ and 2.7 nm, respectively. The mesopore size of 2.7 nm indicates void space between the Pt nanowires. This value is in good agreement with the wall thickness of the original KIT-6.

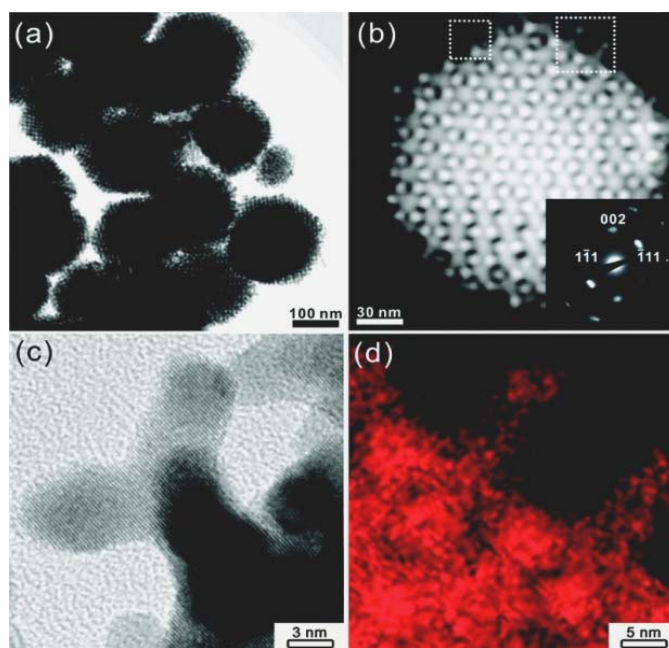


Figure 3.6 (a) Low-magnification TEM image of meso-Pt prepared using KIT-6. (b) ADF-STEM image of one meso-Pt. The inset shows an ED pattern taken from this particle using an incident beam direction parallel to [110] of the Pt *fcc* structure. (c) High-magnification TEM image taken at the left square box in (b). (d) Energy-dispersive spectroscopy elemental (Pt) mapping obtained at the right square box in (b).

TEM images and the elemental mapping are displayed in **Figure 3.6**. The annular dark-field scanning TEM (ADF-STEM) image of one meso-Pt (**Figure 3.6b**) is well-consistent with the image of the original KIT-6 ($Ia3d$ space group) taken with the incident beam parallel to the $\{111\}$ direction. Thus, meso-Pt corresponds to a perfect inversion replica of the original highly ordered KIT-6. Notably, the electron diffraction (ED) pattern (**Figure 3.6b inset**) taken from this same particle showed that the Pt within the framework possessed an almost single-crystalline nature of the Pt face centered cubic (fcc) structure. The wide-angle X-ray diffraction (WAXRD) pattern of meso-Pt could also be assigned to the Pt *fcc* crystal structure (**Figure 3.7**).

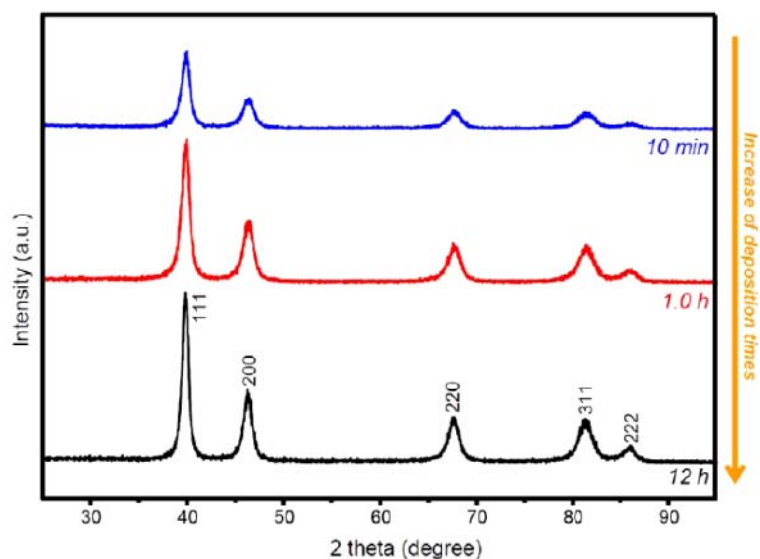


Figure 3.7 Wide-angle XRD patterns for *meso*-Pt prepared by different Pt deposition time in mesoporous silica KIT-6 (10 min, 1.0 hour, and 12 hours). With the increase of the deposition periods, the peak intensities are gradually increased and the full widths at half maximum (FWHM) are decreased from 1.22 (10 min) to 0.93 (12 h).

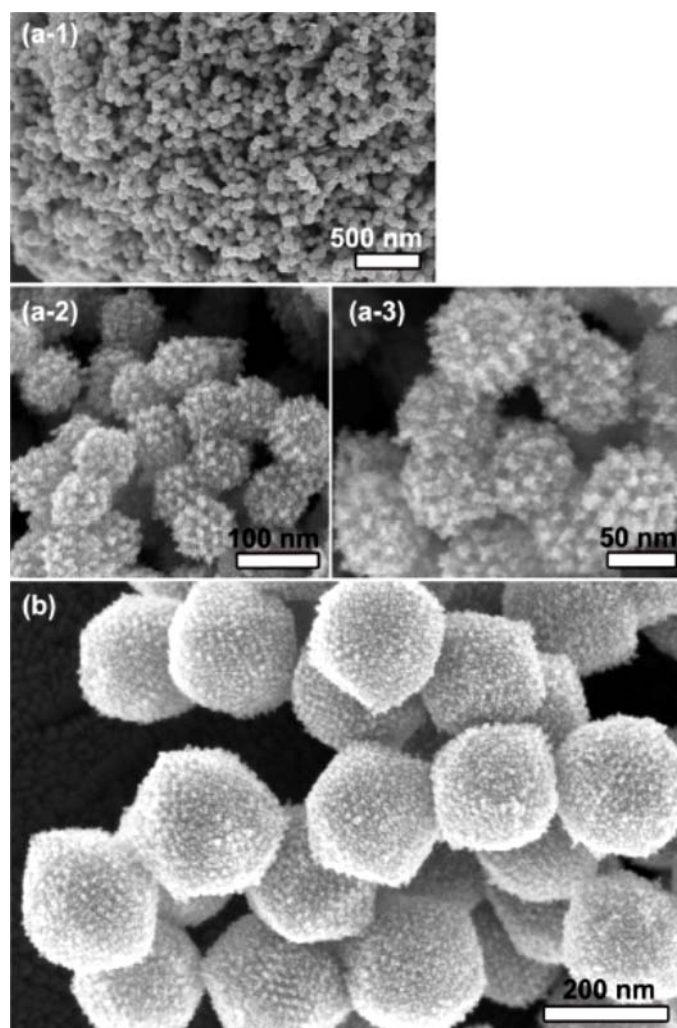


Figure 3.8 SEM images of *meso*-Pt prepared by different Pt deposition time in mesoporous silica KIT-6 ((a) 10 min and (b) 1.0 hour).

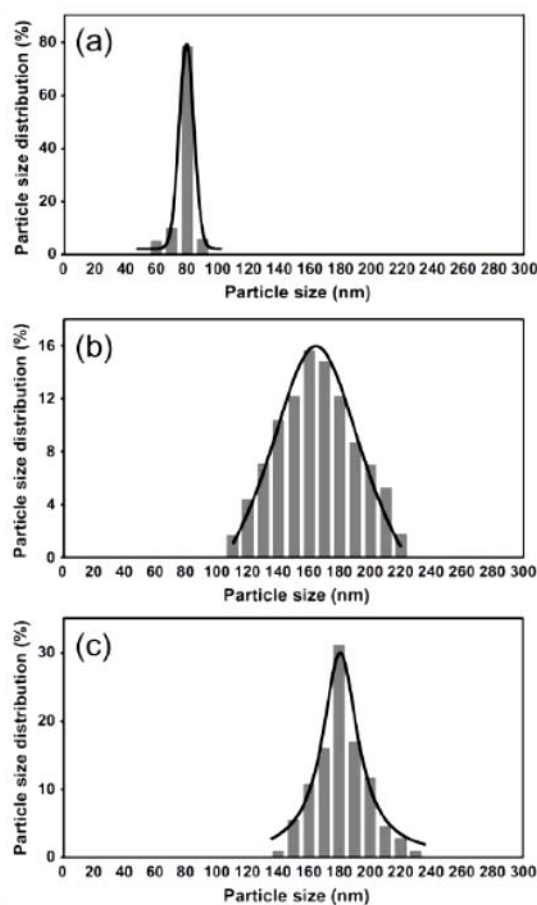


Figure 3.9 Particle size distributions of *meso*-Pt prepared by different Pt deposition time in mesoporous silica KIT-6 ((a) 10 min, (b) 1.0 hour, and (c) 12 hours).

To understand the Pt deposition process, several types of *meso*-Pt with different particle sizes were prepared by changing the reduction time (10 min, 1 h, and 12 h) (**Figures 3.8** and **3.9**). When the reduction time was 10 min, the deposited Pt particles showed a polyhedral shape with an average diameter of 80 nm (**Figures 3.8a** and **3.9a**). With an increase in the deposition period to 1 h, the average particle size gradually increased (up to 160 nm) with retention of the polyhedral shape (**Figures 3.8b** and **3.9b**). After the complete reduction of the Pt sources (12 h), the average particle size reached 180 nm (**Figure 3.2** and **Figure 3.9c**). On the basis of these results, at the beginning stage of the Pt deposition, the nucleation occurs at the center of the particles. Next, Pt grain growth from the nuclei increasingly proceeds, forming larger sized particles, while coherently retaining the Pt atomic crystallinity over the full region of each particle, as shown in **Figure 3.6b,c**.

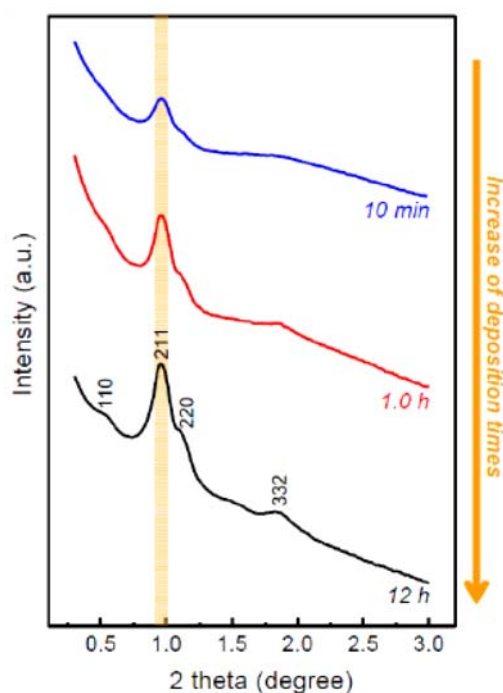


Figure 3.10 SAXS profiles of *meso*-Pt prepared by different Pt deposition time in mesoporous silica KIT-6 (10 min, 1.0 hour, and 12 hours). With the increase of the deposition periods, the peak intensities gradually are increased and the full widths at half maximum (FWHM) are decreased from 0.16 (10 min) to 0.14 (12 h).

With the increase in particle size, the single-domain size of the “mesoporous crystals” became large. Actually, the intensities of the SAXS profiles increased and the full width at half-maximum (fwhm) decreased (**Figure 3.10**). Similarly, the WAXRD patterns (**Figure 3.7**) also showed the increase in peak intensities and decrease in fwhm, indicating the enlargement of Pt *fcc* crystal domains with increasing particle size.

To clarify the reason why each particle shows a “single mesoporous crystal”, the *meso*-Pt/silica composites before the silica removal were carefully investigated by TEM. The deposited Pt particles were distributed over the entire of the silica matrix and isolated from each other. As clearly seen in **Figure 3.11**, the Pt particles were deposited within the same single mesostructural Ia3d domain of the original KIT-6. The domain sizes of “mesoporous crystals” with the same orientation in the KIT-6 template were submicrometer scale (**Figure 3.12**), which is much larger than the particle sizes of the deposited *meso*-Pt particles. Therefore, it is very reasonable that the obtained Pt particles were single mesoporous crystals without defects (**Figure 3.6b**).

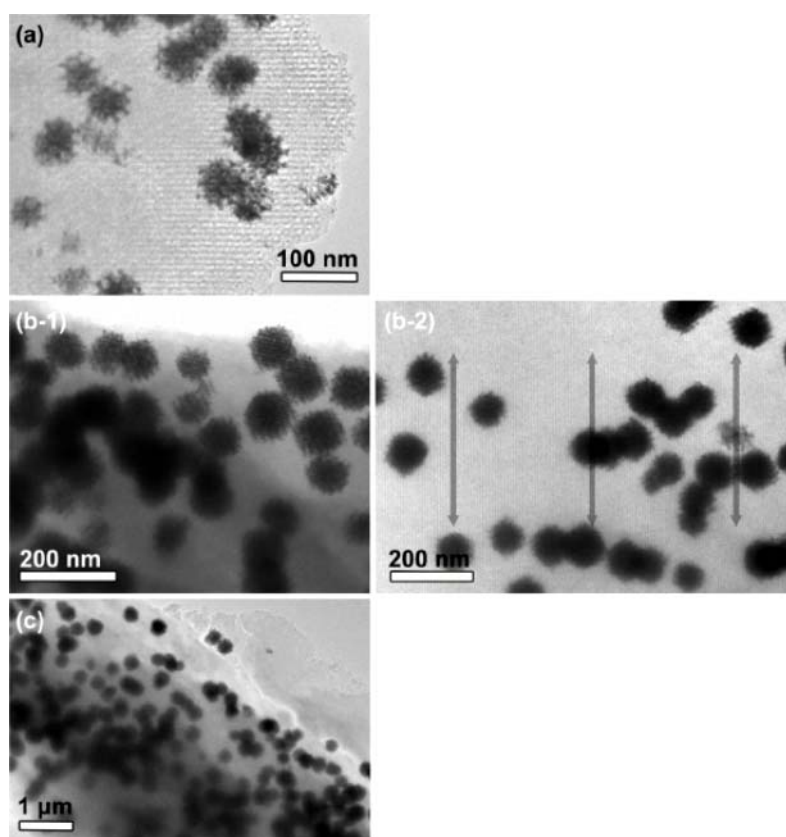


Figure 3.11 TEM images of *meso*-Pt/silica composites prepared by different Pt deposition time in mesoporous silica KIT-6 ((a and b) 10 min and (c) 12 hours). With the increase of the deposition periods, the particle sizes are gradually increased. No Pt deposition is observed outside the mesoporous silica. Therefore, all the deposited Pt particles can possess well-ordered mesostructures replicated from the original mesoporous silica without any formation of by-products. Several nanoparticles deposited within the same mesostructural domain are confirmed in (a) and (b-2).

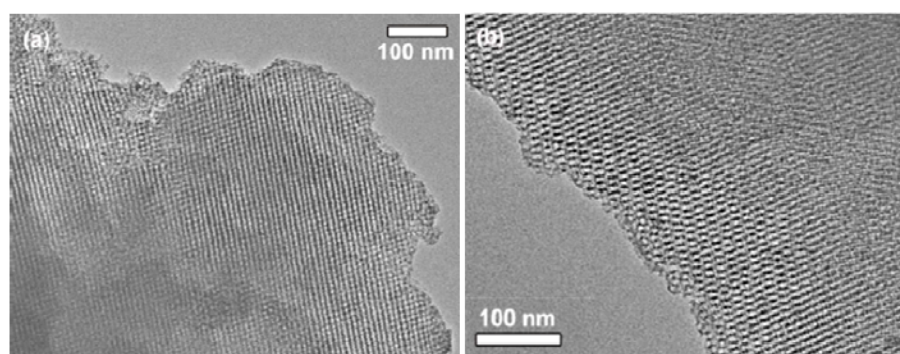


Figure 3.12 Typical TEM images of mesoporous silica KIT-6 with *Ia-3d* symmetry. The domain sizes of mesoporous crystals are sub-micrometer scale which is much larger than the particle sizes of the obtained *meso*-Pt.

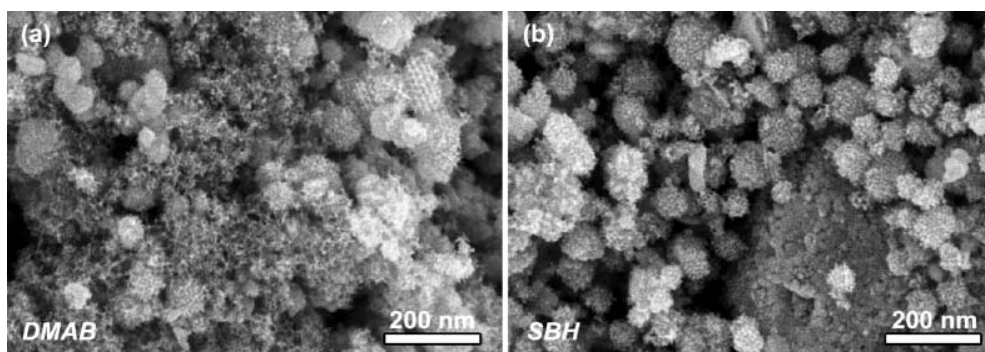


Figure 3.13 SEM images of Pt deposited by using (a) DMAB and (b) SBH as reducing agents.

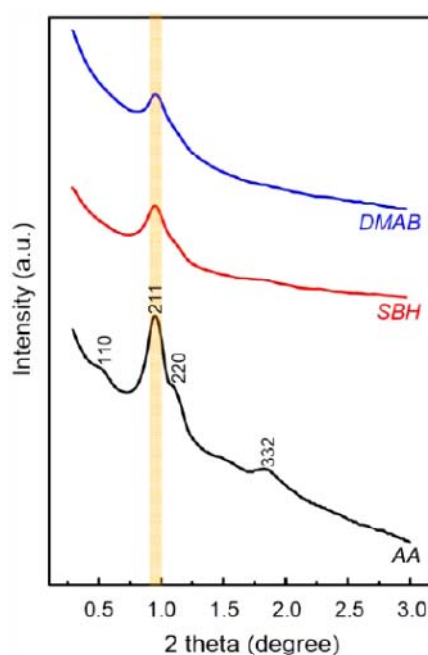


Figure 3.14 SAXS profiles of Pt deposited by using DMAB, SBH, and AA as reducing agents.

The strength of the reducing agent plays the most important key role in the successful preparation of mesoporous Pt nanoparticles with uniform size. For comparison, two different kinds of reducing agents, sodium borohydride (SBH) and dimethylaminoborane (DMAB), were used instead of AA. In both cases, the deposited Pt showed irregular morphology (**Figure 3.13**). Some particles had no ordered mesoporous structures as a result of Pt deposition on the outer surface of the mesoporous silica. The peak intensities in the low-angle range were much smaller than for meso-Pt obtained using AA (**Figure 3.14**), exactly consistent with the SEM images.

These results prove that the use of AA is vital for formation of Pt polyhedra with well-ordered mesostructures. The Pt deposition rate is determined by the strength of the reducing agent. The redox potentials of SBH and DMAB are much lower than that of AA. Therefore, relative to AA, SBH and DMAB are very strong reducing agents and can reduce Pt sources very rapidly. Therefore, SBH and DMAB molecules cannot enter the mesopores and reduce the Pt species inside the mesoporous particles. Especially, SBH reduced the Pt species immediately by a very severe self-decomposition reaction with a large volume of gas, thereby depositing the Pt outside the mesoporous particles (**Figure 3.15**). In contrast, the use of AA can provide enough time to access the Pt sources located inside the mesopores (**Figure 3.11**). In the initial stage of Pt deposition, the AA reduced the Pt species embedded inside the mesopores to deposit the Pt nuclei, and the grain growth proceeded continuously from the primary Pt nuclei. Consequently, the reaction kinetics was critical for high-quality synthesis.

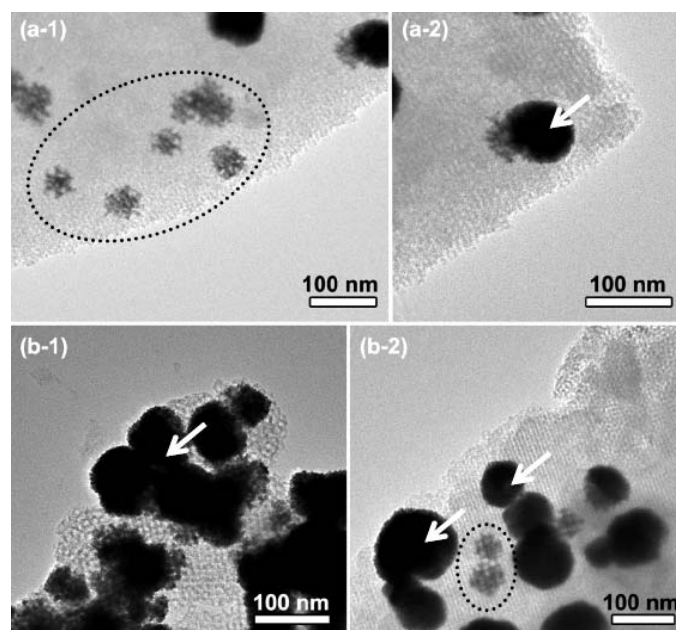


Figure 3.15 TEM images of the deposited Pt by using different reducing agents ((a) DMAB and (b) SBH). The deposited Pt particles inside the silica matrix are indicated by black-colored circles, while the deposited particles outside the silica matrix are indicated by white-colored arrows.

In general, *fcc* metals such as Pt and Au normally have minimum surface energy for $\{111\}$, which is the reason for the formation of typical multiply twinned structures [42]. However, we could not observe such a special crystallographic surface on the top of the Pt network (**Figure 3.2**). In a careful TEM investigation (**Figure 3.16** and **Table 3.1**), we could not find any special crystallographic orientation relationship between the KIT-6 mesostructure (*Ia3d*) and the Pt *fcc* structure (*Fm3m*), although the atomic coherency of the Pt crystal in meso-Pt was confirmed (**Figures 3.6b** and **3.16**). It is therefore natural to assume that the rhombic-dodecahedral shape of the Pt replica synthesized from KIT-6 is not an equilibrium form reflecting the crystal morphology of the Pt *fcc* structure but originates from the KIT-6 mesostructure, that is, the geometry of the double gyroid channels (*Ia3d* symmetry).

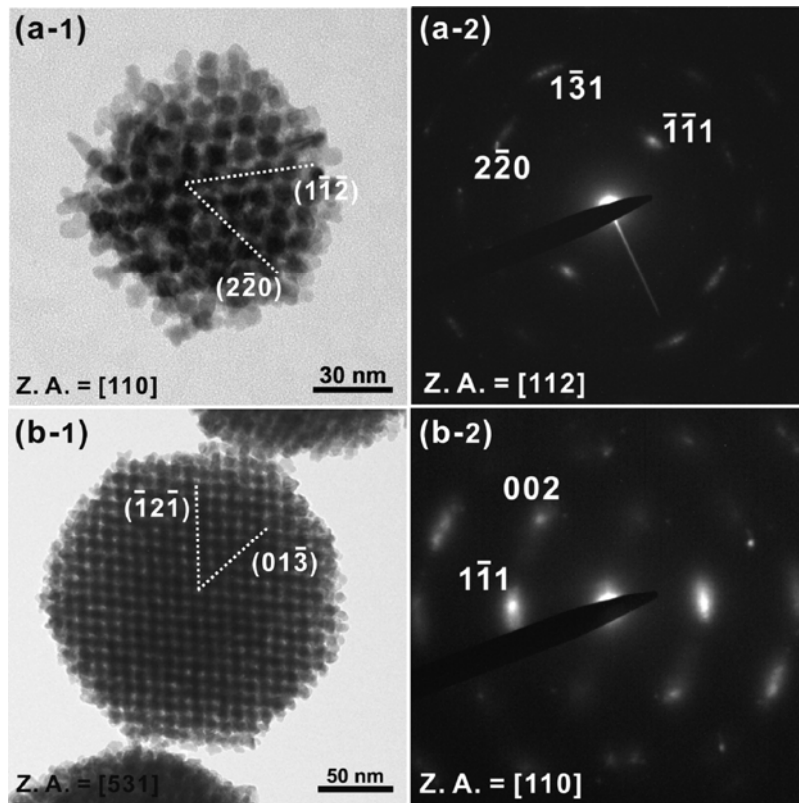


Figure 3.16 (a-1, b-1) Low-magnification bright-field TEM images of meso-Pt and (a-2, b-2) the corresponding ED patterns. Indices are based on (a-1, b-1) the KIT-6 mesostructure and (a-2, b-2) Pt *fcc*.

Table 3.1 Orientation relationships between *Ia-3d* mesostructures and Pt *fcc* structures. Particles (a) and (b) corresponded to the particles (a) and (b) in **Figure 3.16**.

Samples	Parallel directions		Parallel planes	
	Mesostructure	Pt network	Mesostructure	Pt network
Particle a	[110]	[112]	(2 $\bar{2}$ 0)	($\bar{1}\bar{1}$ 1)
Particle b	[531]	[110]	(01 $\bar{3}$)	(002)
Particle c	[110]	[111]	(2 $\bar{2}$ 0)	(0 $\bar{2}$ 2)
Particle d	[012]	[112]	(200)	(351)
Particle e	[012]	[110]	(12 $\bar{1}$)	(1 $\bar{1}$ 1)
Particle f	[111]	[110]	(2 $\bar{1}\bar{1}$)	(002)
Particle g	[531]	[013]	(01 $\bar{3}$)	(3 $\bar{3}$ 1)

From the viewpoint of the electrochemical process, Pt nucleation on the silica walls of KIT-6 is thought to be less than Pt grain growth from the Pt nuclei. In other words, after the nuclei are formed in the early stage of the reaction, most of the reaction time is spent for the growth process. This idea is nicely supported by the fact that (i) the density of the Pt particles (i.e., the number of Pt particles per unit area) was almost constant irrespective of the reaction time (**Figure 3.11**) and (ii) the particle size gradually increased with the reaction time (**Figures 3.8** and **3.9**). Furthermore, coalescence of the particles was not confirmed. Thus, interference among Pt particles to produce their aggregation was rather small. If the density of the nucleation sites were larger, such interference would become relatively large, which would tend to cause the condition of “partition of the space”. In this case, Pt ions diffusing from the associated space to each nucleus (i.e., the Voronoi cell) are likely to contribute to the growth of the Pt particle. The envelope surface must therefore reflect the shape of the Voronoi cell.

In order to discuss further the present formation mechanism, let us assume that the diffusion of the Pt sources as well as that of the reducing agent is fast enough that it would not limit the deposition rate of Pt at every growth front. The Pt network would then grow by tracing the channels of the KIT-6 template outward from the nucleation center with a uniform speed. **Figure 3.17** illustrates an early snapshot of the Pt network,

assuming the nucleation center is a single ternary junction of the gyroid network. At a later stage, the Pt network would exhibit a polyhedral envelope with 24 triangular faces (**Figure 3.17b**). This shape is related to the rhombic dodecahedron observed experimentally, as shown in **Figure 3.2**.

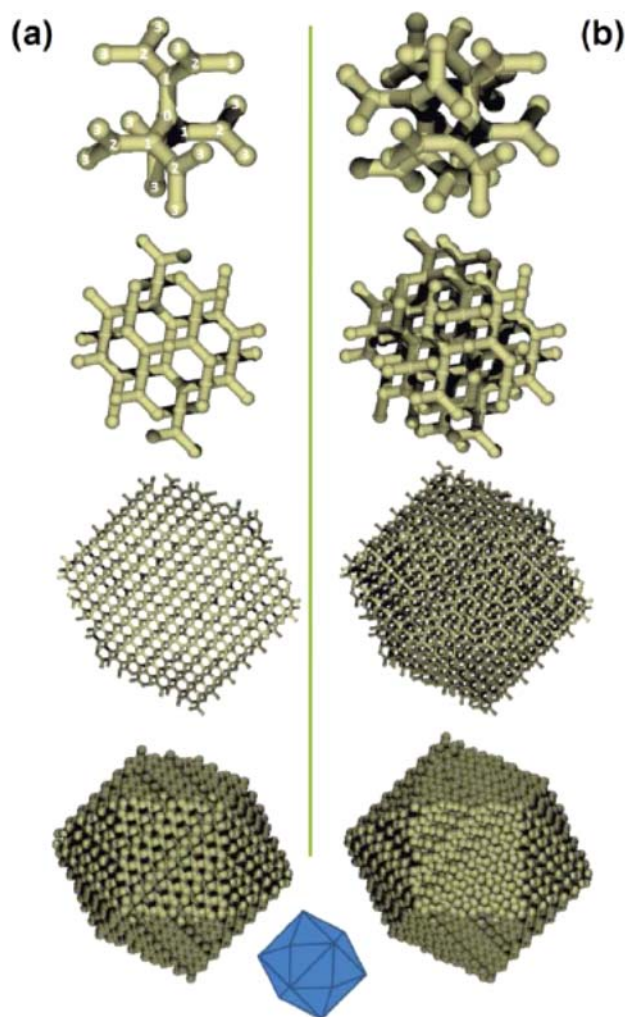


Figure 3.17 Computer simulation of Pt growth in *Ia-3d* mesostructure assuming that the Pt deposition occurs by tracing the channels of KIT-6 template outward from the nucleation center with a uniform speed ((a) A simple model of a growing single Pt network and (b) a double Pt network). The first images in (a) and (b) show that the Pt network reaches the third neighbors (denoted as 3) of the nucleation node (denoted as 0). The last images in (a) and (b) show the Pt network growing at the 25th step. Observe that the envelope of each network is a polyhedron with 24 triangular faces, from which a rhombic dodecahedron can be obtained by expanding the diameters along the three 4-fold axes.

This slight discrepancy may be caused by a bias of the supply of Pt sources along certain directions in the $Ia3d$ channel network. The double gyroid channels in KIT-6 are formed by connections between the branched points that correspond to Wyckoff 16b positions (site symmetry = 32) for $Ia3d$. As shown in **Figure 3.18**, the gyroidal channels are orthogonal to the $\{110\}$ faces of the cubic structure. The formation of rhombic dodecahedra in this study might indicate that the supply of Pt ions and AA can be topologically delayed along the normal to the $\{110\}$ planes.

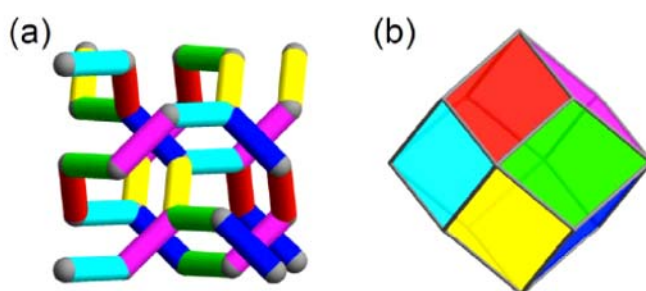


Figure 3.18 Relationship between the orientation of the gyroidal channels and the rhombic dodecahedron shape. All the gyroidal channels shown in (a) are orthogonal to the $\{110\}$ faces of $Ia-3d$ cubic structure shown in Figure (b) (The channels correspond to the same color faces.).

In order to investigate its potential as a catalytic electrode, I measured the methanol electrochemical oxidation reaction on meso-Pt replicated from KIT-6. The electrocatalytic performance recorded in an aqueous solution containing methanol is displayed in **Figure 3.19**. As shown in **Figure 3.19a**, two visible anodic peaks occurring on the positive and negative sweeps, which are typical features of the methanol oxidation process, were confirmed. It is quite interesting that small-sized meso-Pt (deposited for 10 min) showed a remarkably large current density for the electrocatalytic methanol oxidation, in comparison to meso-Pt with larger sizes (deposited for 1 h and 12 h) and commercially available Pt black catalyst (**Figure 3.19d**). In comparison with commercially available Pt catalysts, the onset potentials of meso-Pt were clearly negatively shifted (**Figure 3.19b**). Chronoamperometric curves recorded at 0.6 V proved that small-sized meso-Pt exhibited high durability in its catalytic performance (**Figure 3.19c**). The above results revealed that using small-sized meso-Pt allowed the methanol molecules to access all of the inner mesopores more

easily without serious diffusion resistance. Although 3D connected mesopores are generally known to make the entire surface readily accessible by reactants, the small-sized meso-Pt can more effectively supply the reactants into the mesopores.

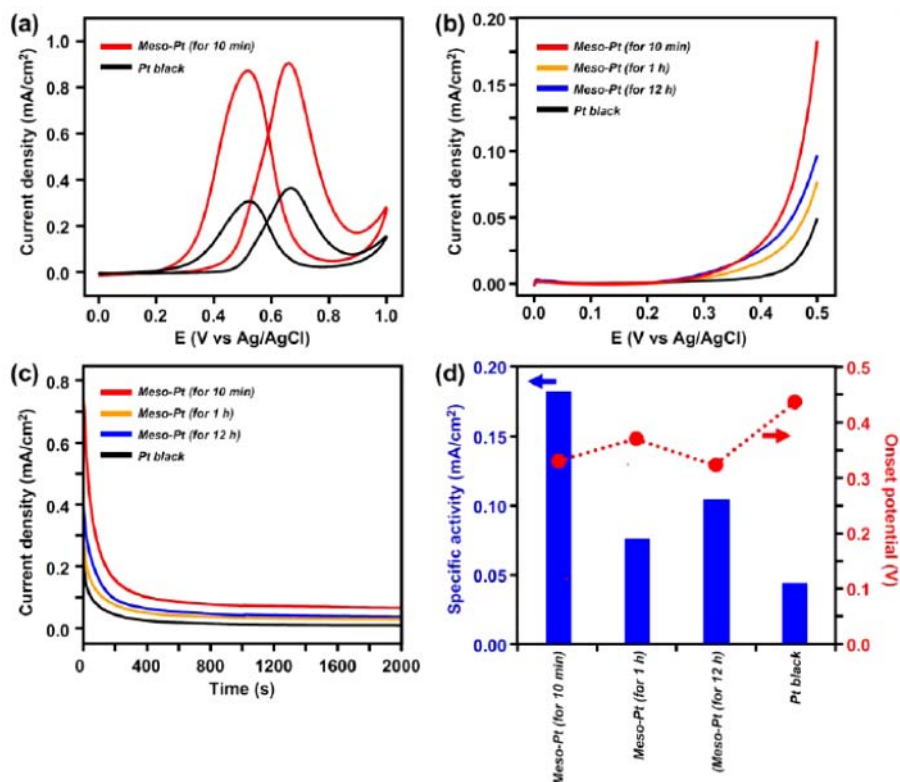


Figure 3.19 Demonstration of methanol oxidation activity of *meso*-Pt with different particle sizes in 0.5 M H₂SO₄ containing 0.5 M methanol. (a) Cyclic voltammograms for small-sized *meso*-Pt (deposited for 10 min) and Pt black (Scan rate: 50 mV·s⁻¹). The currents in Y-axis are normalized by electrochemically active surface areas (ECSAs, cm²) obtained from CV curves in 0.5 M H₂SO₄ solution. (b) Linear sweep voltammograms measured in 0.5 M H₂SO₄ containing 0.5 M methanol (Scan rate: 50 mV·s⁻¹). The onset potentials are defined as the potentials at 10 μA·cm⁻² in the linear sweep voltammograms. (c) Chronoamperometric curves at 0.6 V measured in 0.5 M H₂SO₄ containing 0.5 M methanol. (d) Summary on the specific activities at 0.5 V and the onset potentials for all the samples.

3.4. Conclusion

In conclusion, I have successfully synthesized monodispersed polyhedral- and olive-shaped mesoporous Pt nanoparticles with uniform particle sizes by using KIT-6

and SBA-15, respectively, as templates. The yield in the present work reached ~97%,

although very few Pt sources were lost in the centrifuging and washing processes. Almost all of the Pt sources were impregnated into the entire mesopore space and reduced inside the hard templates without Pt bulk deposition outside the mesopores. The present reduction process without high temperature and complex equipment is very simple and highly reproducible, which will be useful for large-scale production in the future. I hope that this method can provide a generic platform for the preparation of mesoporous metal NPs that can be used for other metal compositions. Well-defined morphology and uniformity in size (**Figure 3.9**) will become very important aspects for the future use of mesoporous metals in a wide range of applications such as electrodes, sensors, catalysis, and drug delivery.

References

- [1] T. Yanagisawa, T. Shimizu, K. Kuroda, and C. Kato, *Bull. Chem. Soc. Jpn.*, **63**, 988 (1990).
- [2] T. Yanagisawa, T. Shimizu, K. Kuroda, and C. Kato, *Bull. Chem. Soc. Jpn.*, **63**, 1535 (1990).
- [3] C. T. Kresge, M. E. Leonowicz, W. J. Roth, J. C. Vartuli, and J. S. Beck, *Nature*, **359**, 710 (1992).
- [4] Y. Wan, and D. Zhao, *Chem. Rev.*, **107**, 2821 (2007).
- [5] C. E. Fowler, D. Khushalani, B. Lebeau, and S. Mann, *Adv. Mater.*, **13**, 649 (2001).
- [6] T. W. Kim, P. W. Chung, and V. S. Y. Lin, *Chem. Mater.*, **22**, 5093 (2010).
- [7] V. Cauda, A. Schlossbauer, J. Kecht, A. Zurner, T. Bein, *J. Am. Chem. Soc.*, **131**, 11361 (2009).
- [8] C. Urata, H. Yamada, T. Wakabayashi, Y. Aoyama, S. Hirosawa, S. Arai, S. Takeoka, Y. Yamauchi, and K. Kuroda, *J. Am. Chem. Soc.*, **133**, 8102 (2011).
- [9] T. Suteewong, H. Sai, J. Lee, M. Bradbury, T. Hyeon, S. M. Gruner, and U. Wiesner, *J. Mater. Chem.*, **20**, 7807 (2010).
- [10] J. E. Lee, N. Lee, H. Kim, J. Kim, S. H. Choi, J. H. Kim, T. Kim, I. C. Song, S. P. Park, W. K. Moon, and T. Hyeon, *J. Am. Chem. Soc.*, **132**, 552 (2010).
- [11] J. Kim, J. E. Lee, J. Lee, J. H. Yu, B. C. Kim, K. An, Y. Hwang, C. H. Shin, J. G. Park, J. Kim, and T. Hyeon, *J. Am. Chem. Soc.*, **128**, 688 (2006).
- [12] Y. Fang, D. Gu, Y. Zou, Z. Wu, F. Li, R. Che, Y. Deng, B. Tu, and D. Zhao, *Angew. Chem., Int. Ed.*, **49**, 7987 (2010).
- [13] T. W. Kim, P. W. Chung, I. I. Slowing, M. Tsunoda, E. S. Yeung, and V. S. Y. Lin, *Nano Lett.*, **8**, 3724 (2008).
- [14] D. Gu, H. Bongard, Y. Meng, K. Miyasaka, O. Terasaki, F. Zhang, Y. Deng, Z. Wu, D. Feng, Y. Fang, B. Tu, F. Schuth, and D. Zhao, *Chem. Mater.*, **22**, 4828 (2010).
- [15] S. Giri, B. G. Trewyn, and V. S. Y. Lin, *Nanomedicine*, **2**, 99 (2007).

- [16] I. I. Slowing, C. W. Wu, J. L. Vivero-Escoto, and V. S. Y. Lin, *Small*, **5**, 57 (2009).
- [17] J. Lu, M. Liong, Z. Li, J. I. Zink, and F. Tamanoi, *Small*, **6**, 1794 (2010).
- [18] A. Saramat, M. Andersson, S. Hant, P. Thormahlen, M. Skoglundh, G. S. Attard, and A. E. C. Palmqvist, *Eur. Phys. J. D*, **43**, 209 (2007).
- [19] Y. Yamauchi, and K. Kuroda, *Chem. Asian J.*, **3**, 664 (2008).
- [20] A. Saramat, P. Thormahlen, M. Skoglundh, and G. S. Attard, A. E. C. Palmqvist, *J. Catal.*, **253**, 253 (2008).
- [21] G. S. Attard, C. G. Goltner, J. M. Corker, S. Henke, and R. H. Templer, *Angew. Chem., Int. Ed. Engl.*, **36**, 1315 (1997).
- [22] G. S. Attard, P. N. Bartlett, N. R. B. Coleman, J. M. Elliott, J. R. Owen, and J. H. Wang, *Science*, **278**, 838 (1997).
- [23] Y. Yamauchi, A. Takai, T. Nagaura, S. Inoue, and K. Kuroda, *J. Am. Chem. Soc.*, **130**, 5426 (2008).
- [24] Y. Yamauchi, A. Sugiyama, R. Morimoto, A. Takai, and K. Kuroda, *Angew. Chem., Int. Ed.*, **47**, 5371 (2008).
- [25] Y. Yamauchi, M. Komatsu, M. Fuziwara, Y. Nemoto, K. Sato, T. Yokoshima, H. Sukegawa, K. Inomata, and K. Kuroda, *Angew. Chem., Int. Ed.*, **48**, 7792 (2009).
- [26] F. Bender, R. K. Mankelaw, D. B. Hibbert, and J. J. Gooding, *Electroanalysis*, **18**, 1558 (2006).
- [27] J. Lee, S. Yoon, T. Hyeon, S. M. Oh, and K. B. Kim, *Chem. Commun.*, 2177 (1999).
- [28] R. Ryoo, S. H. Joo, and S. Jun, *J. Phys. Chem. B*, **103**, 7743 (1999).
- [29] J. Lee, S. Yoon, S. M. Oh, C. H. Shin, and T. Hyeon, *Adv. Mater.*, **12**, 359 (2000).
- [30] S. Yoon, J. W. Lee, T. Hyeon, and S. M. Oh, *J. Electrochem. Soc.*, **147**, 2507 (2000).
- [31] J. Lee, J. Kim, and T. Hyeon, *Chem. Commun.*, 1138 (2003).
- [32] A. H. Lu, and F. Schuth, *Adv. Mater.*, **18**, 1793 (2006).
- [33] H. Tuysuz, M. Comotti, and F. Schuth, *Chem. Commun.*, 4022 (2008).
- [34] A. Ruplecker, F. Kleitz, E. L. Salabas, and F. Schuth, *Chem. Mater.*, **19**, 485 (2007).
- [35] H. J. Shin, R. Ryoo, Z. Liu, and O. Terasaki, *J. Am. Chem. Soc.*, **123**, 1246 (2001).

- [36] Z. Liu, O. Terasaki, T. Ohsuna, K. Hiraga, H. J. Shin, and R. Ryoo, *ChemPhysChem*, **2**, 229 (2001).
- [37] Z. Liu, Y. Sakamoto, T. Ohsuna, K. Hiraga, O. Terasaki, C. H. Ko, H. J. Shin, and R. Ryoo, *Angew. Chem., Int. Ed.*, **39**, 3107 (2000).
- [38] Y. Doi, A. Takai, Y. Sakamoto, O. Terasaki, Y. Yamauchi, and K. Kuroda, *Chem. Commun.*, **46**, 6365 (2010).
- [39] X. J. Guo, C. M. Yang, P. H. Liu, M. H. Cheng, and K. J. Chao, *Cryst. Growth Des.* **5**, 33 (2005).
- [40] K. J. Chao, Y. P. Chang, Y. C. Chen, A. S. Lo, T. H. Phan, *J. Phys. Chem. B*, **110**, 1638 (2006).
- [41] T. W. Kim, F. Kleitz, B. Paul, and R. Ryoo, *J. Am. Chem. Soc.*, **127**, 7601 (2005).
- [42] X. Lu, M. Rycenga, S. E. Skrabalak, B. Wiley, and Y. Xia, *Annu. Rev. Phys. Chem.*, **60**, 167 (2009).

Chapter 4

Synthesis of Olive-Shaped Mesoporous Platinum Nanoparticles with Hard-Templating Method Using Mesoporous Silica (SBA-15)

4.1. Introduction

Ordered mesoporous materials with metal content are considered as promising candidates for the development of improved fuel cell electrodes and metallic nanocatalysts, which also may contribute to the miniaturization of optical and electronic materials [1-11]. Fukuoka *et al.* reported the selective formation of Pt nanowires and nanoparticles in mesoporous silica templates (FSM-16) [4-8]. Several metal nanowires and nanoparticles with different compositions have also been prepared. Especially, the Pt nanowires and nanoparticles in FSM-16 showed high catalytic activity and selectivity in the preferential oxidation (PROX) of CO. Yang *et al.* demonstrated the successful incorporation of Pd fine nanoparticles inside micropores by utilizing selective surface functionalization of the mesopores and micropores of mesoporous silica (SBA-15), which is highly promising for the preparation of novel nanocomposites for catalysis and other applications [11].

On the other hand, the synthesis of ordered mesoporous materials with metallic frameworks (*i.e.*, mesoporous metals) is not as easy because metals have high surface energies that favor low surface areas. Various types of ordered mesoporous materials have been synthesized under different conditions and extensively studied with regard to their mesostructural controllability, compositional diversity, and morphological flexibility [12]. An early route to prepare mesoporous metals involves dealloying of one metal from a bimetallic alloy, which is a main way for the preparation of Raney nickel [13]. During the dealloying process, more noble atoms are aggregated by a phase separation process (*i.e.*, spinodal decomposition) to form nanoporosity. The surface area gradually increases owing to the dealloying times. Erlebacher *et al.* successfully prepared nanoporous gold by dealloying an Ag-Au alloy [14]. Other nanoporous films with different compositions (*e.g.*, Pt and Pd) also have been reported up to date [15-17].

However, fine pore-size controls are impossible. In contrast, surfactant self-assembly provides a satisfactory way for preparing highly ordered mesoporous structures. The lyotropic liquid crystal (LLC) method, which relies on highly concentrated surfactants or block copolymers, as a typical soft templating way, has been used to synthesize highly ordered mesoporous metals [18-22]. Through chemical or

electrochemical reduction, ordered mesoporous metal powders or films can be synthesized easily. However, the ordered arrangement of the rod-like self-assemblies in the LLCs is sometimes seriously distorted during the metal deposition process, in which the long-range ordering of the mesostructures is lost in the final product [23]. Recently, Wiesner *et al.* demonstrated that the self-assembly of block copolymers with ligand-stabilized platinum nanoparticles provided access to ordered arranged mesostructures [24, 25]. Remita *et al.* also reported that giant direct hexagonal mesophases composed of a quaternary system (water, surfactant, cosurfactant, and oil) can be used as a soft template to synthesize nanostructured Pt and Pd [26, 27].

In comparison with the soft-templating method, the hard-templating method seems to be an attractive alternative that has been used as a traditional synthetic process for mesoporous carbon materials [28-36]. Although the hard-templating method requires multiple steps, fine control of mesostructures becomes possible by changing the original mesostructures of the used templates. Mesoporous silica with a robust framework and high thermal stability has been used as a common hard template to synthesize a metal replica [37-42]. Up to date, various Pt nanostructures, such as 1D nanowires and 3D nanowire networks, have been prepared by using various types of mesoporous silica as hard templates, including SBA-15 (*p6mm*) with ordered two-dimensional hexagonal channel structures.

Despite these recent advances in soft- and hard-templates, the obtained morphologies of mesoporous metals have been very limited to only powders with irregular morphology or films on a conductive substrate. In addition, considering various catalysis reaction processes, catalysts or adsorbents must often be packed in a fixed-bed reactor or a column. Therefore, it is very important to establish a simple method of producing mesoporous metal particles with a uniform particle size. Although several mesostructured Pt samples with various mesostructures and compositions have been reported using mesoporous silica, their particle size distribution was very broad. The lack of control over the particles sizes and morphologies is a serious problem for further developments of mesoporous metals.

In this chapter, I further applied this concept to a mesoporous silica (SBA-15) system with a 2D hexagonal mesostructure. I successfully prepared olive-shaped uniform mesoporous Pt nanoparticles (MPNs). Furthermore, the average particle size

could be controlled in the range of 150 nm to 230 nm by changing the Pt deposition time. Our reduction process, in which the AA solution as a reducing agent is dropped into mesoporous silica powders with Pt species, is extremely simple and highly reproducible without high temperature/pressure or any other complex conditions. Small MPNs exhibited superior electrocatalytic activity in the methanol oxidation reaction to our previous MPNs prepared from KIT-6 [43] and commercially available Pt black. Methanol molecules as guest species can be easier to reach the entire Pt surface on smaller MPNs.

4.2. Experimental Process

4.2.1. Synthesis of mesoporous silica SBA-15

In a typical synthesis, 4.0 g of Pluronic P123 (PEO₂₀-PPO₇₀-PEO₂₀, Aldrich, 99%) was dissolved in 86.0 g of distilled water and 24.6 g of conc. HCl (35 wt %) under vigorous stirring. After complete dissolution, 8.5 g of TEOS (Acros, Purity 98%) was added. The mixture was further stirred at 35 °C for 24 h, followed by a hydrothermal treatment at 100 °C for 24 h under static conditions in a closed polypropylene bottle. The solid product was dried at 80 °C. The surfactant was removed by extraction with water and ethanol followed by calcination at 550 °C for 6 h. SEM image of the obtained SBA-15 was shown in **Figure 4.1**.

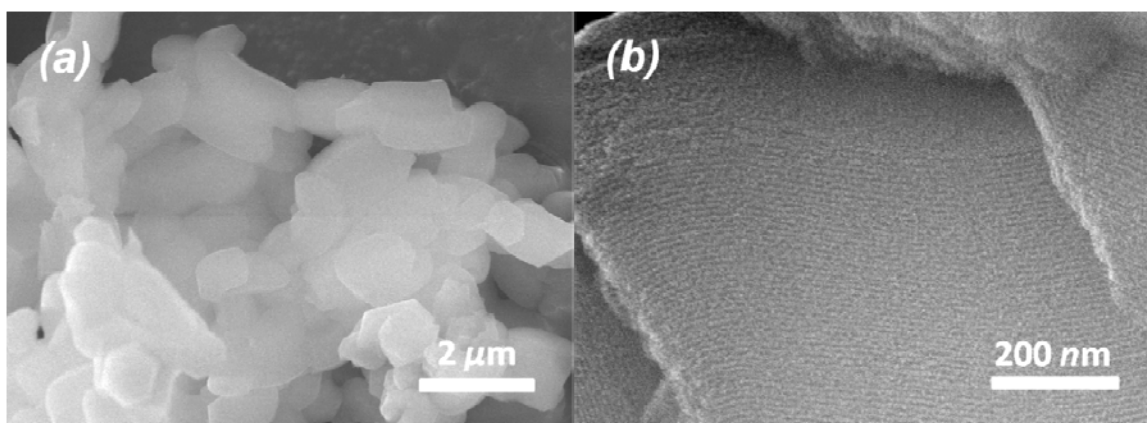


Figure 4.1 (a) Low magnification and (b) high magnification SEM images of the original mesoporous silica SBA-15.

4.2.2. Preparation of mesoporous Pt nanoparticles

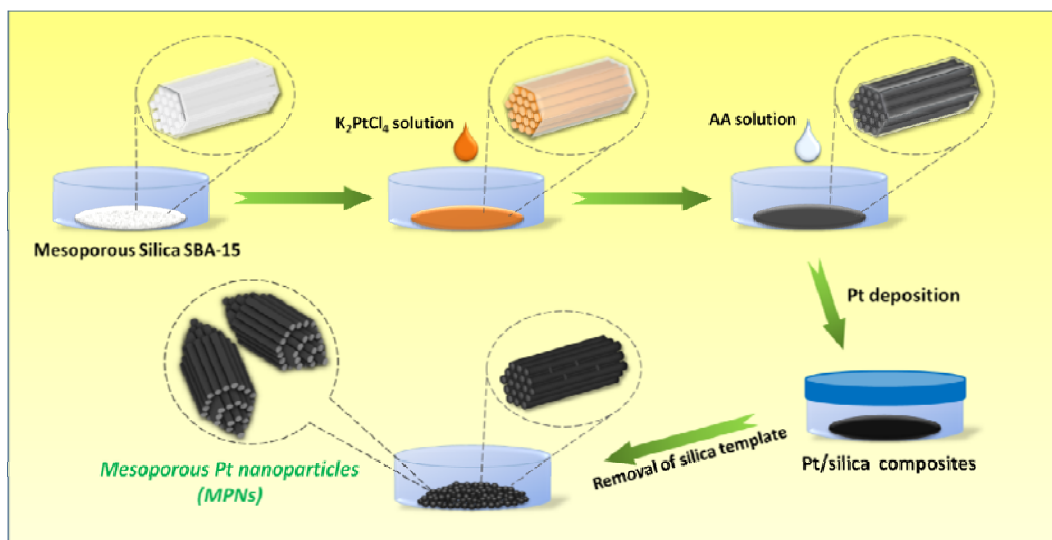
In the Pt deposition process, 2.0 g of a 24.0 wt% K₂PtCl₄ aqueous solution was dropped on 0.6 g of SBA-15 power. The composite was then dried under a reduced vacuum condition at room temperature. After complete drying, an orange-colored powder was obtained. Then, a small amount (2.0 ml) of a 1.0 M ascorbic acid solution was dropped onto the powder. The Pt deposition was carried out in a closed vessel for

30 min, 1 h, and 12 h. Then, the color changed gradually to black. After the Pt deposition, the samples were washed with a 10% hydrofluoric acid solution to remove the silica templates. The black powder was centrifuged and washed with distilled water and then dried at room temperature.

4.2.3. Characterization

Low-angle XRD patterns were obtained by using a Rigaku NANO-Viewer with monochromated Cu K α radiation. The morphology of powder samples was observed using Hitachi S-4800 field emission scanning electron microscopy (FE-SEM). Transmission electron microscopic (TEM) images were taken by JEOL JEM 2010 (200 kV) to demonstrate the formation of periodic mesostructures inside particles. Selected-area electron diffraction (ED) was used to determine the atomic crystallinity of the materials. N₂ adsorption-desorption isotherms were measured using a Quantachrome Autosorb-1 at liquid nitrogen temperature of 77 K with prior degassing at 55 °C for 12 h. The specific surface areas and average pore sizes were calculated by the BET method and the BJH method using adsorption branches, respectively.

4.3. Results and Discussion



Scheme 4.1 Schematic representation of synthetic procedure for preparation of olive-shaped mesoporous Pt nanoparticles (MPNs).

Scheme 4.1 illustrates the synthetic procedure for the preparation of olive-shaped mesoporous Pt nanoparticles (MPNs) from mesoporous silica (SBA-15). After addition of ascorbic acid (AA) solution, the color of the Pt/silica composite gradually changed from orange to gray. The color of the composites gradually changed to dark black, indicating that the Pt species was deposited. After Pt deposition followed by removal of silica templates, highly ordered olive-shaped MPNs were successfully obtained. **Figure 4.2** shows the morphology of the MPNs deposited for 12 hours using ascorbic acid (AA). From the low-magnification SEM image (**Figure 4.2a**), MPNs were isolated from each other, and the particle sizes were relatively uniform, with average length of 230 nm. More interestingly, all the MPNs showed an olive-shaped morphology (**Figure 4.2b**), although some particles appeared to have a different morphology because of the different angle of observation. The obtained samples contained very few impurities other than the ordered mesoporous networks. Most of the particles possessed well-ordered mesostructures, indicating that the Pt species was successfully loaded into the mesopore space by capillary force and then reduced inside

the mesopore without Pt deposition on the external surface of mesoporous silica particles. From high-magnification SEM images (**Figure 4.2b**), periodically arranged Pt nanowires were observed, which was a negative replica of the 2D hexagonally ordered mesoporous silica (SBA-15). The honeycomb arrangement of the Pt nanowires was clearly confirmed, as shown in the inset image in **Figure 4.2b**.

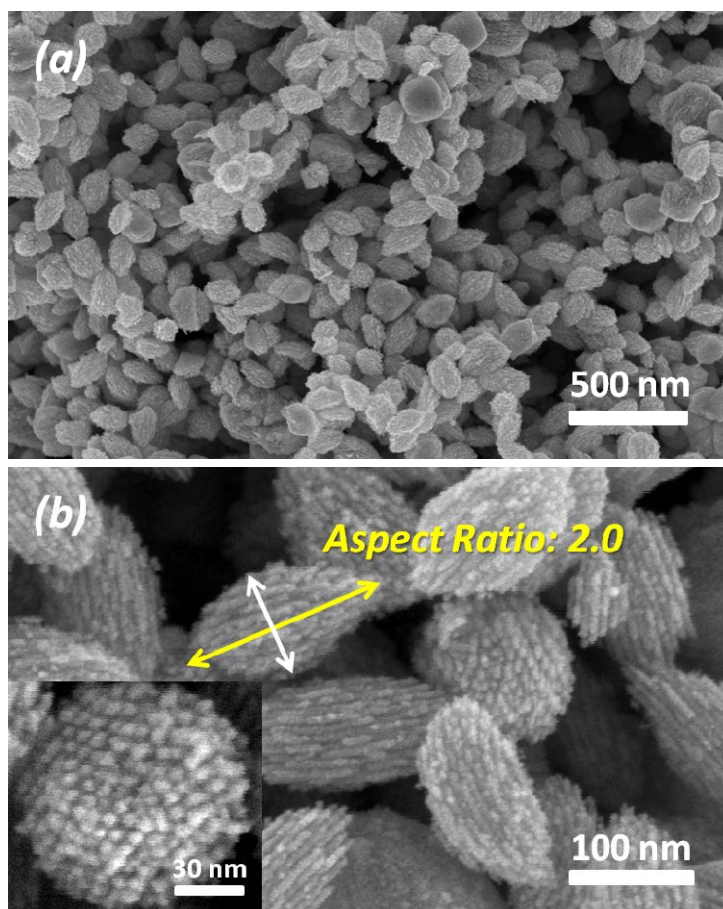


Figure 4.2 (a) Low magnified and (b) high magnified SEM images of the obtained MPNs prepared from mesoporous silica (SBA-15) with deposition time for 12 hours. Honeycomb arrangements of the Pt nanowires are indicated as an inset image.

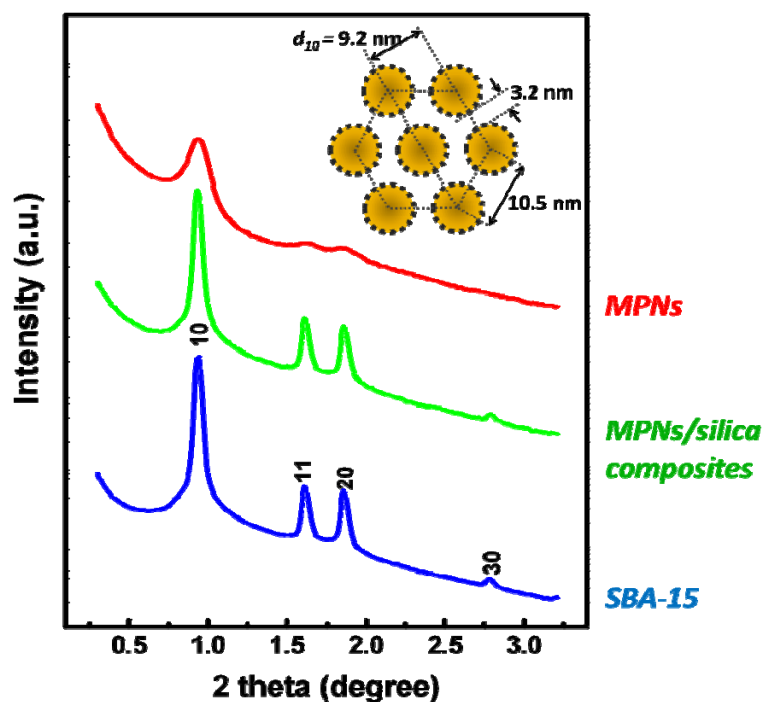


Figure 4.3 Low angle profiles of the original mesoporous silica, MPNs/silica composites (before the silica removal), and MPNs (after the silica removal), respectively.

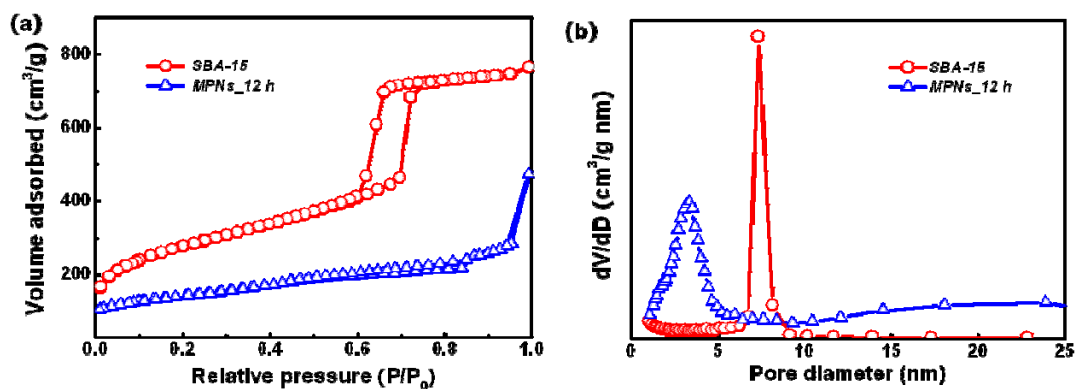


Figure 4.4 (a) N_2 adsorption-desorption isotherms and (b) pore size distribution curves of the original mesoporous silica SBA-15 and the obtained MPNs. BET surface areas are calculated to be $943.0 \text{ m}^2 \cdot \text{g}^{-1}$ for the original mesoporous silica SBA-15, and $37.0 \text{ m}^2 \cdot \text{g}^{-1}$ for MPNs.

Low-angle XRD profiles for MPNs, MPNs/silica composites, and SBA-15 show well-resolved peaks (**Figure 4.3**). All the peaks showed three distinct peaks assignable to the (10), (11), and (20) planes of a highly ordered 2D hexagonal symmetry with d_{10} spacing of 9.2 nm. After silica removal, MPNs still maintained intense peaks which had exactly the same profile as that of the original SBA-15 mesoporous silica. This is evidence that the Pt replicated from SBA-15 well retained the original symmetry. The N_2 adsorption-desorption isotherms for the original mesoporous silica (SBA-15) and MPNs (deposited for 12 hours) are shown in **Figure 4.4**. The N_2 adsorption-desorption isotherm curves showed a typical isotherm of mesoporous materials. Using the BET method, the surface areas were calculated to be $943 \text{ m}^2\cdot\text{g}^{-1}$ (for SBA-15) and $37.0 \text{ m}^2\cdot\text{g}^{-1}$ (for MPNs). The average pore size distributions were evaluated with the BJH method. The average sizes were around 7.3 nm (for SBA-15) and 3.2 nm (for MPNs). The observed pore (around 3.2 nm) indicates a void space between the one-dimensional Pt nanowires. This value is in good agreement with the wall thickness of the original SBA-15 (inset image in **Figure 4.3**). In comparison with commercially available Pt black (with about $20 \text{ m}^2\cdot\text{g}^{-1}$ surface area), our MPNs possessed two times higher surface area and much narrower pore size distribution, which will provide a favorable condition for electrochemical applications.

It is noteworthy that each Pt nanowire in one MPN was oriented parallel in the same direction, which is quite an interesting mesostructural feature (**Figure 4.2b**). Our recent work, in which we prepared MPNs from mesoporous silica (KIT-6), explained the reason that each particle was a “single mesoporous crystal” [43]. When the Pt/mesoporous silica composites after the Pt deposition were investigated by TEM, the deposited Pt particles were distributed over the entire silica matrix and isolated from each other. Notably, the Pt particles were deposited within the same single mesostructural domain of the original KIT-6. The domain sizes of mesoporous crystal with the same orientation in the KIT-6 template were sub-micrometer scale, which was much larger than the particle sizes of the deposited Pt particles. Therefore, it was very reasonable that the obtained Pt particle replicated by KIT-6 showed single mesoporous crystal. The same situation occurred in this study. The original SBA-15 as a hard template showed rod-like shapes with 200 nm width (**Figure 4.1a**). A high-magnified image (**Figure 4.1b**) showed that tubular one-dimensional mesochannels were running

parallel along the long axis of the rods. The domain sizes with the same mesochannel orientation were much larger than the deposited Pt sizes shown in **Figure 4.2**.

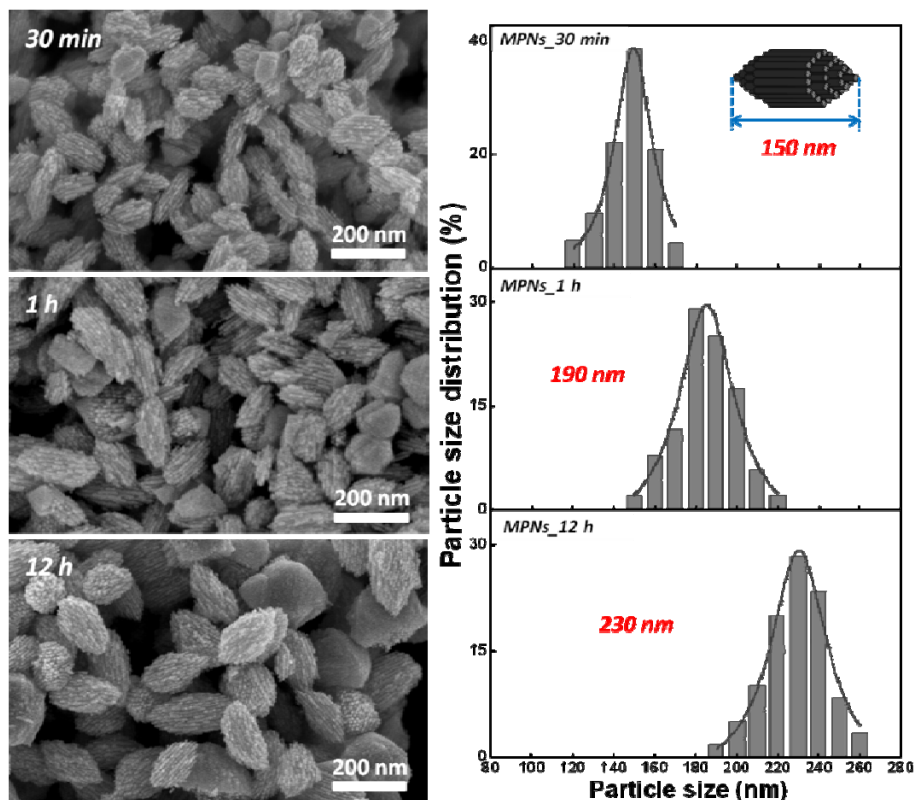


Figure 4.5 High-magnified SEM images of the MPNs prepared by different Pt deposition time (for (a) 30 min, (b) 1 h, and (c) 12 h) and the corresponding particle size distributions.

The particle size can be easily controlled by changing the Pt deposition time. In the experiment, several types of samples with different Pt deposition time (30 min, 1 hour, and 12 hours) were prepared. **Figure 4.5** shows the SEM images of all the three samples and their corresponding particle size distributions. When the deposition time was only 30 min, all the deposited Pt particles already had an olive-like shape with a narrow particle size distribution (the average length of the particles was 150 nm). From the high-magnified SEM images, a negative replica of the 2D hexagonally ordered mesoporous structure could be clearly observed. As the deposition time increased, the average particle sizes obviously increased. With an increase of the deposition period to 1 hour, the average length was increased up to 190 nm. After the complete reduction of

the Pt sources for 12 hours, the average particle size grew uniformly and reached 230 nm, and the negative 2D hexagonal structure was observed more clearly, which also was verified by low-angle XRD patterns for MPNs with different particle sizes (**Figure 4.6**). As the deposition time increased, the (11) and (20) peaks became clear, showing long range of mesostructural ordering. The peak positions for three samples prepared by different deposition time did not change at all. The wide-angle XRD patterns showed a typical *fcc* (face-centered-cubic) crystal structure for all MPNs with different particle sizes (**Figure 4.7**). With the increase in the particle sizes, the peak intensities in the wide-angle XRD patterns also increased. The FWHM (the peak width at half height) of the (111) peaks gradually decreased from 0.741 (for 30 min) to 0.732 (for 1 hour) and further to 0.691 (for 12 hours), indicating the enlargement of Pt *fcc* crystal domains with the increase of the particle sizes.

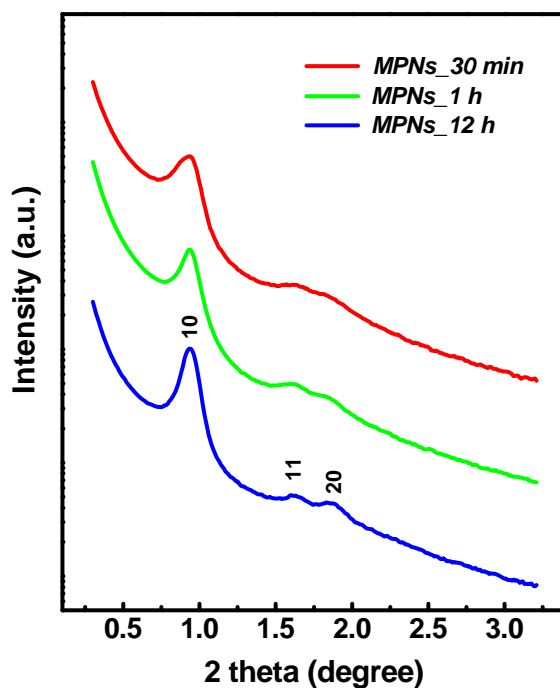


Figure 4.6 Low-angle XRD profiles of the MPNs prepared by different Pt deposition time (30 min, 1 hour, and 12 hour, respectively).

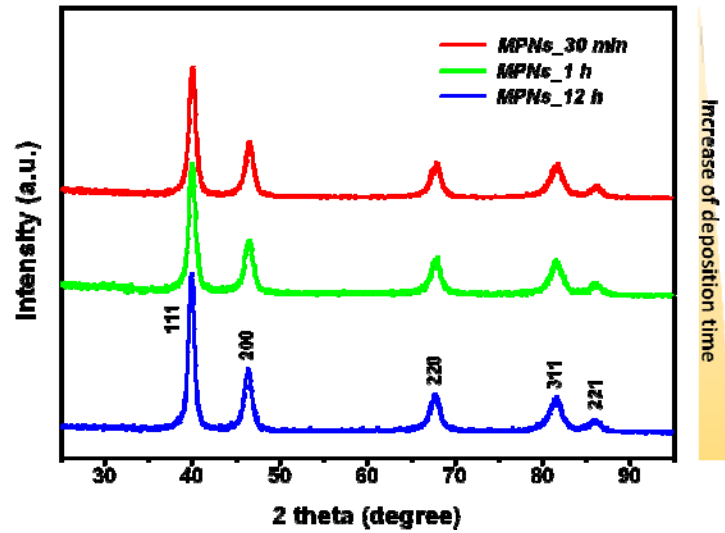


Figure 4.7 Wide-angle XRD patterns of MPNs prepared by different Pt deposition time (30 min, 1 hour, and 12 hours, respectively). With the increase of the deposition time, the peak intensities are gradually increased. The values of full widths at half maximum (FWHM) are 0.741 (for 30 min), 0.732 (for 1 hour) and 0.691 (for 12 hours), respectively.

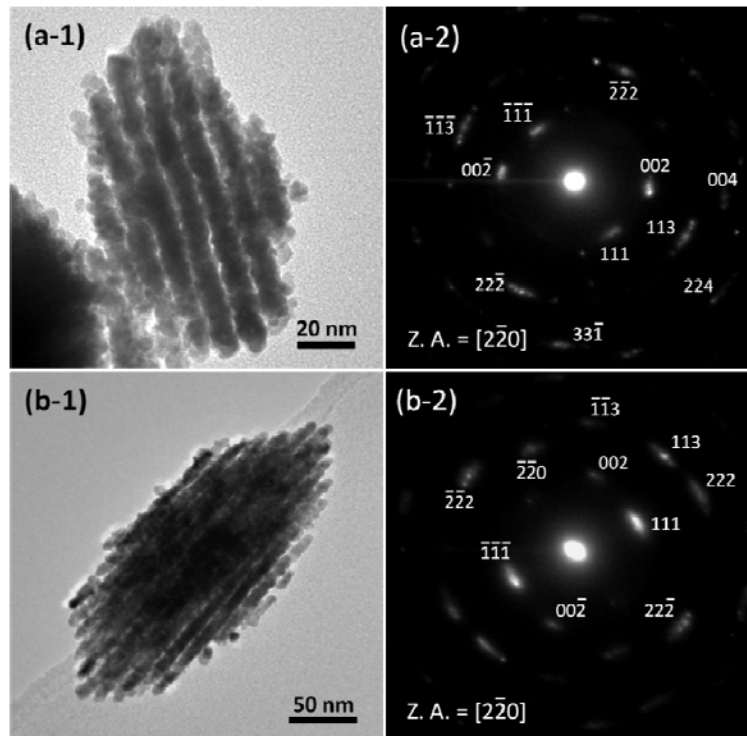
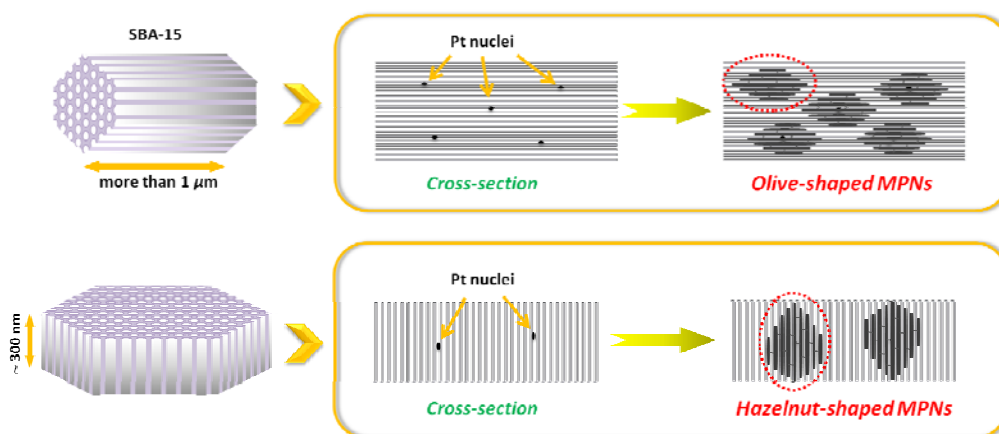


Figure 4.8 TEM images of the MPNs by different Pt deposition time ((a) 1 hour and (b) 12 hour) and their corresponding ED patterns.

A TEM observation was used to study the microstructure in MPNs. TEM images of MPNs are shown in **Figure 4.8** with two different particle sizes and their corresponding electron diffraction (ED) patterns. Small MPNs (prepared by Pt deposition for 30 min) are shown in **Figure 4.8a-1**. A highly ordered mesostructure was well developed. Notably, the ED patterns taken from one particle showed that the Pt within the framework possessed a single-crystalline state of the Pt *fcc* structure (**Figure 4.8a-2**). The same situation was confirmed in large MPNs (prepared for 12 h) (**Figure 4.8b**).



Scheme 4.2 Schematic view of growing process of MPNs in two types of SBA-15.

At the beginning stage of the Pt deposition, the reducing agent (AA) reduced the Pt species embedded inside the mesochannels of the silica template (SBA-15), and some Pt nuclei were then formed (**Scheme 4.2**). This is a nucleation process that should be located at the center of each Pt particle. Next, the Pt grain growth from the initial nuclei increasingly proceeded, forming larger particles with coherent retention of the Pt atomic crystallinity over the full region of each particle (**Figure 4.8**).

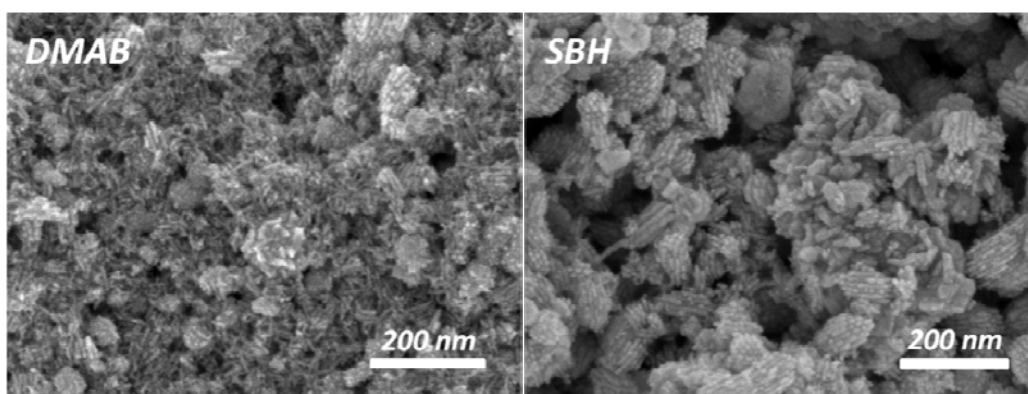


Figure 4.9 SEM images of Pt deposited by using DMAB and SBH as reducing agents, respectively.

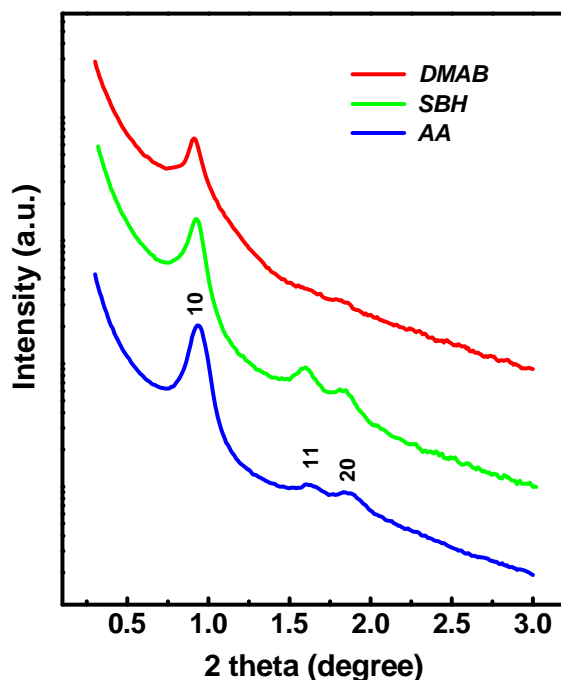


Figure 4.10 Low-angle XRD profiles of Pt deposited by using DMAB, SBH, and AA as reducing agents, respectively.

To realize the formation of uniform MPNs, the strength of the reducing agent plays a significant role. For comparison, two different kinds of reducing agents, dimethylaminoborane (DMAB) and sodium borohydride (SBH), were utilized instead of AA. With a very severe reaction and large volumes of gas released, the Pt deposition occurred. In both cases, the deposited Pt showed an irregular morphology (**Figure 4.9**). Some particles had no ordered mesoporous structures, because some Pt species were

deposited on the outer surface of the mesoporous silica particles. A similar situation was observed in our previous work [43]. The peak intensities of the SAXS patterns were also much smaller than those of the MPNs obtained using AA as a reducing agent (**Figure 4.10**), which was consistent with the SEM images (**Figure 4.9**). These results proved that the use of AA is vital for the formation of highly ordered MPNs with uniform sizes. The deposition rate is determined by the strength of the reducing agent. Compared to AA, DMAB and SBH are very strong reducing agents and can reduce Pt sources very rapidly. Especially for SBH, at the moment of addition of SBH solution, orange-colored powder was immediately changed to black. This was totally different with the AA system which required a few minutes for changing to dark and then black. Therefore, we assume that DMAB and SBH molecules cannot enter the mesoporous particles and reduce the Pt species inside them. In contrast, with the use of AA as a reducing agent, it can provide sufficient time to reach the position of Pt sources located inside the mesoporous of silica.

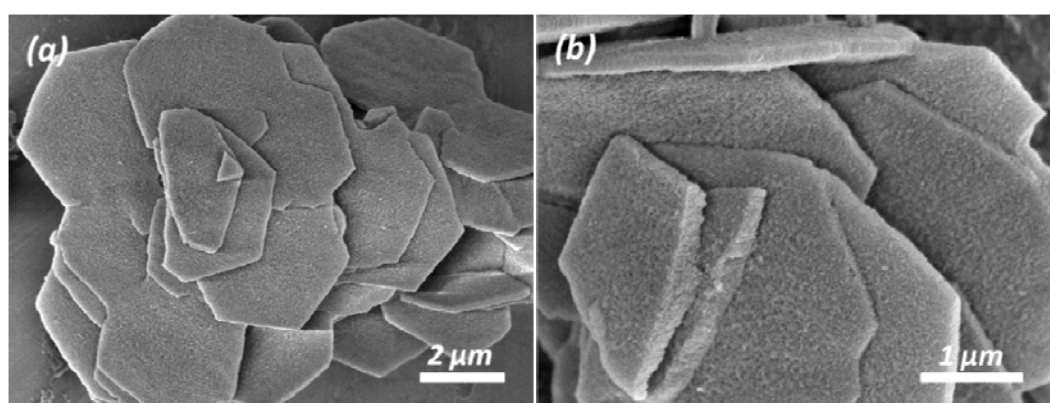


Figure 4.11 SEM images of platelet-shaped mesoporous silica.

To further understand the formation mechanism, I used another type of mesoporous silica (**Figure 4.11**). Park *et al.* reported SBA-15-type mesoporous silica having a unique hexagonal platelet morphology with short mesochannels running parallel to the full thickness of the plate using the co-condensation method of aminopropyltriethoxysilane (APTES) and sodium metasilicate as a silica source in the presence of a Pluronic P123 triblock copolymer as a structure-directing agent [44]. Here,

I used platelet-shaped mesoporous silica as a hard template (**Scheme 4.2**). The short mesochannels in the hexagonal platelets can give higher accessibility of AA from the outside than general mesoporous silica SBA-15. Therefore, we can expect the formation of a different-shaped morphology in MPNs. After silica removal, the obtained MPNs showed an interesting hazelnut-shaped morphology in the above platelet SBA-15 system (**Figure 4.12**). From the high-resolution SEM images (**Figure 4.12c, d**), a highly ordered 2D hexagonal mesostructure can be observed, which was confirmed by low-angle XRD measurement (**Figure 4.13**). The morphologies of the obtained MPNs are a little different from those of MPNs prepared from SBA-15.

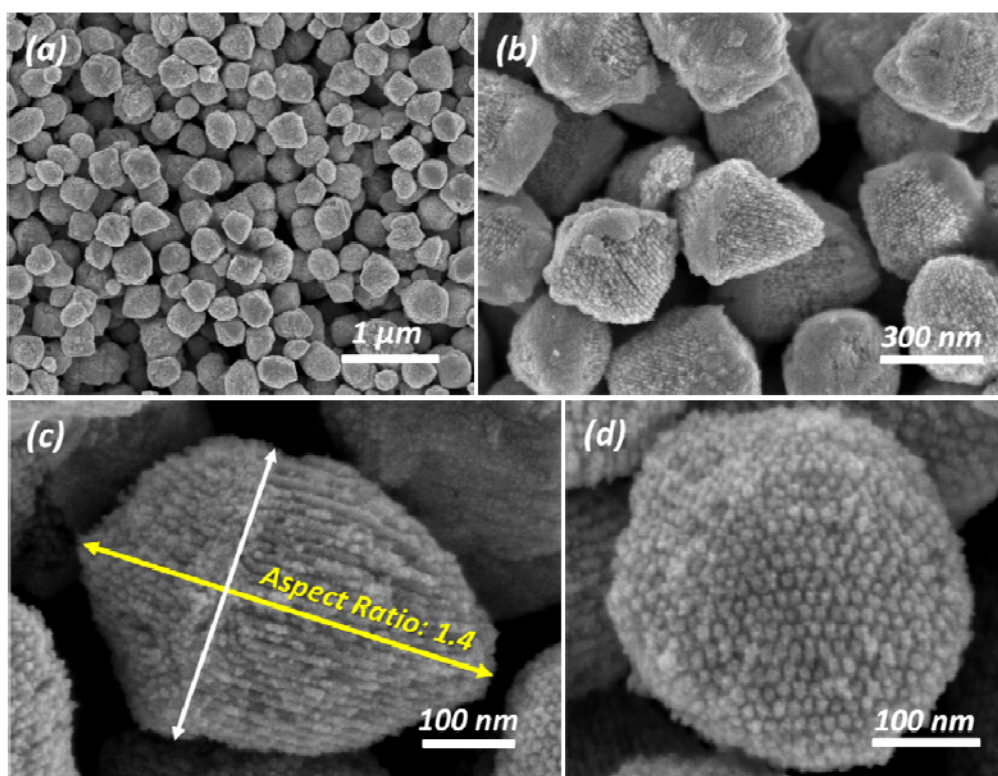


Figure 4.12 (a, b) Low-magnified and (c, d) high-magnified SEM images of the MPN prepared with platelet-shaped mesoporous silica.

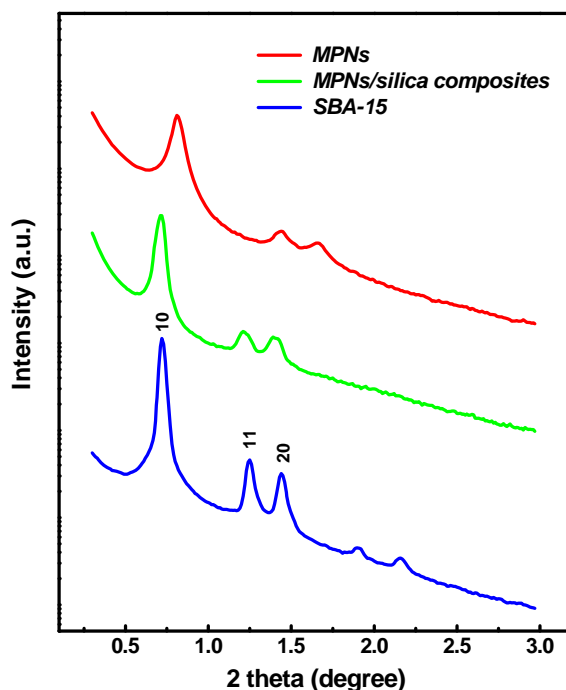


Figure 4.13 Low-angle XRD profiles of the original platelet-shaped mesoporous silica, MPNs/silica composites (before the silica removal), and MPNs (after the silica removal), respectively.

In previous work, using the same deposition method, I successfully prepared polyhedron-shaped MPNs from 3D bicontinuous mesoporous silica KIT-6 [43]. After Pt nuclei were formed in the early stage of the reaction with a slow reduction rate, Pt particles began to grow along the gyroid mesochannels. In this case, the obtained nanoparticles tended to be spherical. On the other hand, for SBA-15 with a 2D hexagonal mesostructure, the resistances of the particle growth are quite different between the parallel and the perpendicular directions to mesochannels. Pore walls in SBA-15 have many micropores connecting the straight mesochannels. Inside such micropores, the Pt deposition rate should be decreased due to insufficient supply of the Pt species. As a result, olive-shaped MPNs were formed, in which the length (in the direction parallel to the Pt nanowires) was larger than the width (in the perpendicular direction to Pt nanowires) (**Figures 4.2** and **4.5**). From **Figures 4.2** and **4.5**, the aspect ratios were roughly measured to be around 2. When platelet-shaped mesoporous silica

was used as a hard template, the aspect ratios were slightly reduced to around 1.0-1.5, showing hazelnut-shaped Pt nanoparticles (**Figure 4.12c**). This is because the short mesochannels in the platelet-shaped mesoporous silica can uniformly provide an AA-reducing agent from the outside to the nucleus sites without resulting in a serious bias for the diffusion (**Scheme 4.2**).

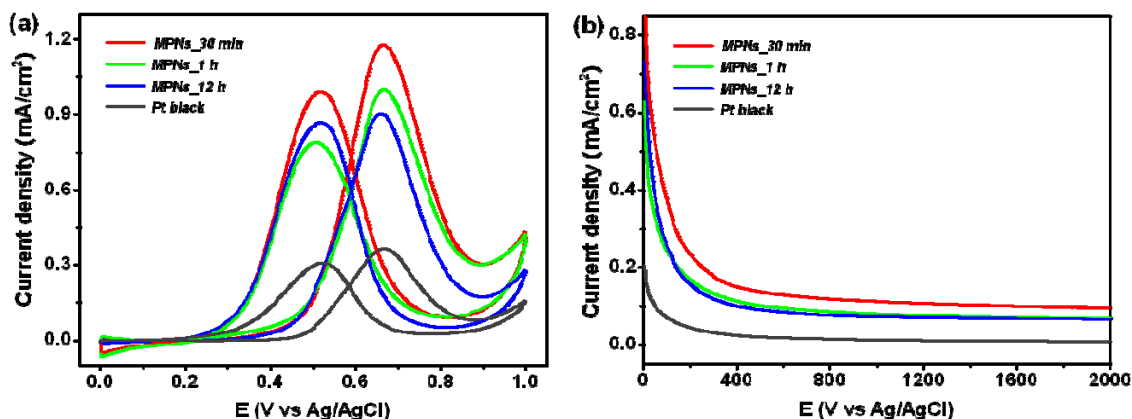


Figure 4.14 Demonstration of methanol oxidation activity of MPNs with different particle sizes in 0.5 M H₂SO₄ containing 0.5 M methanol. (a) Cyclic voltammograms for MPNs samples prepared from SBA-15 with different depositing time, which were compared with commercial Pt black. The scan rate is 50 mV·s⁻¹. The current densities at 0.6 V are measured to be 0.825 (mA·cm⁻²) (MSNs for 30 min), 0.661 (mA·cm⁻²) (MSNs for 1 h), 0.577 (mA·cm⁻²) (MSNs for 12 h), and 0.255 (mA·cm⁻²) (for Pt black), respectively. (c) Chronoamperometric curves of all the samples at 0.6 V.

In order to investigate its potential as a catalytic electrode, I measured the methanol electrochemical oxidation reaction on the obtained MPNs. The electrocatalytic performance recorded in an aqueous solution containing methanol is displayed in **Figure 4.14**. The catalytic activities of all the MPNs were obviously enhanced, which are two or three times higher than the activity of Pt black. The catalytic activity of Pt nanoparticles is highly shape-dependent [45, 46]. As the particle size decreased, the catalytic activity of MPNs increased. Of all three MPN samples prepared from SBA-15, the MPNs (prepared for 30 min) with the smallest particle size showed a remarkably large current density and the highest catalytic activity for electrocatalytic methanol oxidation. In comparison with commercial Pt black, the onset potentials of MPNs were

clearly negatively shifted (**Figure 4.14a**). Chronoamperometric curves recorded at 0.6 V proved that all the MPN samples exhibited enhanced durability compared with Pt black (**Figure 4.14b**). From these results, small MPNs had the best performance.

The above results revealed that use of small-sized MPNs allowed the methanol molecules to access all the inner mesoporous more easily without serious diffusion resistance. Interestingly, MPNs replicated from SBA-15 (deposited for 30 min and 1 hour, except for 12 h) exhibited higher catalytic activities than small MPNs (*i.e.*, inverse double gyroid mesostructure) replicated from KIT-6 ($0.659 \text{ mA}\cdot\text{cm}^{-2}$ at 0.6 V) [43]. Considering the electrochemical applications, the nanoporous conformation, which determines accessibility of guest molecules from the outside into the inner part of the pore space, is highly important. 1D straight mesospace created among the Pt nanowires is considered to be a highly open porous host with easy and direct access for guest species, compared to 3D porous network replicated from KIT-6 in which the Pt nanowires are curved and spatially branched. Such difference of the Pt nanostructures would lead to the higher methanol oxidation catalytic activity of MPNs prepared from SBA-15.

4.4. Conclusion

Highly ordered olive-shaped mesoporous Pt nanoparticles (MPNs) was successfully synthesized by using SBA-15 as template *via* ascorbic acid as a reducing agent. The obtained MPNs had a narrow particle size distribution and their sizes could be controlled from 150 nm to 230 nm by changing Pt deposition time. The use of ascorbic acid provides a slow reaction rate and sufficient reaction time, which enables ascorbic acid molecules to effectively penetrate into the mesochannels of silica template. The small-sized MPNs achieved much higher catalytic activity than commercial Pt black for the methanol oxidation reaction. The present facile synthesis showed high controllability in the particle size without collapse of well-ordered mesostructure, which can be scaled up for industrial mass production.

References

- [1] A. Haryono, and W. H. Binder, *Small*, **2**, 600 (2006).
- [2] J. M. Campelo, D. Luna, R. Luque, J. M. Marinas, and A. A. Romero, *ChemSusChem*, **2**, 18 (2009).
- [3] R. J. White, R. Luque, V. L. Budarin, J. H. Clark, and D. J. Macquarrie, *Chem. Soc. Rev.*, **38**, 481 (2009).
- [4] M. Sasaki, M. Osada, N. Higashimoto, T. Yamamoto, A. Fukuoka, and M. Ichikawa, *J. Mol. Catal. A-Chem.*, **141**, 223 (1999).
- [5] Y. Sakamoto, A. Fukuoka, T. Higuchi, N. Shimomura, S. Inagaki, and M. Ichikawa, *J. Phys. Chem. B*, **108**, 853 (2004).
- [6] A. Fukuoka, and M. Ichikawa, *Top. Catal.*, **40**, 103 (2006).
- [7] A. Fukuoka, J. I. Kimura, T. Oshio, Y. Sakamoto, and M. Ichikawa, *J. Am. Chem. Soc.*, **129**, 10120 (2007).
- [8] A. Fukuoka, Y. Sakamoto, T. Higuchi, N. Shimomura, and M. Ichikawa, *J. Porous. Mat.*, **13**, 231 (2006).
- [9] C. M. Yang, M. Kalwei, F. Schüth, and K. Chao, *J. Appl. Catal. A-Gen.*, **254**, 289 (2003).
- [10] C. M. Yang, P. H. Liu, Y. F. Ho, C. Y. Chiu, and K. Chao, *J. Chem. Mater.*, **15**, 275 (2003).
- [11] C. M. Yang, H. A. Lin, B. Zibrowius, B. Spliethoff, F. Schüth, S. C. Liou, M. W. Chu, and C. H. Chen, *Chem. Mater.*, **19**, 3205 (2007).
- [12] Y. Wan, and D. Zhao, *Chem. Rev.*, **107**, 2821 (2007).
- [13] M. Raney, *U.S. Patent 1*, **628**, 190 (1927).
- [14] J. Erlebacher, M. J. Aziz, A. Karma, N. Dimitrov, and K. Sieradzki, *Nature*, **410**, 450 (2001).
- [15] S. Tominaka, M. Shigeto, H. Nishizeko, and T. Osaka, *Chem. Commun.*, **46**, 8989 (2001).
- [16] S. Tominaka, *J. Mater. Chem.*, **21**, 9725 (2011).

- [17] S. Tominaka, T. Hayashi, Y. Nakamura, and T. Osaka, *J. Mater. Chem.*, **20**, 7175 (2010).
- [18] G. S. Attard, C. G. Goltner, J. M. Corker, S. Henke, and R. H. Templer, *Angew. Chem., Int. Ed. Engl.*, **36**, 1315 (1997).
- [19] G. S. Attard, P. N. Bartlett, N. R. B. Coleman, J. M. Elliott, J. R. Owen, and J. H. Wang, *Science*, **278**, 838 (1997).
- [20] Y. Yamauchi, A. Takai, T. Nagaura, S. Inoue, and K. Kuroda, *J. Am. Chem. Soc.*, **130**, 5426 (2008).
- [21] Y. Yamauchi, A. Sugiyama, R. Morimoto, A. Takai, and K. Kuroda, *Angew. Chem., Int. Ed.*, **47**, 5371 (2008).
- [22] Y. Yamauchi, M. Komatsu, M. Fuziwara, Y. Nemoto, K. Sato, T. Yokoshima, H. Sukegawa, K. Inomata, and K. Kuroda, *Angew. Chem., Int. Ed.*, **48**, 7792 (2009).
- [23] F. Bender, R. K. Mankelaw, D. B. Hibbert, and J. Gooding, *J. Electroanalysis*, **18**, 1558 (2006).
- [24] S. C. Warren, L. C. Messina, L. S. Slaughter, M. Kamperman, Q. Zhou, S. M. Gruner, F. J. DiSalvo, and U. Wiesner, *Science*, **320**, 1748 (2008).
- [25] H. Arora, Z. Li, H. Sai, M. Kamperman, S. C. Warren, and U. Wiesner, *Macromol. Rapid Commun.*, **31**, 1960 (2010).
- [26] F. Ksar, G. Surendran, L. Ramos, B. Keita, L. Nadjo, E. Prouzet, P. Beaunier, A. Hagege, F. Audonnet, and H. Remita, *Chem. Mater.*, **21**, 1612 (2009).
- [27] G. Surendran, L. Ramos, B. Pansu, E. Prouzet, P. Beaunier, F. Audonnet, and H. Remita, *Chem. Mater.*, **19**, 5045 (2007).
- [28] J. Lee, S. Yoon, T. Hyeon, S. M. Oh, and K. B. Kim, *Chem. Commun.*, 2177 (1999).
- [29] J. Lee, S. Yoon, S. M. Oh, C. H. Shin, and T. Hyeon, *Adv. Mater.*, **12**, 359 (2000).
- [30] S. Yoon, J. Lee, T. Hyeon, and S. M. Oh, *J. Electrochem. Soc.*, **147**, 2507 (2000).
- [31] J. Lee, J. Kim, and T. Hyeon, *Chem. Commun.*, 1138 (2003).
- [32] R. Ryoo, S. H. Joo, and S. Jun, *J. Phys. Chem. B*, **103**, 7743 (1999).
- [33] S. Jun, S. H. Joo, R. Ryoo, M. Kruk, M. Jaroniec, Z. Liu, T. Ohsuna, and O. Terasaki, *J. Am. Chem. Soc.*, **122**, 10712 (2000).
- [34] F. Schüth, *Angew. Chem. Int. Ed.*, **42**, 3604 (2003).
- [35] H. Yang, and D. Zhao, *J. Mater. Chem.*, **15**, 1217 (2005).

- [36] C. M. Yang, C. Weidenthaler, B. Spliethoff, M. Mayanna, and F. Schüth, *Chem. Mater.*, **17**, 355 (2005).
- [37] H. J. Shin, R. Ryoo, Z. Liu, and O. Terasaki, *J. Am. Chem. Soc.*, **123**, 1246 (2001).
- [38] Z. Liu, O. Terasaki, T. Ohsuna, K. Hiraga, H. J. Shin, and R. Ryoo, *Chem. Phys. Chem.*, **2**, 229 (2001).
- [39] Z. Liu, Y. Sakamoto, T. Ohsuna, K. Hiraga, O. Terasaki, C. H. Ko, H. J. Shin, and R. Ryoo, *Angew. Chem. Int. Ed.*, **39**, 3107 (2000).
- [40] Y. Doi, A. Takai, Y. Sakamoto, O. Terasaki, Y. Yamauchi, and K. Kuroda, *Chem. Commun.*, **46**, 6365 (2010).
- [41] A. Takai, Y. Doi, Y. Yamauchi, and K. Kuroda, *J. Phys. Chem. C*, **114**, 7586 (2010).
- [42] C. M. Yang, B. Zibrowius, W. Schmidt, and F. Schüth, *Chem. Mater.*, **16**, 2918 (2004).
- [43] H. Wang, H. Y. Jeong, M. Imura, L. Wang, L. Radhakrishnan, N. Fujita, T. Castle, O. Terasaki, and Y. Yamauchi, *J. Am. Chem. Soc.*, **133**, 14526 (2011).
- [44] Sujandi, S. E. Park, D. S. Han, S. C. Han, M. J. Jin, and T. Ohsuna, *Chem. Comm.*, 4131 (2006).
- [45] S. Mostafa, F. Behafarid, J. R. Croy, L. K. Ono, L. Li, J. C Yang, A. I. Frenkel, and B. R. Cuenya, *J. Am. Chem. Soc.*, **132**, 15714 (2010).
- [46] V. Komanicky, H. Iddir, K. Chang, A. Menzel, G. Karapetrov, D. Hennessy, P. Zapol, and H. You, *J. Am. Chem. Soc.*, **131**, 5732 (2009).

Chapter 5

Microwave-Assisted Rapid Synthesis of Branched Platinum Nanoclusters with High Surface Area

5.1. Introduction

Synthesis of nanostructured platinum with controlled size and morphology to finely manipulate the platinum properties, which is a typical example of materials nanoarchitectures that emphasizes the importance of novel size and shape dependent properties, is of particular interest for many important application, e.g., catalysis [1-8]. Lots of platinum nanostructures with specific structural features, such as nanospheres [9-11], nanofibers [12], nanowires [13-15], nanotubes [16], nanowheels [17], porous nanoparticles [18] and mesoporous nanostructures [19-23], etc, have been successfully prepared by various strategies, mainly including templated and templatless strategies. In the previous work, I have proposed facile approaches to the rational synthesis of mesoporous platinum structures by using the lyotropic liquid crystals (LLC) as soft template [12, 16, 20-23].

Increasing interest in synthesis of nanostructured platinum is inspired by the unique catalytic property of platinum and desired utilization efficiency [5-8]. Branching out is a promising strategy to improve the specific surface area of platinum nanomaterials. But, it is high challenge work to produce branched platinum nanostructures due to the fact that platinum itself has inherently symmetric nature of face-centered cubic (fcc) structure [24]. Very few examples of the preparation of platinum nanostructures with branched morphologies, e.g., platinum nanodendrites, are demonstrated to date [25-27]. For example, Chang et al. produced platinum nanodendrites from the reduction of PtCl_6^{2-} ions via galvanic replacement reactions with Te nanowires at 90 °C [28]; Knoll et al. prepared porous flowerlike platinum nanostructures based on high temperature thermolytic reduction of $\text{trans-Pt}(\text{NH}_3)_2\text{Cl}_2$ in organic solution-phase (oleylamine, OAm) [29]; EI-Sayed et al. obtained multiarmed platinum nanostars by using tetrahedral platinum nanocrystals seeded growth [30]. It is noted that most demonstrated syntheses used for producing branched platinum nanostructures are time-consuming and require multi-steps, making the strategies to be scaled up difficultly. Developing a rapid and efficient strategy to produce platinum nanomaterials with high surface area is still an urgent

question to be solved. Alternately, besides synthesis of platinum nanodendrites, design and synthesis of the interconnected platinum nanoclusters (PNCs) with porous structures provide another new promising route to improve the specific surface area. Besides reducing platinum consumption, the presence of porous interconnected structures in the PNCs favors the high accessibility of guest species, most likely resulting in high performance in various applications, e.g., catalytic applications.

Herein, a rapid, one-step and efficient wet chemical route to straightforwardly produce PNCs in high yield is proposed without the need for any organic solvent, template or ion replacement, which is carried out simply by microwave-based heat-treatment of an aqueous solution containing K_2PtCl_4 and 2-[4-(2-hydroxyethyl)-1-piperazinyl]ethane sulfonic acid (HEPES) within 12 s. Importantly, as-prepared PNCs are porous interconnected nanostructures and possess very high surface area. These merits are advantageous for catalytic applications.

Usually, HEPES is used for preparing pH buffer solution. Recent investigations have shown that HEPES can serve as efficient reductant and stabilizer in preparation of Au [31] and Ag [32] nanoparticles. To date, the HEPES mediated synthetic strategy is limited to prepare Au and Ag nanoparticles. To further explore the potential merits of the HEPES mediated synthetic strategy, it is worth developing HEPES mediated synthetic strategy to produce platinum nanostructures with a large number of edge and corner atoms. It has been testified that the presence of edge and corner atoms favors improving the catalytic performance of nanostructured platinum [30, 33]. To the best of our knowledge, this is the first report on the synthesis of porous interconnected PNCs by using HEPES mediated synthetic strategy. Furthermore, the proposed approach is very simple, rapid, and straightforward.

5.2. Experimental Process

5.2.1. Materials

K_2PtCl_4 and HEPES were purchased from Nacalai Tesque Inc. (Kyoto, Japan). All the reagents were used as received without further purification. All solutions were prepared with deionized water treated in a Millipore water purification system (Millipore Corp.).

5.2.2. Synthesis of platinum nanoclusters

K_2PtCl_4 solution was prepared by dissolving K_2PtCl_4 in water under ambient condition and was aged at least 24 h before use. Aging the platinum solution disproportionated the complex into an equilibrium mixture of 42 % $Pt(H_2O)_2Cl_2$, 53 % $Pt(H_2O)Cl_3^-$, and 5 % $PtCl_4^{2-}$ [1].

In a typical synthesis of the PNCs, 5 mL 20 mM K_2PtCl_4 aqueous solution containing 0.1 M HEPES was placed in a 30 mL microwave sealed vessel. The mixture solution was then irradiated in a domestic microwave operated at 100 % power of 500 W for 12 s. The color of the reaction solution changed from transparent light brownish-yellow to opaque black within 12 s. Residual HEPES was removed by high-speed centrifugation. The collected product was dried or redispersed in water with sonicating to produce a colloidal suspension for further characterization.

5.2.3. Characterization

Transmission electron microscope (TEM) and high-resolution transmission electron microscope (HRTEM) were carried out by using a JEOL JEM-2100F operated at 200 kV equipped with energy dispersive spectrometer (EDS) analyses. The sample for TEM and HRTEM characterization was prepared by depositing a drop of dilute sample solution on a carbon-coated copper grid and dried at room temperature. Wide-angle powder X-ray diffraction (XRD) pattern were obtained with a Rigaku Rint 2500X diffractometer with Cu $K\alpha$ radiation (40 kV, 100 mA)

operated by using a step scan program (step width 0.05°). N_2 adsorption and desorption was obtained by using a Belsorp 28 apparatus (Bel Japan, Inc.) at 77 K.

5.3. Results and Discussion

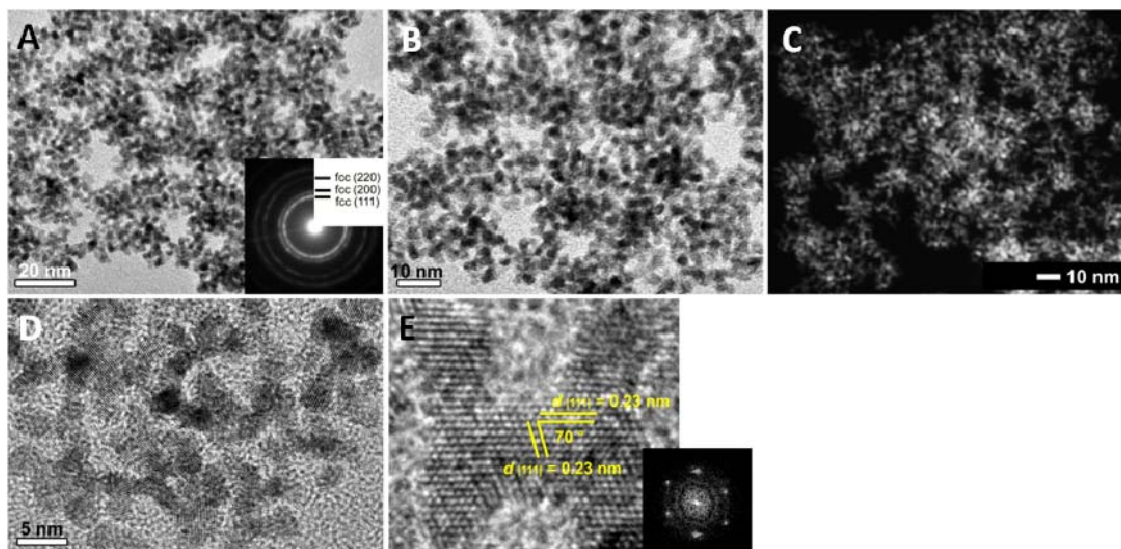


Figure 5.1 TEM images at different magnifications (A and B), dark-field TEM image (C), and HRTEM images (D and E) of the product. The inset in (A) shows the SAED pattern and the inset in (E) shows the FFT pattern.

K_2PtCl_4 reduction occurred very quickly with the help of microwave-based heat-treatment in the presence of HEPES which served as both efficient reductant and stabilizer for the producing the PNCs. The color of the reaction solution quickly changed from light brownish-yellow (from the platinum complex) to opaque black within 12 s, indicating that platinum nanostructures could be readily formed by this process in such a very short time. From the molecular structure of HEPES, it was known that HEPES has three functional groups, i.e. piperazine, hydroxyl, and sulfonate. Among them, piperazine and hydroxyl groups were principally responsible for the reduction of platinum complex under microwave-based heat-treatment. The morphology and size of the typical produced PNCs were characterized by TEM. The TEM image obtained at lower magnification revealed the presence of abundant PNCs (**Figure 5.1A**). No other platinum nanostructures

were observed, demonstrating the high yield formation of the PNCs (~ 100%). Higher magnification image indicated the PNCs were formed by aggregation of irregular nanoparticles to porous interconnected clusters. (Figure 5.1B). The porous and interconnected nature of the product was more evident in the images obtained by scanning TEM using a high-angle annular dark-field (HAADF) (Figure 5.1C). The lattice fringes in the HRTEM image confirmed that each aggregated irregular nanoparticle was single-crystalline nature (Figure 5.1D). The lattice fringes corresponded to (111) planes of platinum, because both d spacings were 0.23 nm and the dihedral angle was about 70° (Figure 5.1E). The inserted Fast Fourier Transform (FFT) pattern of the HRTEM image, shown in the inset of Figure 5.1E, further testified that the individual irregular nanoparticle was a single crystal and could be indexed by an incident electron beam.

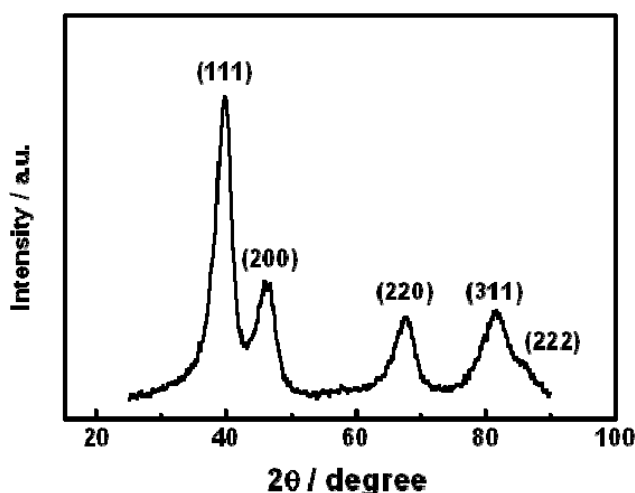


Figure 5.2 XRD pattern of the produced PNCs.

The chemical composition of the obtained PNCs was determined by energy dispersive X-ray (EDX) analysis of the samples coated on the TEM grids. The EDX spectrum testified the existing of the Pt element, in which the peaks of the corresponding element Pt were distinct (data not shown). The X-ray diffraction (XRD) pattern of the product was as expected for fcc platinum crystal structure (Figure 5.2) consistent with the selected area electron diffraction (SAED) pattern of

the sample (**Figure 5.1A Inset**).

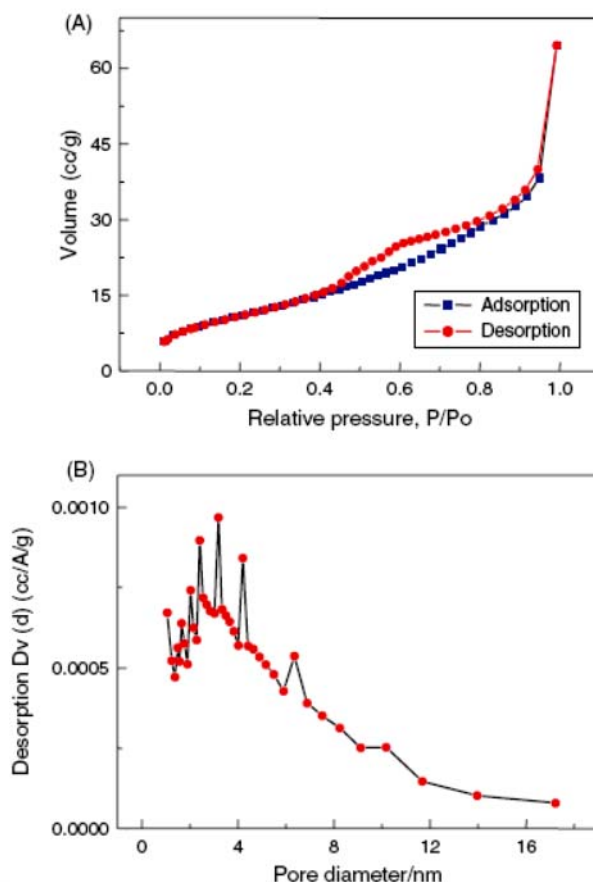


Figure 5.3 N₂ adsorption-desorption isotherm of the product (A) and the pore-size distribution curve obtained from BJH method (B).

High surface area was expected for as-prepared interconnected PNCs. Analysis of isotherms of the PNCs, as shown in **Figure 5.3A**, gave a surface area of 41 m²·g⁻¹. This value was very close to a half of the value of 81 m²·g⁻¹, calculated roughly for the surface area of nanowires with 2.3 nm in average diameter, indicating that the near half of the interconnected inner edges and corner areas were readily accessible from outside. For comparison, the specific surface area of platinum black range from 20 to 28 m²·g⁻¹ [34]. Porous platinum nanoparticles prepared by using complicated organic phase or by reaction-limited aggregation of nanoparticles possessed a surface area of 14 m²·g⁻¹ [18] and 39 m²·g⁻¹ [35],

respectively.

To better understand the interconnected nature of the product, the pore-size distribution of the product was further investigated by using the Barrett-Joyner-Halenda (BJH) method. BJH pore-size analysis gave a random distribution of pore sizes ranging from 1 to 11 nm (**Figure 5.3B**) and the broadness of the distribution indicated that the pores were not well defined. These pores most likely corresponded to the void space of the interconnected irregular nanoparticles observed in the TEM images (**Figure 5.1**).

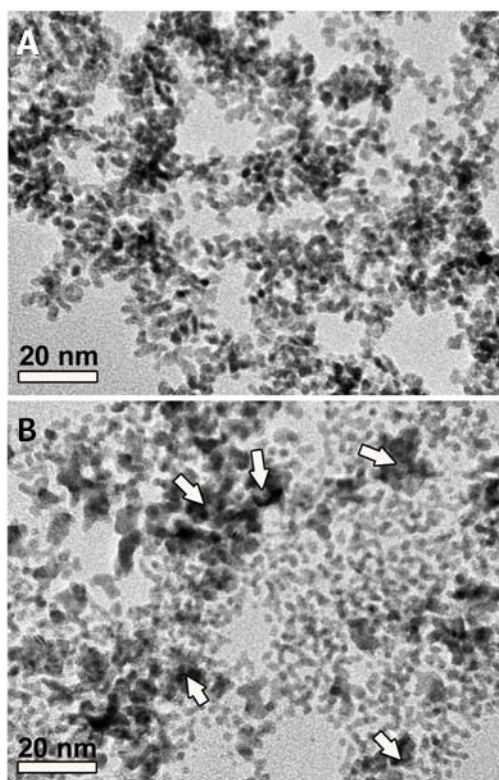


Figure 5.4 Typical TEM images of the platinum nanostructures prepared at different HEPES concentrations: 0.05 M (A) and 0.5 M (B), respectively, under the identical conditions used for preparing typical PNCs. The arrows indicate large irregular nanoparticles.

Usually, the formation of metal nanostructures with specific feature is highly dependent on the concentrations and ratios of the used reagents [36, 38]. Thus,

investigations were performed in which different concentrations of HEPES or platinum precursor were used. The effect of the HEPES concentration on the formation of the PNCs was investigated by using 0.05 M and 0.5 M HEPES, respectively and as-produced product was characterized by TEM (**Figure 5.4**). At the lower HEPES concentration (0.05 M), PNCs could also be obtained as shown in **Figure 5.4A**. The diameter and morphology of each interconnected irregular nanoparticle in the product were similar to that of the typical produced sample (**Figure 5.1**). Higher HEPES concentration (0.5 M) used, the product was only composed with many irregular nanoparticles and no obvious interconnected nature was observed, these particle sizes were distributed roughly from 1.8 to 15 nm (**Figure 5.4B**). When HEPES was left out of this synthetic system, no product could be obtained, demonstrating that HEPES played crucial role in the investigated system to produce PNCs.

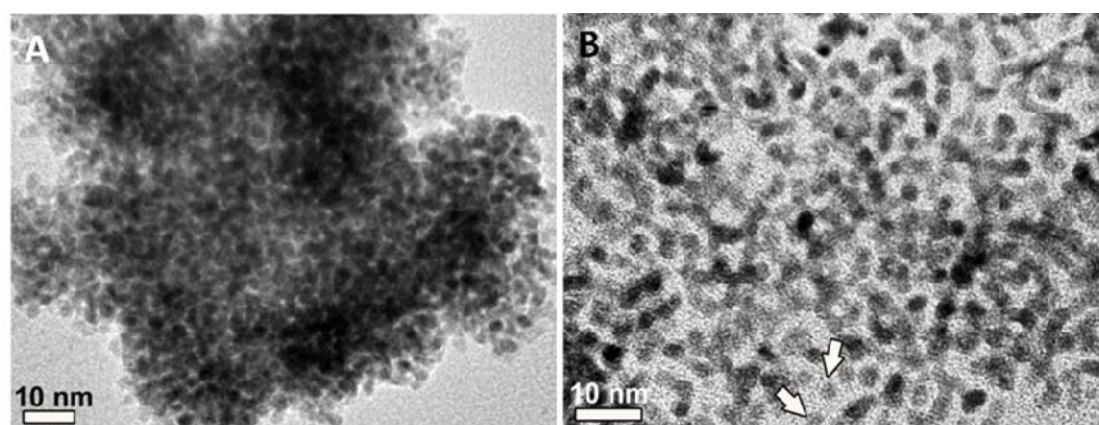


Figure 5.5 Typical TEM images of the platinum nanostructures prepared at different platinum precursor concentrations: 40 mM (A) and 5 mM (B), respectively, under the identical conditions used for preparing typical PNCs. The arrows indicate regular nanoparticles.

The used amount of platinum precursor was apparently one of the key factors in the synthesis of the PNCs. Higher platinum precursor concentration (40 mM) produced PNCs in highly aggregation form (**Figure 5.5A**). The platinum precursor concentration affected the formation rate of the monomer Pt^0 (seeds) and the corresponding rates for nucleation and crystal growth. Lower platinum

concentrations (5 mM) used, the amount of the monomer Pt^0 was not enough to construct PNCs, and only irregular nanoparticles (~ 96 %) together with very few regular nanoparticles (~ 4 %) were observed (**Figure 5.5B**).

To date, microwave irradiation has been demonstrated to be an effective means for rapid synthesis of metal nanostructures [39]. Supported [40-43] and unsupported [39] platinum nanostructures have been synthesized by microwave heating under appropriate conditions in which microwave polyol process was the commonly used strategy and ethylene glycol (EG) was one of the prerequisites [41-43]. Compared with the microwave polyol synthesis of platinum nanomaterials, the proposed water-based microwave system provided a more well-suited route for the synthesis of platinum nanomaterials. Furthermore, comparing to EG, HEPES offered a more environmentally benign in microwave synthesis. The combination of simple implement with the high surface area of the product made the presented synthetic strategy to be highly valuable for synthesis of platinum nanomaterials with high surface area.

5.4. Conclusion

In summary, PNCs were straightforwardly produced in high yield simply by microwave-based heat-treatment of an aqueous solution containing K_2PtCl_4 and HEPES within 12 s. The advantages of the proposed approach to produce the PNCs are obvious. First, this approach is very simple, rapid and feasible. Second, no organic solvents, templates or ion replacements are needed. Furthermore, the proposed HEPES mediated synthesis might provide new strategy for rapid and efficient creation of novel metal nanomaterials. The porous interconnected nanoarchitectures of the PNCs together with its high surface area are scientifically interesting and technically important. As-prepared PNCs have great potential as electrocatalysts in fuel cells, which will be the next issue.

References

- [1] Y. Song, Y. Yang, C. J. Medforth, E. Pereira, A. K. Singh, H. Xu, Y. Jiang, C. J. Brinker, F. Swol, and J. A. Shelnut, *J. Am. Chem. Soc.*, **126**, 635 (2004).
- [2] N. Tian, Z. Y. Zhou, S. G. Sun, Y. Ding, and Z. L. Wang, *Science*, **316**, 732 (2007).
- [3] C. Wang, H. Daimon, T. Onodera, T. Koda, and S. H. Sun, *Angew. Chem. Int. Ed.*, **47**, 3588, (2008).
- [4] C. Wang, H. Daimon, Y. Lee, J. Kim, and S. H. Sun, *J. Am. Chem. Soc.*, **129**, 6974 (2007).
- [5] B. Lim, X. M. Lu, M. J. Jiang, P. H. C. Camargo, E. C. Cho, E. P. Lee, and Y. N. Xia, *Nano Lett.*, **8**, 4043 (2008).
- [6] K. M. Bratlie, H. Lee, K. Komvopoulos, P. D. Yang, and G. A. Somorjai, *Nano Lett.*, **7**, 3097 (2007).
- [7] L. Wang and Y. Yamauchi, *J. Am. Chem. Soc.*, **131**, 9152 (2009).
- [8] L. Wang and Y. Yamauchi, *Chem. Mater.*, **21**, 3562 (2009).
- [9] N. C. Bigall, T. Hartling, M. Klose, P. Simon, L. M. Eng, and A. Eychmuller, *Nano Lett.*, **8**, 4588 (2008).
- [10] H. P. Liang, H. M. Zhang, J. S. Hu, Y. G. Guo, L. J. Wan, and C. L. Bai, *Angew. Chem. Int. Ed.*, **43**, 1540 (2004).
- [11] H. M. Chen, R. S. Liu, M. Y. Lo, S. C. Chang, L. D. Tsai, Y. M. Peng, and J. Lee, *J. Phys. Chem. C*, **112**, 7522 (2008).
- [12] Y. Yamauchi, A. Takai, T. Nagaura, S. Inoue, and K. Kuroda, *J. Am. Chem. Soc.*, **130**, 5426 (2008).
- [13] Y. J. Song, R. M. Garcia, R. M. Dorin, H. R. Wang, Y. Qiu, E. N. Coker, W. A. Steen, J. E. Miller, and J. A. Shelnut, *Nano Lett.*, **7**, 3650 (2007).
- [14] S. H. Sun, F. Jaouen, and J. P. Dodelet, *Adv. Mater.*, **20**, 3900 (2008).
- [15] E. P. Lee, Z. M. Peng, D. M. Cate, H. Yang, C. T. Campbell, and Y. N. Xia, *J. Am. Chem. Soc.*, **129**, 10634 (2007).
- [16] A. Takai, Y. Yamauchi, and K. Kuroda, *Chem. Commun.*, 4171 (2008).

- [17] Y. J. Song, R. M. Dorin, R. M. Garcia, Y. B. Jiang, H. R. Wang, P. Li, Y. Qiu, F. Swol, J. E. Miller, and J. A. Shelnut, *J. Am. Chem. Soc.*, **130**, 12602 (2008).
- [18] X. W. Teng, X. Y. Liang, S. Maksimuk, and H. Yang, *Small*, **2**, 249 (2006).
- [19] G. S. Attard, P. N. Bartlett, N. R. B. Coleman, J. M. Elliott, J. R. Owen, and J. H. Wang, *Science*, **278**, 838 (1997).
- [20] Y. Yamauchi, A. Sugiyama, R. Morimoto, A. Takai, and K. Kuroda, *Angew. Chem. Int. Ed.*, **47**, 5371 (2008).
- [21] Y. Yamauchi, A. Takai, M. Komatsu, M. Sawada, T. Ohsuna, and K. Kuroda, *Chem. Mater.*, **20**, 1004 (2008).
- [22] Y. Yamauchi, T. Momma, M. Fuziwara, S. S. Nair, T. Ohsuna, O. Terasaki, T. Osaka, and K. Kuroda, *Chem. Mater.*, **17**, 6342 (2005).
- [23] Y. Yamauchi and K. Kuroda, *Chem. Asian J.*, **3**, 664 (2008).
- [24] S. Cheong, J. Watt, B. Ingham, M. F. Toney, and R. D. Tilley, *J. Am. Chem. Soc.*, **131**, 14590 (2009).
- [25] L. Wang, S. J. Guo, J. F. Zhai, and S. J. Dong, *J. Phys. Chem. C*, **112**, 13372 (2008).
- [26] Y. J. Song, Y. B. Jiang, H. R. Wang, D. A. Pena, Y. Qiu, J. E. Miller, and J. A. Shelnut, *Nanotechnology*, **17**, 1300 (2006).
- [27] M. H. Ullah, W. S. Chung, I. Kim, and C. S. Ha, *Small*, **2**, 870 (2006).
- [28] Z. H. Lin, M. H. Lin, and H. T. Chang, *Chem. Eur. J.*, **15**, 4656 (2009).
- [29] X. H. Zhong, Y. Y. Feng, I. Lieberwirth, and W. Knoll, *Chem. Mater.*, **18**, 2468 (2006).
- [30] M. A. Mahmoud, C. E. Tabor, M. A. El-Sayed, Y. Ding, and Z. L. Wang, *J. Am. Chem. Soc.*, **130**, 4590 (2008).
- [31] B. K. Jena and C. R. Raj, *Langmuir*, **23**, 4064 (2007).
- [32] R. W. Y. Sun, R. Chen, N. P. Y. Chung, C. M. Ho, C. L. S. Lin, and C. M. Che, *Chem. Comm.*, 5059 (2005).
- [33] Y. J. Xiong, B. J. Wiley, and Y. N. Xia, *Angew. Chem. Int. Ed.*, **46**, 7157 (2007).
- [34] K. S. Choi, E. W. McFarland, and G. D. Stucky, *Adv. Mater.*, **15**, 2018 (2003).
- [35] B. Viswanath, S. Patra, N. Munichandraiah, and N. Ravishankar, *Langmuir*, **25**, 3115 (2009).
- [36] L. H. Lu, A. Kobayashi, K. Tawa, and Y. Ozaki, *Chem. Mater.*, **18**, 4894 (2006).

- [37] Y. L. Wang, P. H. C. Camargo, S. E. Skrabalak, H. C. Gu, and Y. N. Xia, *Langmuir*, **24**, 12042 (2008).
- [38] T. K. Sau and C. J. Murphy, *J. Am. Chem. Soc.*, **126**, 8648 (2004).
- [39] N. N. Mallikarjuna and R. S. Varma, *Cryst. Growth Des.*, **7**, 686 (2007).
- [40] Z. Q. Tian, S. P. Jiang, Y. M. Liang, and P. K. Shen, *J. Phys. Chem. B*, **110**, 5343 (2006).
- [41] X. Li, W. X. Chen, J. Zhao, W. Xing, and Z. D. Xu, *Carbon*, **43**, 2168 (2005).
- [42] J. Zhao, P. Wang, W. X. Chen, R. Liu, X. Li, and Q. L. Nie, *J. Power Sources*, **160**, 563 (2006).
- [43] H. Xu, L. P. Zeng, S. J. Xing, Y. Z. Xian, and L. T. Jin, *Electrochem. Commun.*, **10**, 551 (2008).

Chapter 6

Synthesis of Mesoporous Pt Films with Tunable Pore Sizes from Aqueous Surfactant Solutions

6.1. Introduction

Currently, platinum (Pt) is widely used as industrial catalysts and battery electrodes, because of its usefulness as a heavy, durable, and malleable metal, as well as its chemical functions as a catalyst in a number of reactions. Pt becomes an essential metal in key manufacturing processes in automobile, chemical, petroleum refining, pharmaceutical, and electronic fields, thereby increasingly being used by the industries. However, Pt represents one of the world's most precious and rarest metals. In view of the strong social demand for the reduced use of rare metals, there have been heightened calls for the development of a technology for securing high functionality with low use of Pt by producing nanostructured materials with larger surface areas.

Active research on the synthesis of new Pt nanomaterials, including nanoparticles, nanotubes, nanosheets, nanodendrites, and nanoporous materials has been underway for a number of years. Nanoparticles with a large surface area have been synthesized by the reverse micelle method and other processes [1, 2]; however, low thermal stability has been mentioned as an issue because the particles tend to agglomerate when heated to high temperature due to their small size. The surface areas of the nanotubes [3], nanosheets [4], and nanodendrites [5, 6] were limited to around $25 \text{ m}^2\cdot\text{g}^{-1}$, which is the same level as the platinum black used as an industrial catalyst. An approach of dealloying, in which a less noble metal is selectively dissolved from a bimetallic alloy, is an attractive strategy to synthesize nanoporous metals without the use of surfactants; however, it is hard to control precisely nanopore size [7, 8].

To overcome these problems, new types of metal-based mesoporous materials with very uniform mesopores and extremely high surface areas have been developed rapidly. Although many mesoporous materials with various compositions [9-15] and morphologies [16-19] have been reported to date since the discovery of mesoporous materials in the early 1990s [9-11], metal-based mesoporous materials "mesoporous metals" are of considerable interest for several applications in metal catalysis, battery and fuel cell electrodes, capacitors, and sensor devices. The previous synthesis of mesoporous metals have been synthesized based on the concept of direct replication from templates (i.e., molds). Most of the mesoporous metals have been prepared by

using mesoporous silicas as hard templates [20, 21]. Ordered lyotropic liquid crystalline phases with very high surfactant concentrations (over 50 wt %) have been utilized as alternative soft templates [22-25]. In this process, by taking the phase diagram of the surfactant/metal salts/water system into consideration, the final mesostructures can be controlled by changing surfactant sizes and concentrations [25]. Currently, the variations of possible mesostructures are expanding to include lamellar and 3D cage-type, as well as 2D hexagonal mesostructures, through the use of block copolymers [26, 27] or the addition of expanders into liquid crystal systems [28]. It was reported that the self-assembly of block copolymers with ligand-stabilized platinum nanoparticles provided access to ordered arranged mesostructures [29, 30]. Despite considerable progress with mesoporous metals, however, the synthetic process is still very complex, and the controllability of the pore sizes in mesoporous metal systems is much more limited compared to that in mesoporous silica systems [12-31].

In this chapter, I propose a route to mesoporous metal films with various pore sizes by a simple electrodeposition method in an aqueous surfactant solution, in contrast to a traditional route based on the concept of direct replication [20-23, 26-30]. The mesopore sizes in the deposited films can be widely tuned from 5 to 30 nm, by changing the sizes of the used surfactants and adding a hydrophobic aromatic compound as an expander. The frameworks in the obtained mesoporous Pt films are composed of connected Pt nanoparticles (around 3 nm diameter). Interestingly, the Pt atomic crystallinity is coherently extending across over several Pt nanoparticles, providing a large number of atomic steps and defect sites, which can facilitate the cleavage of the C–H and O–H bonds in methanol decomposition [32, 33]. As a result of high surface areas and unique Pt surface structure, electrochemical performance for methanol electro-oxidation dramatically enhanced, compared to commercially available carbon-supported Pt nanoparticles and unsupported Pt nanoparticles (i.e., Pt black).

6.2. Experimental Process

6.2.1. Materials

K_2PtCl_4 was purchased from Nacalai Tesque, Inc. (Kyoto, Japan). Pluronic F127 and Brij 58 were obtained from Sigma. $\text{PEO}_{4500}\text{-PPO}_{3200}\text{-PEO}_{4500}$ was ordered from Polymer Source Company. Pt black (HiSPEC 1000) and carbon-supported Pt nanoparticles (HiSPEC 3000, 20 wt % Pt on carbon black) were purchased from Johnson Matthey Company.

6.2.2. Electrodeposition

Electrochemical fabrication of Pt mesoporous films was performed by using the electrochemical machine (CHI 842B electrochemical analyzer, CHI Instrument, U.S.) with a standard three-electrode cell system, including an Ag/AgCl (saturated KCl) electrode as the reference electrode, a platinum wire as the counter electrode, and a working electrode. The working electrode included an indium tin oxide (ITO) substrate or a gold substrate. For the preparation of the electrolyte, 1.0 wt % nonionic surfactant (e.g., Pluronic F127, $\text{PEO}_{4500}\text{-PPO}_{3200}\text{-PEO}_{4500}$, and Brij 58 $\text{C}_{16}\text{EO}_{20}$) was dissolved in 20 mM K_2PtCl_4 aqueous solution. The Pt depositions were performed at the potential of -0.2 V for 10 min without stirring at room temperature. After the deposition, as fabricated films were placed in ethanol for 12 h to extract the nonionic surfactant and then were thoroughly rinsed with deionized water and dried in air for further characterization.

6.2.3. Characterizations

Scanning electron microscopy (SEM) images were obtained using a Hitachi HR-SEM S-5500 microscope. Powder samples without coating were observed directly. The accelerating voltage was 10 kV. Transmission electron microscopy (TEM) was carried out using a JEOL JEM-3010 ($C_s = 0.6$ mm, point resolution 1.7 Å) operated at 300 kV. SAXS patterns were recorded by a Rigaku NANO-Viewer (Microfocus rotating anode, Cu $K\alpha$ radiation) with the camera length = 700 mm operated at 40 kV and 30

mA. To evaluate the size distribution of Pt nanoparticles, as well as the mesopores, the observed small-angle X-ray scattering (SAXS) profiles were analyzed using a spherical model and a Γ -distribution function where the Percus–Yevick type interparticle/intermesopore correlation was taken into account. The fitting 2θ ranges were carefully chosen so that the scattering from mesopore arrangement can be discriminated from that of Pt nanoparticles. SAXS intensities of Brij 58 micelles in water and 20 mM K_2PtCl_4 solution were measured by SAXS Kratky-type camera (Anton Paar, Graz) equipped with a block collimator and a fine line-focus sealed X-ray tube (Cu $\text{K}\alpha$ radiation, $\lambda = 0.154$ nm) operated at 40 kV and 50 mA. The available q -range was 0.08 – 6.00 nm^{-1} . Indirect Fourier transformation (IFT) technique was employed to yield a real space picture of the micellar structure. Solution density of 1.0 wt % Brij 58 in 20 mM K_2PtCl_4 was measured using a high-precision DMA4500 M densimeter (Anton Paar, Graz). Methanol electrocatalytic oxidation measurements were carried out in 0.5 M H_2SO_4 solution containing 1 M methanol; the scan rate was 20 $\text{mV}\cdot\text{s}^{-1}$. In the electrocatalytic investigations, the ECSAs were used to normalize the current. ECSA was determined from the charge associated with the hydrogen adsorption and desorption processes, and a conversion factor of 210 $\mu\text{C}\cdot\text{cm}^{-2}$ was used. The Pt weights were determined from the weights of the scratched Pt films.

6.3. Results and Discussion

Mesoporous Pt films were electrodeposited from an aqueous solution including K_2PtCl_4 and amphiphilic block copolymers (nonionic surfactants). Three types of nonionic surfactant with different molecular weights were used; EO4500-PO3200-EO4500, F127 ($\text{EO}_{100}\text{-PO}_{65}\text{-EO}_{100}$), and Brij 58 ($\text{C}_{16}\text{-EO}_{20}$). The detailed synthetic procedure is given in the Supporting Information. The surfactant concentrations in the plating solutions were set at 1.0 wt %, which is above the critical micelle concentration (CMC) of surfactants (**Figure 6.1**). The surface morphology of the Pt films was observed by SEM, as shown in **Figure 6.2**. The Pt species was deposited uniformly on the substrates without any cracks or voids.

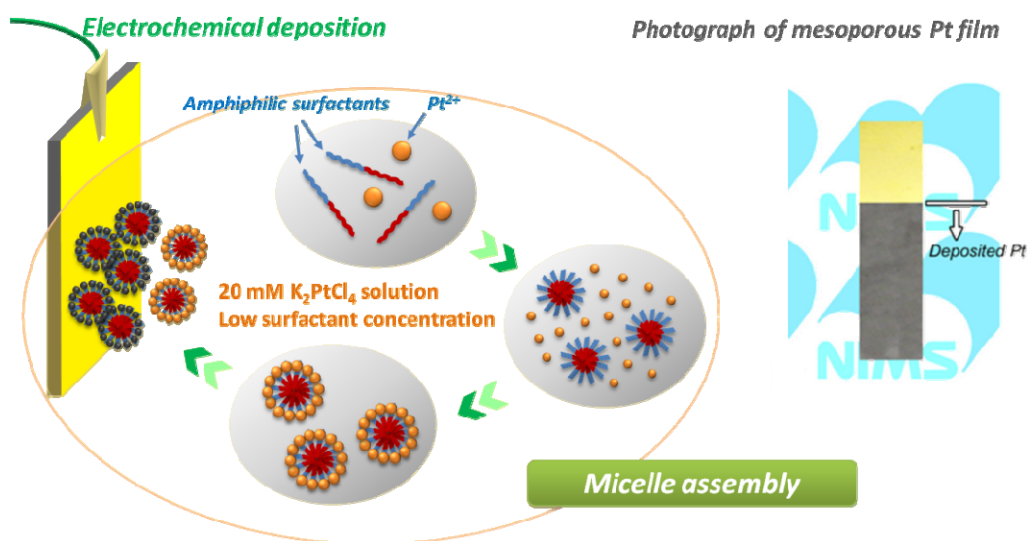


Figure 6.1 Synthetic concept of mesoporous Pt films. The surfactant concentration used in this study is over CMC. Inset image is photograph of the mesoporous Pt film deposited on Au substrate. The black area indicates the deposited Pt.

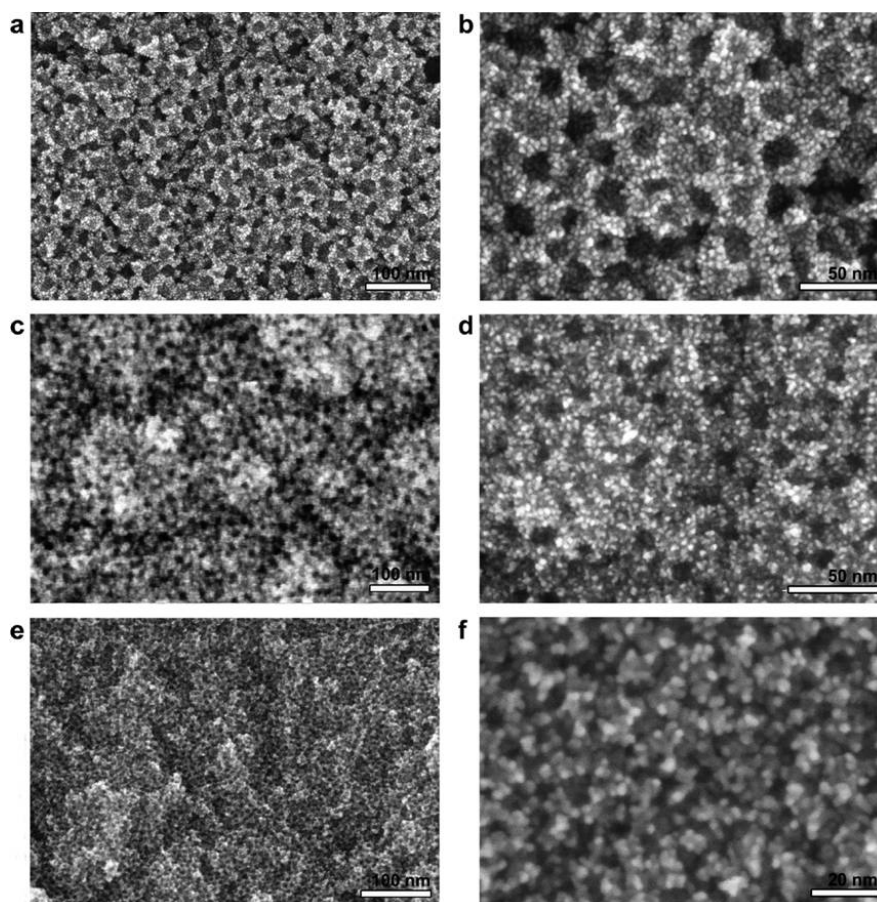


Figure 6.2 SEM images of mesoporous Pt films deposited on the ITO substrate: (a, b) PEO₄₅₀₀-PPO₃₂₀₀-PEO₄₅₀₀, (c, d) F127, and (e, f) Brij 58.

By using various surfactants with different chain lengths, the mesopore sizes were tuned in a wide range from 5 to 20 nm (**Figure 6.2**). The triblock copolymer, PEO₄₅₀₀-PPO₃₂₀₀-PEO₄₅₀₀, possessed the largest molecular weight among the surfactants used, realizing the maximum mesopore size (the observed mesopores were around 20 nm in diameter). In the films prepared with F127, mesopores with around 12 nm in diameter were observed. The mesopore sizes of the films prepared with diblock copolymers (Brij 58) were roughly calculated to be around 7 nm in diameter. In a comparative experiment, the Pt film was prepared without surfactants. No specific nanostructures were confirmed (**Figure 6.3a**), indicating that the dissolved surfactants played a key role in the creation of the mesoporous structures.

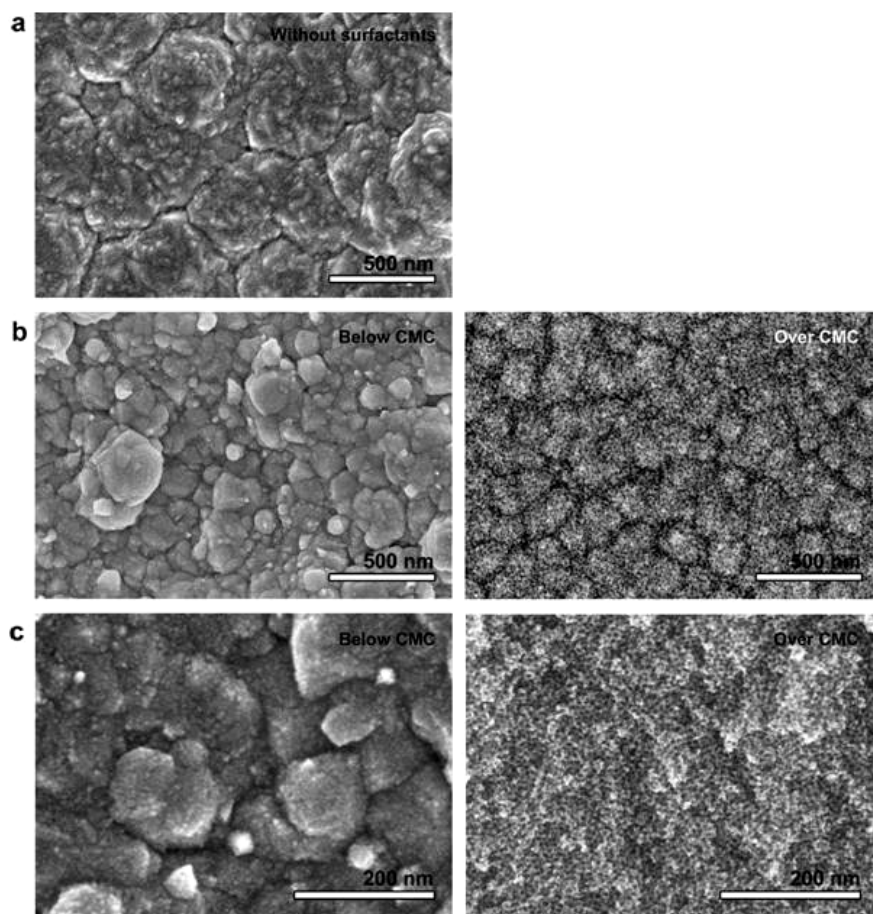


Figure 6.3 Typical SEM images of the Pt films prepared (a) without surfactants, (b) with F127 surfactants, and (c) with Brij 58. The effect of surfactant concentrations are examined in both F127 and Brij 58 systems.

Furthermore, the size distributions of the mesopores in the obtained mesoporous Pt films were evaluated by SAXS measurement (**Figure 6.4**). The observed SAXS profiles were fitted based on the model that mesopore spheres are surrounded by Pt with a certain packing fraction. Each SAXS profile shows a clear bump up to 1.0° that is ascribed to the correlation of underlying mesopore packings, where the mesopore packing fraction estimated by the Percus–Yevick approximation was ca. 15%. The peak tops of the mesopore size distribution curves (**Figure 6.4d**) were located around 17 nm (for PEO₄₅₀₀-PPO₃₂₀₀-PEO₄₅₀₀), 10 nm (for F127), and 7 nm (for Brij 58), which underpinned the SEM observations given in **Figure 6.2**. With the increase of the

molecular weights of the used surfactants, the distribution curves broadened, suggesting that the Brij 58 could provide an opportunity to synthesize the best uniform mesopores among the present surfactants employed.

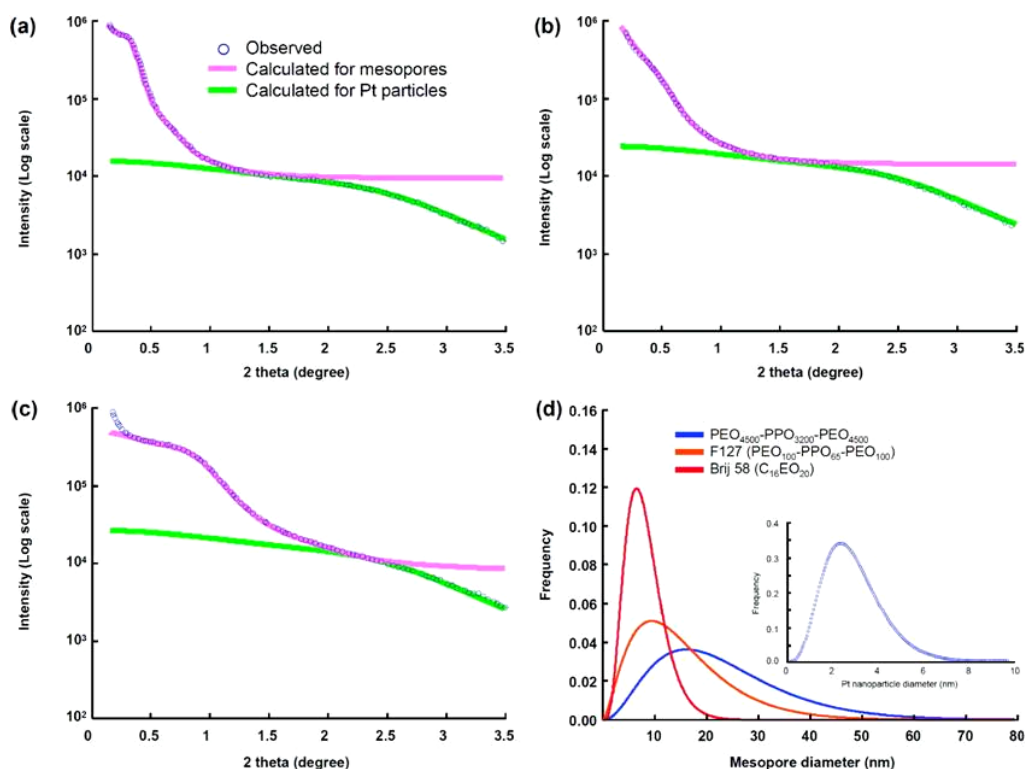


Figure 6.4 SAXS profiles of the mesoporous Pt films prepared with (a) PEO₄₅₀₀-PPO₃₂₀₀-PEO₄₅₀₀, (b) F127, and (c) Brij 58. Calculated profiles for the mesopores and the Pt nanoparticles are also noted. Size distributions of the mesopores prepared with different surfactants are evaluated from data fitted

at $2\theta = 0.15^\circ \sim 1.5^\circ$ (for (a) PEO₄₅₀₀-PPO₃₂₀₀-PEO₄₅₀₀), at $2\theta = 0.20^\circ \sim 1.8^\circ$ (for (b) F127), and at 2θ

$= 0.3^\circ \sim 2.0^\circ$ (for (c) Brij 58). The size distribution of the Pt nanoparticles was evaluated from

PEO₄₅₀₀-PPO₃₂₀₀-PEO₄₅₀₀ data fitted at $2\theta = 1.50^\circ \sim 3.5^\circ$, and the resultant distribution was assumed

to be common in the other samples (the scale factor was only optimized in each sample data). (d) Mesopore size distributions of all the samples estimated from the spherical model fitting to the observed profiles. Pt particle size distribution is also noted as the inset image.

I investigated further the detailed microstructure of the framework at a higher magnification. Interestingly, the framework in all the films was composed of the connected nanoparticles, with an average size of around 3 nm (**Figure 6.2b, d, f**). This observation was further quantified by the Pt size distribution drawn from the SAXS profiles (**Figure 6.4d, inset**). The average size of the Pt nanoparticles calculated by the SAXS profile were 2.7 ± 1.3 nm, which coincided with the value observed by SEM (**Figure 6.2**). When triblock copolymers such as PEO₄₅₀₀-PPO₃₂₀₀-PEO₄₅₀₀ and F127 were used, a few nanoparticles were aggregated to form the thick framework (**Figure 6.2b, d**). On the other hand, in the case of Brij 58, the framework thickness was decreased to around 3 nm, equal to one Pt nanoparticle size. Each Pt nanoparticle was exposed on both sides of the wall (**Figure 6.2f**). Therefore, almost all the surface of the Pt nanoparticles was exposed on the mesopores and can be effectively utilized as electrochemically active surface area.

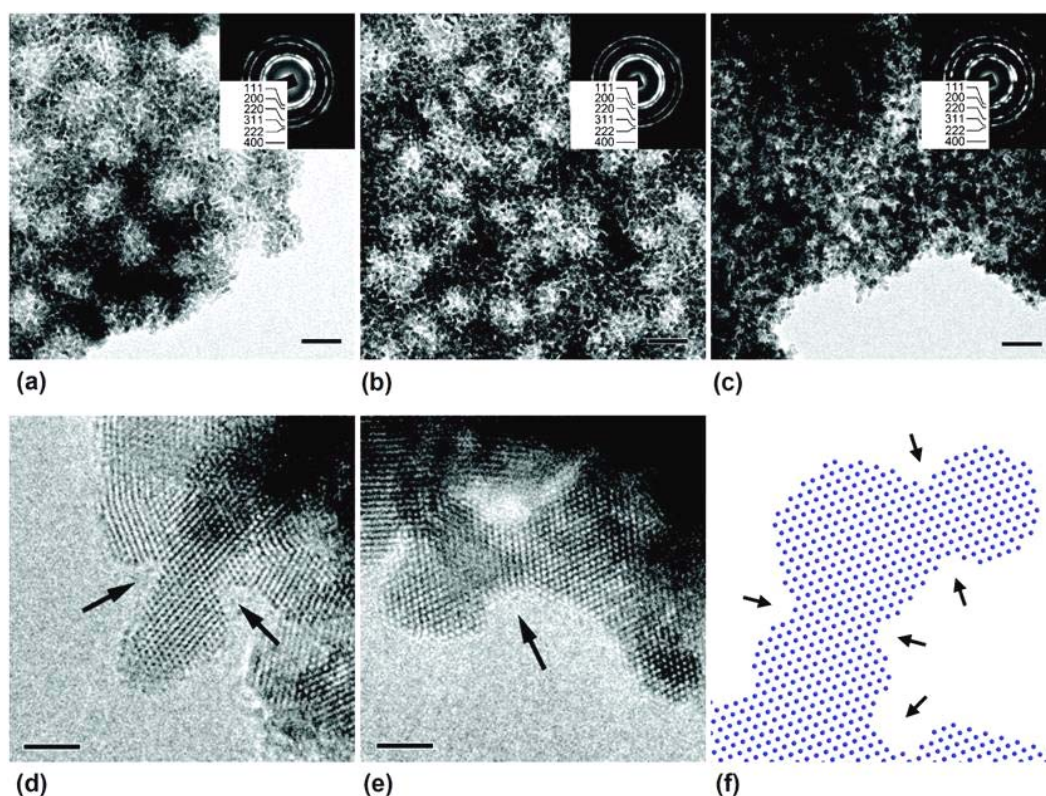


Figure 6.5 TEM images and the corresponding electrochemical deposition (ED) patterns of mesoporous Pt films prepared with (a) PEO₄₅₀₀-PPO₃₂₀₀-PEO₄₅₀₀, (b) F127, and (c) Brij 58. (d, e) High resolution TEM images of mesoporous Pt film prepared with Brij58. High index surface and concave surface are indicated by arrows. (f) Schematic drawing of the connection of Pt nanoparticles along the [110] direction. The ‘neck’ part of the connected particles has concave shapes indicated by arrows. Scale bars are (a, b, c) 20 nm and (d, e) 2 nm.

TEM images (**Figure 6.5a, b, c**) showed that all the Pt films consisted of nanoparticles with mesopores whose sizes were dependent on the used surfactants. Both sizes of Pt nanoparticle and mesopore well agreed with those observed in SEM images (**Figure 6.2**) and SAXS data (**Figure 6.4**). Higher magnification TEM images of Pt films prepared with Brij58 showed that Pt nanoparticles connected each other and the lattice fringes of the {111} plane went through all over the several nanoparticles (**Figure 6.5d, e**). Each nanoparticle showed a characteristic undefined shape with higher index surface, that is, a large number of steps, although metal nanoparticles tend to show faceted crystal morphology observed with low index surfaces such as {111} and {100} planes [1]. More interestingly, the connection of the nanoparticles with coherent crystal lattice resulted in a concave surface topology. The characteristic morphology,

that is, a large number of steps and concave surface, acts as not only active sites for catalytic reactions but also effective space geometries for catalytic substances (**Figure 6.5f**).

To understand the formation mechanism, the concentration of the dissolved surfactant (F127) was varied from 0.1 wt % to 2 wt %. With a decrease in the F127 concentration below CMC (the CMC of F127 is 0.7 wt %) [34, 35], no porous structures were obtained (**Figure 6.3b**). On the other hand, when the concentration of F127 was over the CMC, many spherical mesopores were formed in the films. A similar situation was observed in the Brij 58 system (**Figure 6.3c**). From the data, we can suppose that mesoporous Pt films are electrodeposited by the assembly of surfactant micelles with metal species. In the plating solution, dissolved Pt ions are coordinated by water molecules to form metal-aqua complexes. Since the coordinated water molecules usually interact with ethylene oxide (EO) groups of the surfactant micelles [24], the dissolved Pt ions adsorb inside the external EO region of the surfactant micelles. Therefore, during the electrochemical deposition (i.e., application of the potential voltages), the Pt species are thought to move to the working electrode together with the surfactant micelles. Thus, the surfactant micelles can act as structural direct agents.

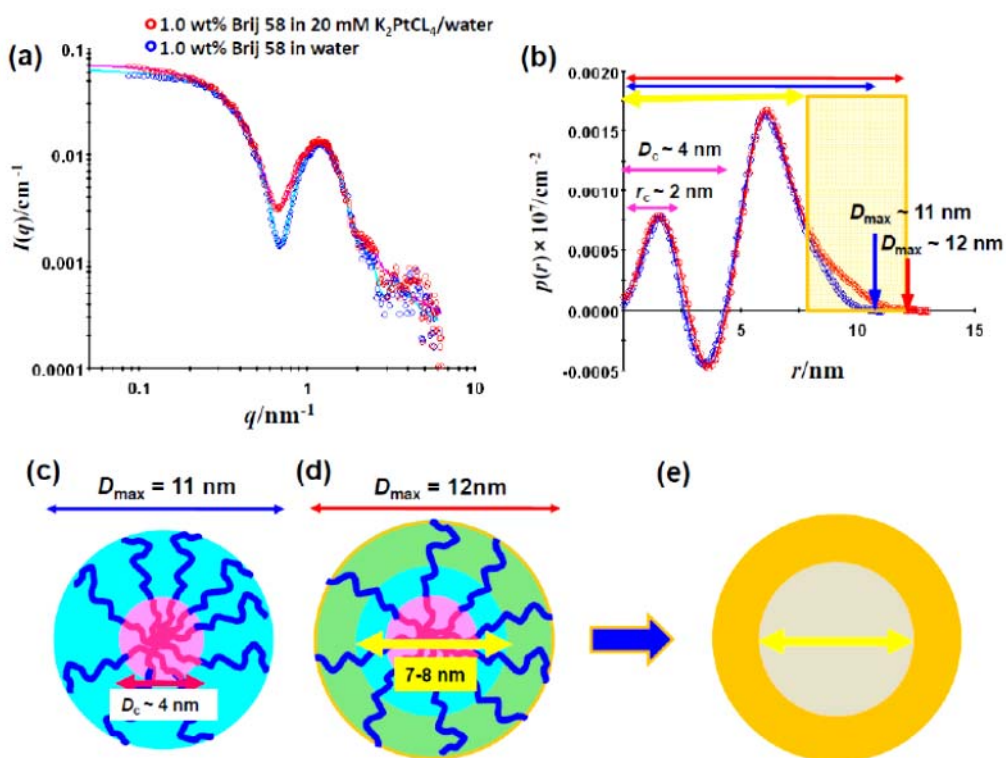


Figure 6.6 Particle characterization of Brij 58 micelles by small-angle X-ray scattering (SAXS). (a) SAXS profiles, $I(q)$, and (b) the resulting pair-distance distribution functions, $p(r)$, of 1.0 wt% Brij 58 in water and in 20 mM K_2PtCl_4 solution on absolute scale. (c and d) Schematic representation of the Brij 58 micelles (c) in water and (d) in 20 mM K_2PtCl_4 solution. (e) Suggested mesopore structure replicated from the Brij 58 micelle in 20 mM K_2PtCl_4 solution.

Note in Figure 6.6:

Density of 20 mM K₂PtCl₄ solution is 1.0034 g·cm⁻³, resulting in the electron density of 335.02 eI·nm⁻³, which is only 0.15 % greater than that for water (333.46 eI·nm⁻³). Therefore, the observed modification of the SAXS intensities upon replacing the solvent water with 20 mM K₂PtCl₄ solution could essentially be attributed to the difference of the micellar structures, instead of different contrast.

SAXS observes the structure of the particles via the convolution square of the electron density fluctuations, $\Delta\rho(\mathbf{r})$,

$$\gamma(r) \equiv \Delta\tilde{\rho}^2(r) = \langle \Delta\tilde{\rho}^2(\mathbf{r}) \rangle = \left\langle \int_{-\infty}^{\infty} \Delta\rho(\mathbf{r}_1) \Delta\rho(\mathbf{r}_1 - \mathbf{r}) d\mathbf{r}_1 \right\rangle \quad \text{--- (1)}$$

where r is the distance between two scattering centers chosen inside the particle. The so-called pair-distance distribution function, defined as $p(r) = \gamma(r) \cdot r^2$, is a real-space function that contains information about size, shape, and internal structure of the particle. The SAXS intensity, $I(q)$, of a dilute globular particle dispersion is given by the Fourier transformation of $p(r)$ as

$$I(q) = 4\pi \int_0^{\infty} p(r) \frac{\sin qr}{qr} dr \quad \text{--- (2)}$$

$p(r)$ is accessible by means of the well-established Indirect Fourier transformation (IFT) technique [36-38], which provides an intuitive real-space picture of the particle structure.

The precursor solution (1.0 wt % Brij 58 in 20 mM K_2PtCl_4 solution) was characterized by SAXS. For comparison, 1.0 wt % Brij 58 solution in water was also measured. In both cases, the pair-distance distribution function, $p(r)$, calculated using Indirect Fourier transformation (IFT) technique, confirmed the formation of spherical-like micelles (**Figure 6.6**), which possess a maximum diameter of ca. 11 nm in water, whereas it attains a slightly greater value (ca. 12 nm) in the presence of a K_2PtCl_4 source. The notable difference in $p(r)$ was seen in the high- r regime ($r > 7-8$ nm), which may indicate that Pt ion species are incorporated into the outermost part of the hydrophilic shell, as schematically shown in **Figure 6.6**. Therefore, the suggested imprinted mesopore sizes after Pt deposition on the micelles can be estimated to be around 7–8 nm, which is almost identical to the average pore sizes in mesoporous Pt films prepared with Brij 58 (**Figures 6.2e, f and 6.4d**). In another experiment, when 1,3,5-triisopropylbenzene ($0.006 \text{ g}\cdot\text{ml}^{-1}$, TIPBz) was dissolved in the original solutions and introduced into the cores of the surfactant micelles, the obtained mesopores sizes expanded up to 31 nm (for PEO₄₅₀₀-PPO₃₂₀₀-PEO₄₅₀₀), 18 nm (for F127), and 12 nm (for Brij 58) (**Figure 6.7**). Thus, mesopore sizes increased by 70–80% compared to the original mesopore sizes prepared without organic expanders. This evidence supports the described formation mechanism based on the surfactant micelle assembly.

There have been very few papers on mesoporous and nanoporous Pt [39, 40] and ZnO [41] films using aqueous surfactant solutions under the influence of an electrostatic potential. In these cases, even when the surfactant concentration is lower than CMC, micelle formation on the electrode surface is possible due to an electrostatic interaction between the surfactant and the electrode surface [40-43]. However, fine control of the hydrophilicity of the substrates, the ionic strength of the surfactants, and the counter ions is necessary. Also, the use of surfactants has been limited to only cationic CTAB and anionic SDS surfactants with small molecular weights. Therefore, the resultant mesopores were at most 3 nm in size [39]. In contrast, our present method using nonionic block copolymers opens a useful route for wide control of pore sizes in mesoporous metal films. The self-assembly process of nonionic block copolymers with a neutral charge, unlike ionic surfactants, is not disturbed externally by a bias voltage to the substrate.

As shown in the TEM results (**Figure 6.5d, e**), a unique framework with high Pt crystallinity was formed, which can reasonably be explained by the following suggested mechanism. After starting the electrochemical deposition, the Pt species approaches the working electrode surface together with the surfactant micelles. As explained, the Pt species are entangled with the EO chains of the micelles and the primary cluster of metal atoms (Pt_0) is formed by the first reduction. Isotropic grain growth from the primary cluster continuously proceeds until the Pt nanoparticle becomes thermally stable (~ 3 nm). In general, the primary Pt cluster isotropically

grows into a sphere to minimize the surface energy of the Pt grain. Then, the growing grain dislodges both water molecules and EO regions in the micelles. The EO regions are slightly distorted and undergo a plastic deformation. At this stage, the grown nanoparticle is fitted and stabilized inside the EO regions. The highly magnified TEM image clearly shows that the crystallinity of Pt with fcc structure is extended coherently across several nanoparticles (**Figure 6.5d, e**). Therefore, as the Pt deposition proceeds, the second Pt nanoparticle should be formed from another nucleus generated on the external surface of the first Pt nanoparticle, retaining the single crystalline-like state. Based on the described mechanism, it is understood that the framework thicknesses in the obtained mesoporous Pt films are determined by the shell thicknesses of the hydrophilic EO regions in the micelles. In the case of Brij 58 (**Figure 6.2f**), very thin walls (around 3 nm) were formed. With an increase in the number of EO units in the surfactants, the thick EO shells could accommodate several nanoparticles, increasing the wall thicknesses up to 13 nm (**Figure 6.2b, d**).

The electrochemically active surface areas (ECSAs) of the mesoporous Pt films were obtained by integrating the charge associated with the adsorption/desorption of hydrogen atoms in cyclic voltammograms (CVs) scanned in 0.5 M sulfuric acid, whose traces were typical of Pt electrode surface (not shown). The mass-normalized ECSAs were $31 \text{ m}^2 \cdot \text{g}^{-1}$, $32 \text{ m}^2 \cdot \text{g}^{-1}$, and $43 \text{ m}^2 \cdot \text{g}^{-1}$ for the mesoporous Pt films deposited by

PEO₄₅₀₀-PPO₃₂₀₀-PEO₄₅₀₀, F127, and Brij 58, respectively. The ECSAs of the films deposited by Brij 58 were higher than those of the films deposited by pluronic F127 and PEO₄₅₀₀-PPO₃₂₀₀-PEO₄₅₀₀, revealing that the decreasing mesopore size and wall thickness increased the ECSAs of the mesoporous Pt films. The mesoporous Pt film prepared with Brij 58 showed higher ECSAs compared to commercially available Pt black (around 10–25 m²·g⁻¹) and mesoporous Pt analogues (between 17 and 23 m²·g⁻¹) prepared with LLC [22, 23]. Thus, by creating nanoarchitectures with high-density porous structures in the films, the ECSAs of the Pt films were enhanced and higher surface-to-volume ratios were realized. To investigate the thermal stability, the obtained mesoporous Pt films were annealed at various temperatures (100 °C, 150 °C, and 200 °C,) for 2 h. Even after the thermal treatments, the CV shapes did not change at all. The loss of specific surface areas was not confirmed, indicating good thermal stability of the mesoporous films.

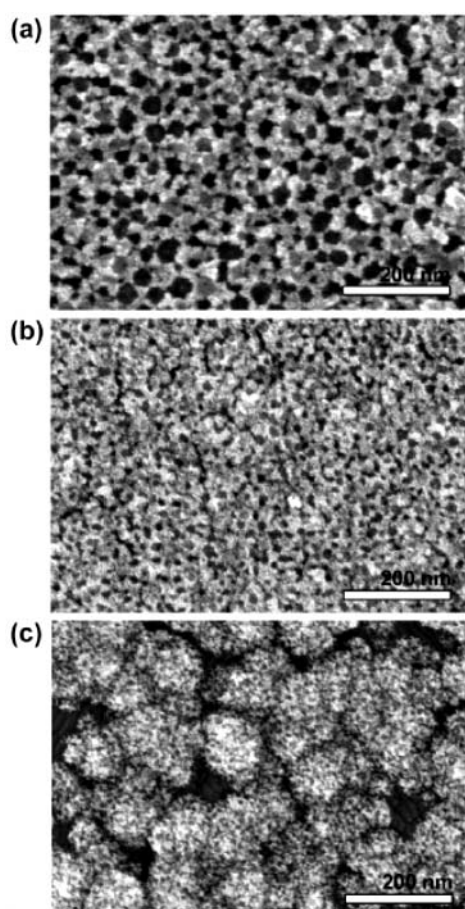


Figure 6.7 Typical SEM images of the mesoporous Pt films prepared (a) with PEO₄₅₀₀-PPO₃₂₀₀-PEO₄₅₀₀ + TIPBz, (b) with F127 + TIPBz, and (c) with Brij 58 + TIPBz. The observed mesopore sizes ranges from 22 nm to 51 nm (for (a) PEO₄₅₀₀-PPO₃₂₀₀-PEO₄₅₀₀ + TIPBz), from 12 nm to 25 nm (for (b) F127 + TIPBz), and from 11 nm to 14 nm (for (c) Brij 58 + TIPBz), respectively. The average mesopore sizes are 31 nm (for (a) PEO₄₅₀₀-PPO₃₂₀₀-PEO₄₅₀₀+ TIPBz), 18 nm (for (b) F127 + TIPBz), and 12 nm (for (c) Brij 58 + TIPBz), respectively.

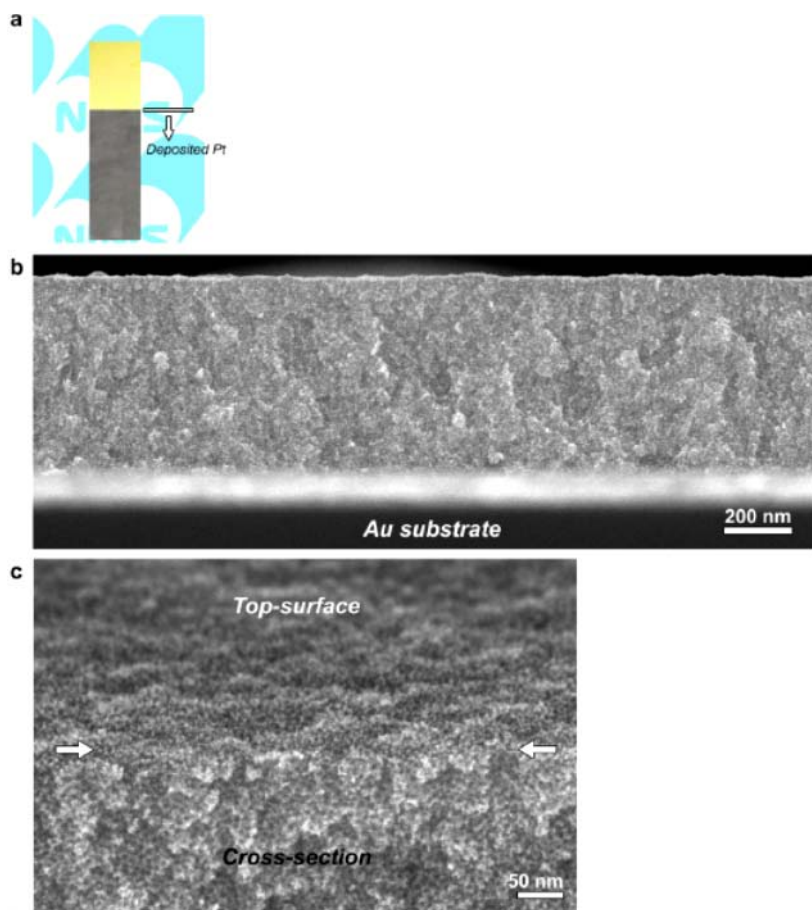


Figure 6.8 SEM images of the mesoporous Pt film prepared with Brij 58 on the Au substrate.

Note in Figure 6.8:

The Pt species was deposited uniformly on the substrates without any cracks or voids. In normal electrochemical plating, side reactions such as the evolution of gas sometimes occurs, which induces the occurrence of cracks in the film and the reduction of mesoporous ordering. In the present case, the use of low-potential deposition effectively prevented the generation of gas, forming the crack-free continuous Pt film.

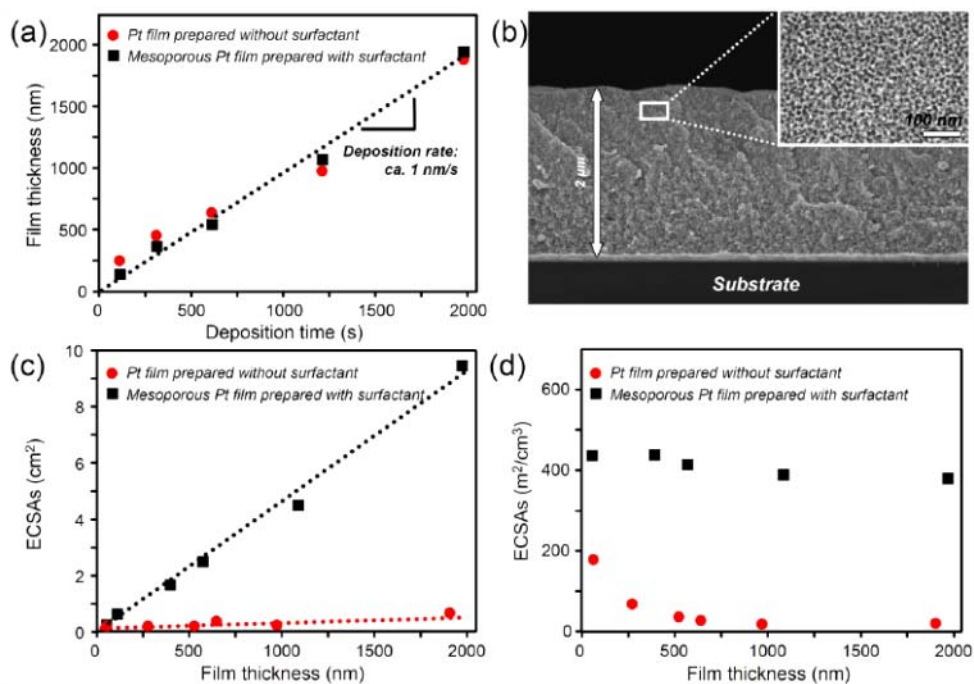


Figure 6.9 ECSAs of the mesoporous Pt films prepared with Brij 58 and without surfactant. (a) Relation between the film thicknesses and the applied deposition time. (b) Cross-sectional SEM image of the top-region in the thick mesoporous Pt film. (c) Relation between the total ECSAs and the film thicknesses. (d) Relation between the volume-normalized ECSAs and the film thicknesses.

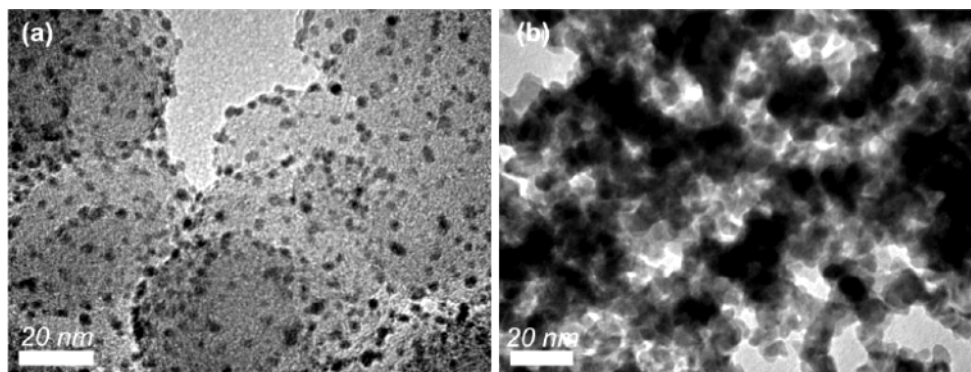


Figure 6.10 TEM image of (a) carbon-supported Pt black and (b) commercially available Pt black as references.

When the mesoporous Pt films were deposited on an Au substrate, the films had a flat surface due to good contact between the mesoporous Pt layer and the Au surface (**Figure 6.8**). Uniform mesopores were clearly observable on the cross-sectional image near the top-region in the thick film (**Figure 6.8b, c**). The relation between the film thicknesses and the deposition time are shown in **Figure 6.9a**. The film thicknesses in both mesoporous Pt and nonporous Pt films proportionally increased at deposition rate of $1 \text{ nm}\cdot\text{s}^{-1}$, but the total surface areas only for mesoporous Pt films proportionally increased (**Figure 6.9c**). The volume normalized ECSAs (per film volume, cm^3) of the mesoporous Pt film kept constant even after the deposition of thick mesoporous Pt layer (**Figure 6.9d**), but those of the nonporous Pt film gradually decreased (**Figure 6.9d**). This fact concludes that, by creating mesoporous structure, the inner parts of the Pt film can work as electrochemically active surface and the mesoporous structure was homogeneously formed inside the film (**Figure 6.9b**).

To investigate potentiality as a catalytic electrode, methanol electrochemical oxidation reaction on the mesoporous Pt film prepared with Brij 58 was examined and compared with five different kinds of samples: two mesoporous Pt analogues prepared with LLCs (Type I: diblock copolymer system [26], Type II: C_{16}EO_8 system [22]), Pt film without mesopores, and two commercially available Pt catalysts (carbon-supported Pt nanoparticles and unsupported Pt nanoparticles (i.e., Pt black), **Figure 6.10**. **Figure 6.11** and **6.12**, show the electrocatalytic performances recorded in an aqueous solution containing methanol. All the samples showed the two visible anodic peaks occurring on the positive and negative sweeps, which are typical features of the methanol oxidation process (**Figure 6.12b**). It is interesting that our mesoporous Pt film showed a remarkably large current for the electrocatalytic oxidation of methanol among all the samples (**Figure 6.11a**). In detail, the ECSA-normalized peak current of our mesoporous Pt film in the positive-direction sweep was several times larger than those of commercially available Pt catalysts (**Figure 6.11a**). Chronoamperometric curves recorded at 0.6 V (**Figure 6.11b**) indicated that the sufficiently high durability of the catalytic performance of the mesoporous Pt film.

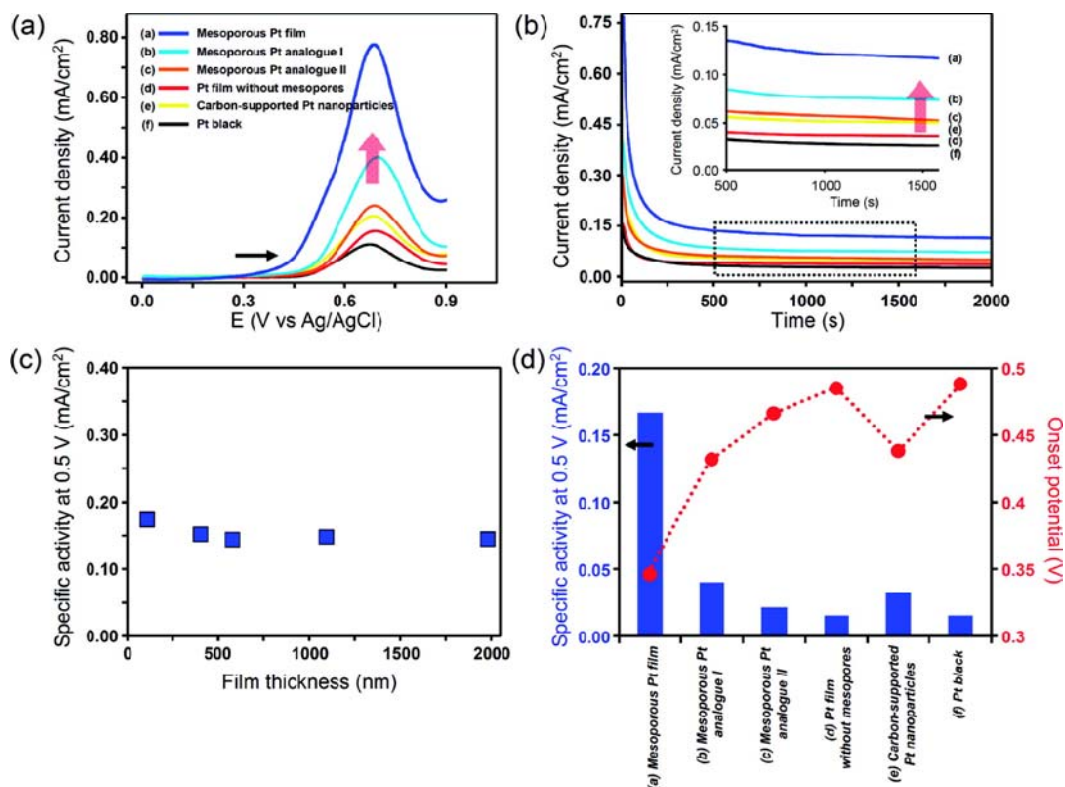


Figure 6.11 Demonstration of methanol oxidation activity of mesoporous Pt film prepared with Brij 58. (a) Cyclic voltammograms and (b) chronoamperometric curves at 0.6 V are measured in 0.5 M H₂SO₄ containing 1 M methanol. The currents are normalized by ECSAs obtained from CV curves in 0.5 M H₂SO₄ solution. Mesoporous Pt film prepared with Brij 58 is compared with mesoporous Pt analogues prepared from LLC (Type I: diblock copolymer. Type II: C₁₆EO₈), bulk Pt film deposited without surfactant, commercially available carbon-supported Pt nanoparticles, and Pt black. The bulk Pt film as a reference is prepared under the same electrochemical condition except for the absence of surfactant. All the film thicknesses for mesoporous Pt and mesoporous Pt analogues (I and II) are 100 nm. (c) Investigation of the effect of film thicknesses on the methanol oxidation performance. The relation between the film thicknesses and the specific activities at 0.5 V is examined. (d) Summary on the specific activities at 0.5 V and the onset potentials for all the samples.

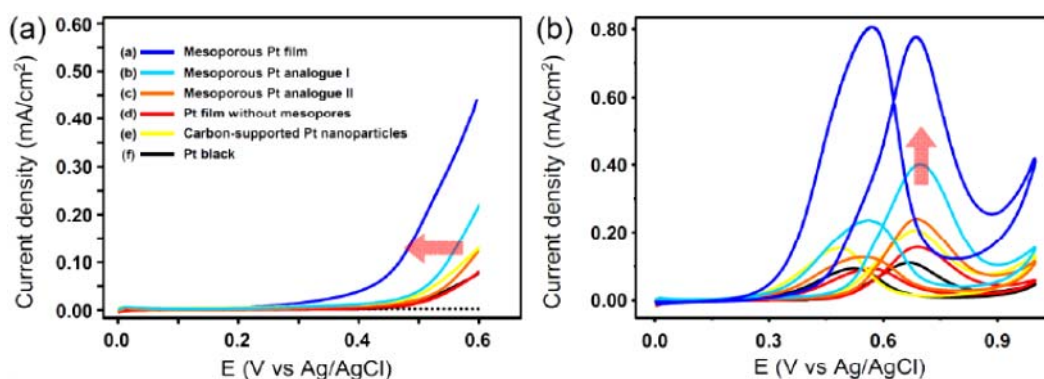


Figure 6.12 (a) Linear sweep voltammograms and (b) cyclic voltammograms measured in 0.5 M H_2SO_4 containing 1 M methanol. In both the figures, the currents are normalized by ECSAs obtained from CV curves in 0.5 M H_2SO_4 solution. The onset potentials are defined as the potentials at $10 \mu\text{A}\cdot\text{cm}^{-2}$ in (a) linear sweep voltammogram. Mesoporous Pt film prepared with Brig 58 is compared with mesoporous Pt analogues prepared from LLC (Type I: Diblock copolymer, Type II: C_{16}EO_8), bulk Pt film deposited without surfactant, commercially available carbon-supported Pt nanoparticles, and Pt black. The bulk Pt film as a reference is prepared under the same electrochemical condition except for the absence of surfactant. All the film thicknesses for mesoporous Pt and mesoporous Pt analogues (I and II) are fixed to be 100 nm.

Generally, three-dimensionally connected pores are known to make the entire surface readily accessible by reactants, because they have a small tortuosity factor [44]. Such porous materials have little diffusion resistance for reactants which have a mean free path shorter than the pore radius (e.g., liquid). In view of this, I introduced experimental results that indicate sufficiently fast reactant supply into the mesopores (**Figure 6.11c** and **Figure 6.13**). **Figure 6.11c** shows the relation between the film thicknesses and ECSA-normalized currents at 0.5 V where the electrochemical oxidation of methanol was dominant, as we can observe a linear relation in Tafel plots (**Figure 6.14**). Even when the film thicknesses increased up to 2 μm , the specific activities were almost constant. It is indicated that the methanol molecules can easily access all the inner mesopores without serious diffusion resistance. Further detailed discussion on this point is available in the Supporting Information (**Figure 6.13**).

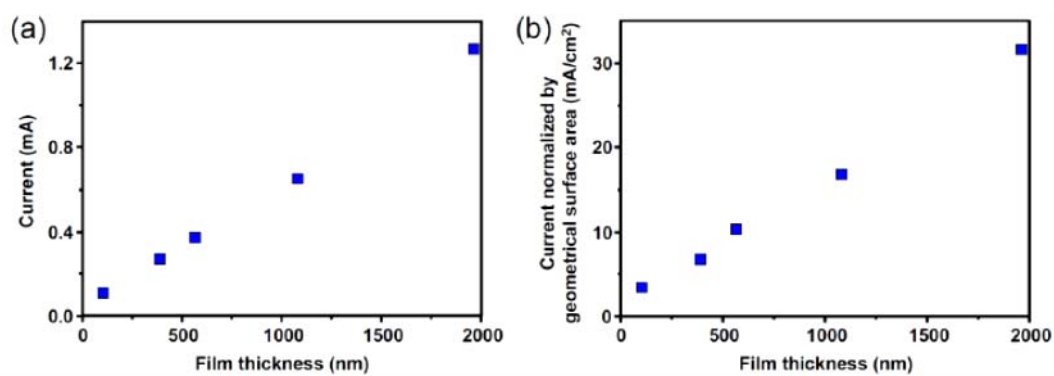


Figure 6.13 Investigation of methanol oxidation activity (measured in 0.5 M H₂SO₄ containing 1 M methanol) for mesoporous Pt films with different film thicknesses ranging from 100 nm to 2 μ m. (a) Relation between the film thicknesses and the catalytic currents (at 0.5 V in the positive-direction sweep). (b) Relation between the film thicknesses and catalytic currents (at 0.5 V in the positive-direction sweep) normalized by the geometric electrode surface areas.

Note in Figure 6.13:

Here I theoretically discuss the influence of mass transport in electrochemical reaction system. As shown in **Figures 6.11** and **6.13**, I experimentally proved that the diffusion effect inside the mesoporous film was negligible. The obtained result was consistent with a previous report that peak current of methanol oxidation reaction was not influenced by the mass transport effect [51]. Through the theoretical explanation, we can describe the diffusion limitation in our system. Two types of diffusion limitation should be considered.

Diffusion limitation I: From bulk solution to the outer surface of mesoporous Pt film

In order to resolve the concern about the influence of mass transport of methanol, we estimated limiting diffusion current density (based on geometrical surface area) as follows. The limiting diffusion current density, i_d , is calculated in accordance with the diffusion equation:

$$i_d = nFD_{\text{MeOH}}C_0/d$$

Where n is the electron number for net reaction, F is Faraday constant ($96480 \text{ C}\cdot\text{mol}^{-1}$), D_{MeOH} is the diffusion coefficient for methanol in water ($1.3 \times 10^{-5} \text{ cm}\cdot\text{s}^{-1}$), C_0 is the bulk concentration ($1 \times 10^{-5} \text{ mol}\cdot\text{cm}^{-3}$), and d is the thickness of diffusion layer ($\sim 0.04 \text{ cm}$). The d value is calculated from the parameters of oxygen reduction reaction ($i_d = 0.4 \text{ mA}\cdot\text{cm}^{-2}$, $n = 4$, $D = 2 \times 10^{-5} \text{ cm}\cdot\text{s}^{-1}$, $C = 2 \times 10^{-6} \text{ mol}\cdot\text{cm}^{-3}$) [49, 50].

From the above assumption, the i_d value of the methanol oxidation reaction at room temperature without stirring is expected to be $\sim 200 \text{ mA}\cdot\text{cm}^{-2}$. As seen in **Figure 6.13**, however, the current densities normalized by the geometrical electrode surface area were at most $30 \text{ mA}\cdot\text{cm}^{-2}$.

Diffusion limitation II: From the entrance of the mesoporous Pt film to the bottom of the film

The diffusion of methanol inside mesoporous materials is “molecular diffusion” in this case [51]. From the potential at which the concentration of methanol at the bottom part of the mesoporous Pt film, C_b , becomes very low, the influence of mass transport inside the mesoporous Pt film is thought to be apparent. The current density at $C_b = 0$ is defined as “ i_{d2} ” and the following equation can be obtained from a mass transport equation inside mesoporous electrode system (See the reference and the

boundary conditions are “concentration gradient and concentration at the surface of mesoporous film are 0 and C_{02} , respectively.”) [52].

$$i_{d2} = 2nFD_{\text{eff}}C_{02}/h$$

where D_{eff} is the effective diffusion coefficient ($= D_{\text{MeOH}}P / \tau$; P is porosity and τ is tortuosity factor), C_{02} is the concentration at the surface of mesoporous film, and h is the thickness of the film. By comparing the i_d value and i_{d2} value, we can obtain a relative value, X :

$$X = i_{d2} / i_d = 2(P / \tau) (d/h) (C_{02}/C_0)$$

$$\text{from } D_{\text{eff}} \nabla^2 C = -\frac{Si_{\text{ECSA}}}{nF}$$

where D_{eff} is the effective diffusion coefficient ($= D_{\text{MeOH}}P / \tau$; P is porosity and τ is tortuosity factor), C_{02} is the concentration at the surface of mesoporous film, S is the specific surface area, and h is the thickness of the film. For such three-dimensionally connected porous materials like our mesoporous Pt film, a relation between τ value and P value was reported by Levitz [52]. According to the report, even when P value is only 0.2 (actual value of our mesoporous Pt is probably larger), τ is found to be ~ 5 . Thus, for the thickest film we used in this work ($h = 2 \mu\text{m}$, see **Figure 6.11** and **6.13**), the limiting current inside the mesoporous film, i_{d2} , becomes $\sim 3 \text{ A}\cdot\text{cm}^{-2}$. This value is far larger than the current observed in this work.

Consequently, from the above theoretical calculation (I and II), the mass transport effect can be excluded in the present electrochemical measurements.

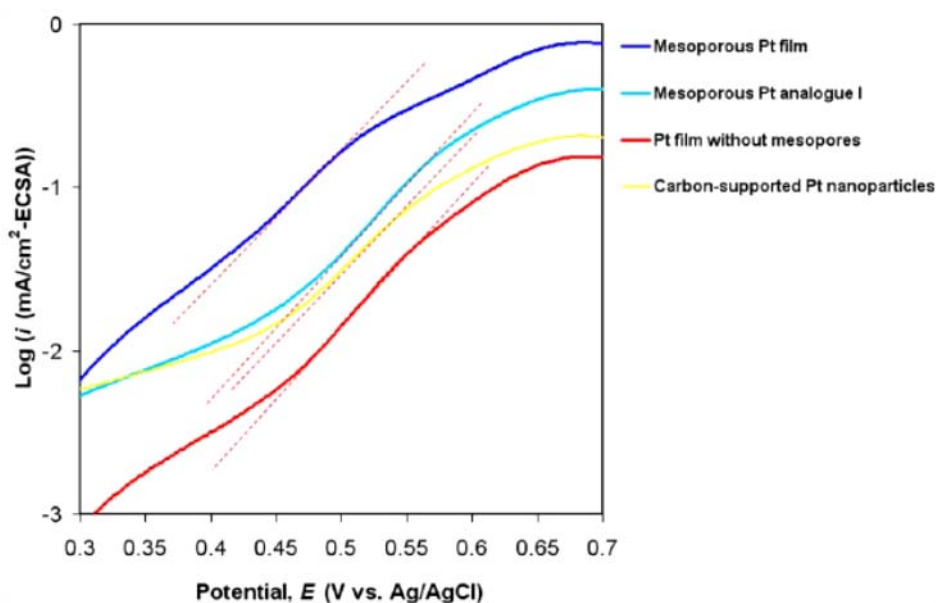


Figure 6.14 Tafel slopes for methanol electrooxidation reaction. Tafel slope for mesoporous Pt prepared with Brij 58 is compared with those for other typical Pt samples (Mesoporous Pt analogue I, Pt film without mesopores, and carbon-supported Pt nanoparticles). The Tafel slopes are measured to be 126 (for Mesoporous Pt film), 116 (Mesoporous Pt analogue I), 110 (Pt film without mesopores), 126 (Carbon-supported Pt nanoparticles), respectively.

Note in Figure 6.14:

The Tafel slopes of all the samples were almost constant (around $120 \text{ mV} \cdot \text{decade}^{-1}$), indicating the occurrence of the same rate-determining step for all the cases. This value is consistent with the result of non-steady state measurement of methanol oxidation reaction reported by Wieckowski *et al.*, who reported the rate-determining step was the C-H bond cleavage [53]. The concave structure of the mesoporous Pt film provided more active sites for the C-H bond cleavage reaction, showing the superior specific activity as displayed in **Figure 6.11**. The chronoamperometric measurement (**Figure 6.11b**) also revealed high durability, indicating the enhancement of adsorbed OH formation associated with water dissociation, which is requisite for the oxidation of CO intermediates in the electrochemical methanol oxidation reaction. Thus, our mesoporous Pt film can accelerate methanol oxidation reaction, due to abundant active sites for the dissociation of C-H bond of methanol molecules and O-H bond of water molecules.

Furthermore, I discussed the topological interest of our mesoporous Pt film on the basis of activity for methanol oxidation reaction. The specific activity of the mesoporous Pt at 0.5 V is found to be far larger than those of the other samples (**Figure 6d**). This is also supported by the ~ 100 mV more negative onset potential of the mesoporous Pt film (**Figure 6d** and Supporting Information, **Figure 6.12a**). Importantly, Tafel slope values for all the samples are the same, meaning that the rate-determining step of the reaction on the mesoporous Pt surface is thought to be the same as those of typical Pt catalysts (details are given in the Supporting Information, **Figure 6.14**). From these results, it can be understood that the enhanced activity observed here is attributable to the increase of active sites. Generally, defect sites and step edges enhance dissociation of water and methanol molecules [32, 33, 45-47]. As seen in **Figure 6.5**, the connected Pt nanoparticles with high crystallinity provide not only high surface area but also the rich atomic steps with concave surface topology, which probably enhanced cleavage of the C–H and O–H bonds in the methanol decomposition.

6.4. Conclusion

I proposed a new approach using diluted surfactant solutions for the preparation of Pt films with accessible pores and widely controlled the mesopore sizes by changing different surfactants and adding organic expanders. Nonionic PEO-PPO-PEO-type copolymers used in this study are good candidates as porogen of larger mesopores because of their low cost, commercial availability, and biodegradability. The present plating solutions can be reused several times, demonstrating high repeatability. The present process can allow easy preparation of other mesoporous Pt-based alloys, which will be important for realizing higher performance as electrodes in batteries.

References

- [1] A. Chen, and P. Holt-Hindle, *Chem. Rev.*, **110**, 3767 (2010).
- [2] Z. M. Peng, and H. Yang, *Nano Today*, **4**, 143 (2009).
- [3] T. Kijima, T. Yoshimura, M. Uota, T. Ikeda, D. Fujikawa, S. Mouri, and S. Uoyama, *Angew. Chem., Int. Ed.*, **43**, 228 (2004).
- [4] T. Kijima, Y. Nagatomo, H. Takemoto, M. Uota, D. Fujikawa, Y. Sekiya, T. Kishishita, M. Shimoda, T. Yoshimura, H. Kawasaki, and G. Sakai, *Adv. Funct. Mater.*, **19**, 545 (2009).
- [5] X. W. Teng, X. Y. Liang, S. Maksimuk, and H. Yang, *Small*, **2**, 249 (2006).
- [6] L. Wang, and Y. Yamauchi, *Chem. Mater.*, **21**, 3562 (2009).
- [7] J. Erlebacher, M. J. Aziz, A. Karma, N. Dimitrov, and K. Sieradzki, *Nature*, **410**, 450 (2001).
- [8] S. Tominaka, Y. Nakamura, and T. Osaka, *J. Power Sources*, **195**, 1054 (2010).
- [9] T. Yanagisawa, T. Shimizu, K. Kuroda, and C. Kato, *Bull. Chem. Soc. Jpn.*, **63**, 988 (1990).
- [10] T. Yanagisawa, T. Shimizu, K. Kuroda, and C. Kato, *Bull. Chem. Soc. Jpn.*, **63**, 1535 (1990).
- [11] C. T. Kresge, M. E. Leonowicz, W. J. Roth, J. C. Vartuli, and J. S. Beck, *Nature*, **359**, 710 (1992).
- [12] D. Y. Zhao, J. L. Feng, Q. S. Huo, N. Melosh, G. H. Fredrickson, B. F. Chmelka, and G. D. Stucky, *Science*, **279**, 548 (1998).
- [13] S. Inagaki, S. Guan, T. Ohsuna, O. Terasaki, *Nature*, **416**, 304 (2002).
- [14] P. D. Yang, D. Y. Zhao, D. I. Margolese, B. F. Chmelka, G. D. Stucky, *Nature*, **396**, 152 (1998).
- [15] S. H. Joo, S. J. Choi, I. Oh, J. Kwak, Z. Liu, O. Terasaki, and R. Ryoo, *Nature*, **412**, 169 (2001).
- [16] S. Che, Z. Liu, T. Ohsuna, K. Sakamoto, O. Terasaki, and T. Tatsumi, *Nature*, **429** 281 (2004).
- [17] M. Choi, K. Na, J. Kim, Y. Sakamoto, O. Terasaki, and R. Ryoo, *Nature*, **461**, 246 (2009).

- [18] S. Schacht, Q. Huo, I. G. Voigt-Martin, G. D. Stucky, and F. Schüth, *Science*, **273**, 768 (1996).
- [19] Y. F. Lu, R. Ganguli, C. A. Drewien, M. T. Anderson, C. J. Brinker, W. L. Gong, Y. X. Guo, H. Soyez, B. Dunn, M. H. Huang, and J. I. Zink, *Nature*, **389**, 364 (1997).
- [20] H. J. Shin, R. Ryoo, Z. Liu, and O. Terasaki, *J. Am. Chem. Soc.*, **123**, 1246 (2001).
- [21] Y. Kuroda, Y. Yamauchi, and K. Kuroda, *Chem. Commun.*, **46**, 1827 (2010).
- [22] G. S. Attard, P. N. Bartlett, N. R. B. Coleman, J. M. Elliott, J. R. Owen, and J. H. Wang, *Science*, **278**, 838 (1997).
- [23] G. S. Attard, C. G. Goltner, J. M. Corker, S. Henke, and R. H. Templer, *Angew. Chem., Int. Ed.*, **36**, 1315 (1997).
- [24] O. Celik, and O. Dag, *Angew. Chem., Int. Ed.*, **40**, 3799 (2001).
- [25] G. S. Attard, J. C. Glyde, and C. G. Goltner, *Nature*, **378**, 366 (1995).
- [26] A. Takai, Y. Yamauchi, and K. Kuroda, *J. Am. Chem. Soc.*, **132**, 208 (2010).
- [27] Y. Yamauchi, A. Sugiyama, R. Morimoto, A. Takai, and K. Kuroda, *Angew. Chem., Int. Ed.*, **47**, 5371 (2008).
- [28] G. Surendran, L. Ramos, B. Pansu, E. Prouzet, F. Audonnet, P. Beaunier, and H. Remita, *Chem. Mater.*, **19**, 5045 (2007).
- [29] S. C. Warren, L. C. Messina, L. S. Slaughter, M. Kamperman, Q. Zhou, S. M. Gruner, F. J. DiSalvo, and U. Wiesner, *Science*, **320**, 1748 (2008).
- [30] H. Arora, Z. Li, H. Sai, M. Kamperman, S. C. Warren, and U. Wiesner, *Macromol. Rapid Commun.*, **31**, 1960 (2010).
- [31] Y. Wan, and D. Y. Zhao, *Chem. Rev.*, **107**, 2821 (2007).
- [32] N. Tian, Z. Zhou, and S. Sun, *J. Phys. Chem. C*, **112**, 19801 (2008).
- [33] Z. Zhou, Z. Huang, D. Chen, Q. Wang, N. Tian, and S. Sun, *Angew. Chem., Int. Ed.*, **49**, 411 (2010).
- [34] T. Sakai, and P. Alexandridis, *J. Phys. Chem. C*, **109**, 7766 (2005).
- [35] T. Sakai, and P. Alexandridis, *Langmuir*, **20**, 8426 (2004).

- [36] O. Glatter, and O. Kratky, (Academic, London, 1982).
- [37] O. Glatter, *J. Appl. Crystallogr.*, **10**, 415 (1977).
- [38] O. Glatter, *Acta Phys. Austriaca.*, **47**, 83 (1977).
- [39] K. S. Choi, E. W. McFarland, and G. D. Stucky, *Adv. Mater.*, **15**, 2018 (2003).
- [40] K. S. Choi, E. W. McFarland, and G. D. Stucky, *U.S. Patent*, No. 0016646 (2004).
- [41] K. S. Choi, H. C. Lichtenegger, G. D. Stucky, and E. W. McFarland, *J. Am. Chem. Soc.*, **124**, 12402 (2002).
- [42] S. Manne, J. P. Cleveland, H. E. Gaub, G. D. Stucky, P. K. Hansma, *Langmuir*, **10** 4409 (1994).
- [43] E. J. Wanless, and W. A. Ducker, *J. Phys. Chem.*, **100**, 3207 (1996).
- [44] P. Levitz, *Adv. Colloid Interface Sci.*, **76**, 71 (1998).
- [45] S. W. Lee, S. Chen, W. Sheng, N. Yabuuchi, Y. T. Kim, T. Mitani, E. Vescovo, and Y. Shao-Horn, *J. Am. Chem. Soc.*, **131**, 15669 (2009).
- [46] S. W. Lee, S. Chen, J. Suntivich, K. Sasaki, R. R. Adzic, and Y. Shao-Horn, *J. Phys. Chem. Lett.*, **1**, 1316 (2010).
- [47] N. Tian, Z. Zhou, S. Sun, Y. Ding, and Z. Wang, *Science*, **316**, 732 (2007).
- [48] F. Seland, R. Tunold, and D. A. Harrington, *Electrochim. Acta.*, **55**, 3384 (2010).
- [49] S. Tominaka, S. Ohta, H. Obata, T. Momma, and T. Osaka, *J. Am. Chem. Soc.* **130**, 10456 (2008).
- [50] S. Tominaka, T. Momma, and T. Osaka, *Electrochim. Acta.*, **53**, 4679 (2008).
- [51] S. Tominaka, S. Ohta, T. Osaka, and R. Alkire, *Energy Environ. Sci.*, **4**, 162 (2011).
- [52] P. Levitz, *Adv. Colloid Interface Sci.*, **76-77**, 71 (1998).
- [53] E. Herrero, K. Franaszczuk, and A. Wieckowski, *J. Phys. Chem.*, **98**, 5074 (1994).

Chapter 7

Synthesis of Mesoporous Pt-Pd Alloy Films by Electrochemical Plating in Aqueous Surfactant Solutions

7.1. Introduction

The development of bimetallic materials has attracted a lot of attention because of their attractive performance on catalytic reforming, fuel cell electrocatalysis, hydrodesulphurization, and partial alkene oxidation [1]. Precious metals such as platinum and their alloys represent some of the most efficient catalysts used in fuel-cell technology, hydrogenation reaction, and the development of sensors and nanodevices [2-4]. In comparison with other bimetallic systems, the combination of platinum and palladium is particularly advantageous in catalysts used for hydroisomerization, hydrocracking, hydrogenation, and hydrotreatment [5]. For example, a bimetallic catalyst containing platinum and palladium supported on alumina has been demonstrated to improve sulfur resistance on alumina in a diesel hydrotreating process, compared to a platinum monometallic catalyst.

Compared with traditional bimetallic materials, nanostructured bimetallic materials have more advantages, due to their higher surface area and excellent reaction activity. Meso/nanoporous bimetallic materials have been widely studied for applications in fuel cells, sensors, batteries, and electrochemical supercapacitors [6-8]. Catalytic processes are highly dependent on surface areas and their crystal structures. The nanostructured metals have been used in a variety of industrial processes. In particular, forming bimetallic systems through the addition of a second metal provides a method for tailoring catalytic activity and selectivity through cooperative effects. Although many approaches are being reported for the preparation of metal oxides-, metal sulfides-, and carbon-based supported catalysts [9], the unsupported metallic catalysts are still a hot research topic.

Previous synthesis of ordered mesoporous metals have been synthesized based on the concept of direct replication from templates. Most of the mesoporous metals have been prepared by using mesoporous silicas as hard templates [10-12]. Recently, ordered lyotropic liquid crystalline phases with very high surfactant concentrations [13-15] have been utilized as soft-templates. In this process, by taking the phase diagram of the surfactant/metal salts/water system into consideration, the final mesostructures can be

controlled by changing surfactant sizes and concentrations. Currently, the variations of possible mesostructures are expanding to include lamellar and 3D cage-type as well as 2D hexagonal mesostructures through the use of block copolymers or the addition of expanders into liquid crystal systems [16-18]. Very recently, it was reported that the self-assembly of block copolymers with ligand-stabilized platinum nanoparticles provided access to orderly arranged mesostructures [19-21]. Despite considerable progress with mesoporous metals, however, the synthetic process is still very complex, and the controllability of the framework compositions in mesoporous metals is much more limited compared to that in other mesoporous materials (such as silica- and carbon-based compositions).

The morphology of mesoporous metals has great significance for practical applications. Compared with fibers and tubes, metallic films with meso/nanoporous structure are very useful for battery applications, because they can be directly used as electrodes. For synthesis of meso/nanoporous alloy films, there are increasing number of reports about various approaches, such as the coimpregnation method [22], microemulsions [23], spray pyrolysis [24], and microwave irradiation [25]. With the development of micro-electrochemical devices including on-chip fuel cells and micro-batteries, electrochemical plating has been currently used to prepare porous electrodes and selectively deposit metals or alloys onto tiny current collectors [26, 27].

In this chapter, I extend this synthetic concept to alloy system such as Pt-Pd alloy. By tuning the composition ratios of Pt and Pd in precursor solutions, I successfully synthesized various mesoporous Pt_x-Pd_y alloy films with different compositions (x and y mean the atomic ratios of Pt and Pd in the products, respectively.). The pore walls in the obtained mesoporous Pt-Pd films were consisting of the connected nanoparticles (at around 3 nm in diameter). Such connection of nanoparticles can provide the high surface areas. Thanks to high surface areas and alloying with Pd, mesoporous Pt-Pd film showed distinctly enhanced electrocatalytic activity for methanol oxidation reaction, compared to commercially available Pt black catalyst.

7.2. Experimental Process

7.2.1. Electrodeposition of mesoporous Pt-Pd alloy films

According to our previous report [28], mesoporous Pt-Pd films were electrochemically synthesized by using electrochemical machine (CHI 842B electrochemical analyzer, CHI Instrument, U.S.) with a standard three-electrode cell system, including an Ag/AgCl (saturated KCl) electrode as the reference electrode, a platinum wire as the counter-electrode, and a working electrode. The working electrode included a gold-coating silicon substrate. The precursor solution was consisting of Brij 58 ($C_{16}H_{33}(OCH_2CH_2)_{20}OH$) (polyethylene glycol hexadecyl ether, Sigma) and Pt-Pd aqueous precursors. The concentration of Brij 58 was fixed to be 1.0 wt%. K_2PtCl_4 and Na_2PdCl_4 were purchased from Nacalai Tesque, Inc. and used as the metal sources. The total molar amount of Pt and Pd in the precursor solutions was fixed to be 20 mM. Their molar ratios were gradually changed (Pt : Pd = 100 : 0, 88 : 12, 75 : 25, 63 : 37, 50 : 50, 25 : 75, 0 : 100) for the preparation of various mesoporous Pt_x-Pd_y alloy films with different compositions (x and y mean the atomic ratios of Pt and Pd in the deposited films, respectively.). The mesoporous Pt-Pd alloy films were deposited at a constant potential of -0.2 V for 10 min without stirring at room temperature. After the deposition, as-prepared films were placed in ethanol for 12 h to extract the surfactants and then were thoroughly rinsed with deionized water and dried in air for further characterization. The carbon content in the films was less than 1.0 wt%, indicating that the majority of surfactants could be removed by thoroughly washing with ethanol and water.

7.2.2. Characterization

Scanning electron microscope (SEM) images were obtained by a Hitachi S-4800 microscope. The accelerating voltage was 10 kV. Transmission electron microscopy (TEM) was carried out using a JEOL JEM-2100F using an accelerating voltage at 200 kV. Low-angle XRD patterns were recorded by a Rigaku NANO-Viewer (Cu $K\alpha$ radiation) with the camera length = 700 mm operated at 40 kV and 30 mA. XPS analysis was carried out to conclusively investigate the electronic states of the surface of

the mesoporous Pt-Pd alloys. XPS spectra were taken at room temperature using a JPS-9010TR (JEOL) instrument with an Mg K α X-ray source. All binding energies were calibrated by referencing C 1s (285.0 eV). Cyclic voltammograms and chronoamperometric experiments were performed by using a CHI 842B electrochemical analyzer (CHI Instruments Inc., Austin TX). A conventional three-electrode cell was used, including an Ag/AgCl electrode as the reference electrode, a Pt wire as the counter electrode, and a working electrode. For mesoporous Pt film and mesoporous Pt-Pd films samples, the working electrode were the coating-gold silicon substrate with mesoporous films. For measurement of commercial Pt-black, the working electrode was prepared by depositing 3.0 μ L Pt-black aqueous solution (2.0 mg \cdot mL $^{-1}$) on a glassy carbon electrode (GCE, 3mm in diameter). Then, 3.0 μ L of Nafion (0.2 wt %) was coated on the surface of the modified GCE and dried before the electrochemical experiments. Methanol electrocatalytic oxidation (MOR) measurements were carried out in 0.5 M H $_2$ SO $_4$ solution containing 0.5 M methanol. The scan rate was 50 mV \cdot s $^{-1}$. In the electrocatalytic investigation, mass current densities were normalized by the loaded-Pt and Pt-Pd amounts, respectively. The loaded-Pt and Pt-Pd amounts were calculated by using inductively coupled plasma-mass spectroscopy (ICP-MS).

7.3. Result and Discussion

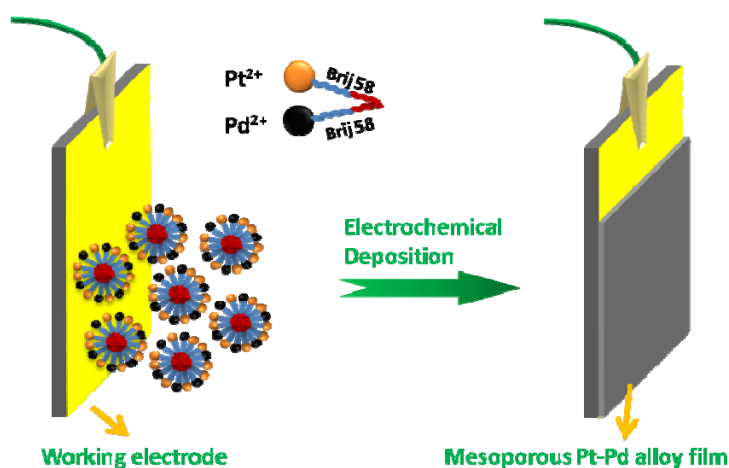


Figure 7.1 Schematic illustration of synthetic concept of mesoporous Pt-Pd alloy films. The surfactant (Brij 58) concentration is 1.0 wt%.

The schematic presentation of our synthetic concept of mesoporous Pt-Pd alloy films is shown in **Figure 7.1**. Mesoporous Pt-Pd alloy films were electrodeposited from an aqueous solution including K_2PtCl_4 and Na_2PdCl_4 with nonionic surfactant Brij 58. The surfactant concentration of Brij 58 in the plating solutions was set to be 1.0 wt%, which was above the critical micelle concentration (CMC) of the Brij 58 surfactant. The surface morphologies of mesoporous Pt_x-Pd_y alloy films with different compositions were observed by scanning electron microscopy (SEM), as is shown in **Figure 7.2** (x and y mean the atomic ratios of Pt and Pd in the products, respectively). After the electrochemical deposition for 10 min, Pt-Pd alloy films were deposited on the substrates uniformly. **Figure 7.2h** shows the relationship between the product compositions and the precursor compositions (The product compositions were measured by ICP analysis.). With the increase of Pd content in the precursor solutions, the Pd content in the products was linearly increased. By tuning the composition ratios of Pt

and Pd in precursor solutions, we successfully synthesized various mesoporous Pt_x-Pd_y alloy films with different compositions.

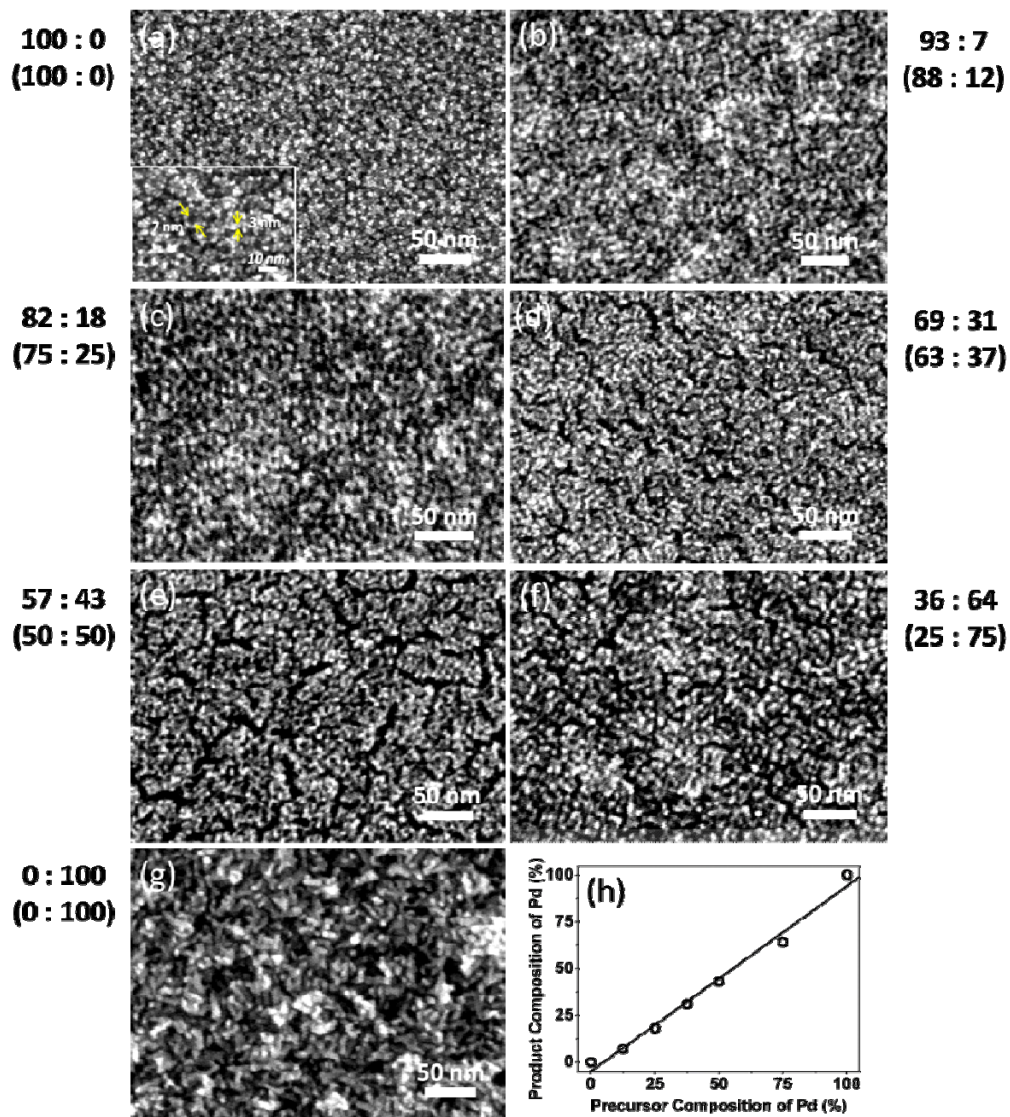


Figure 7.2 SEM images of mesoporous Pt_x-Pd_y alloy films with different compositional ratios. The product compositions of Pt : Pd in the films are noted. The corresponding compositional ratios of the precursor solutions are also noted in parentheses. (h) Relationship between the product compositions and the precursor compositions.

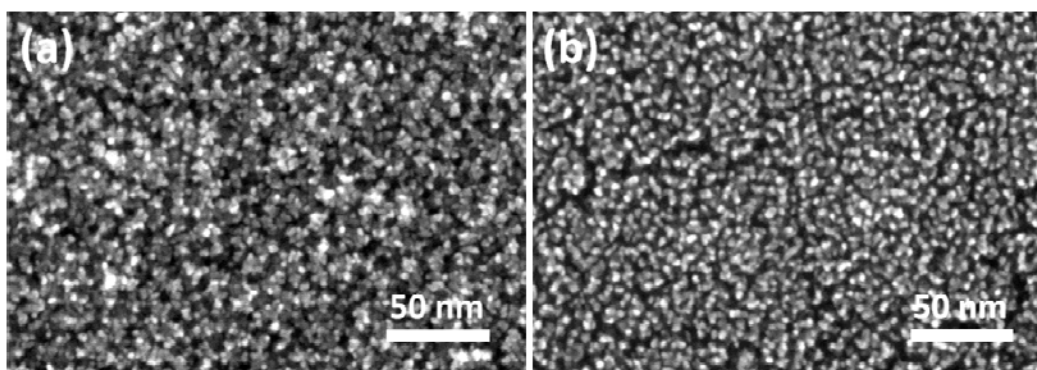


Figure 7.3 High resolution SEM images of mesoporous Pt and Pt₅₇-Pd₄₃ alloy films.

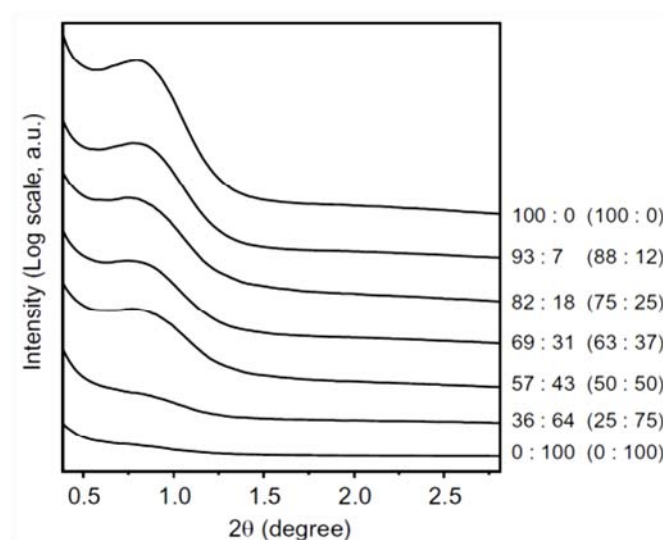


Figure 7.4 Low-angle XRD patterns of mesoporous Pt_x-Pd_y alloy films with different compositional ratios. The product compositions of Pt : Pd in the films are noted. The corresponding compositional ratios of the precursor solutions are also noted in parentheses.

Highly magnified SEM imaged clearly revealed the presence of mesopores. As seen in **Figure 7.3a**, the mesopore size and the wall thickness were roughly estimated to be 7 nm and 3 nm, respectively. The framework in all the films was composed of the connected nanoparticles, with an average size of around 3 nm (**Figure 7.2a** and **7.3**).

When the amounts of Pd species in the precursor solutions were increased, the cracks in the films were more obvious and the surfaces of the alloy films became uneven (**Figure 7.2**). When the precursor did not include Pt species, the Pd was grown as branches and no any mesopores were confirmed in the film.

To further investigate the mesostructural periodicity for all the films, low-angle XRD measurement was conducted, as shown in **Figure 7.4**. Almost the films with low Pd content showed notable peaks. The *d*-spacing was around 10 nm, which indicated the distance between the centers of two adjacent pores. With the increase of Pd content, the peak-tops slightly moved to higher angle region. Also, the peak intensities decreased gradually and became widen. It was proved that the mesostructural orderings were gradually decreased, which is well consistent with SEM result (**Figure 7.2**). The surface areas of all the mesoporous films were measured by nitrogen adsorption-desorption isotherms. The BET surface area of mesoporous Pt film was $43 \text{ m}^2 \cdot \text{g}^{-1}$. The BET surface areas of mesoporous Pt-Pd alloy films were also similar values which ranged from $40 \text{ m}^2 \cdot \text{g}^{-1}$ to $45 \text{ m}^2 \cdot \text{g}^{-1}$. Thus, our mesoporous films showed higher surface areas compared to commercially available Pt black (around $10\text{-}25 \text{ m}^2 \cdot \text{g}^{-1}$).

To understand the formation mechanism, I have changed the concentration of the dissolved surfactant (Brij 58), shown as **Figure 7.5**. When deposited without surfactant (**Figure 7.5a**), any pore structures did not appear in the obtained film. Also, when the Brij 58 concentration was below CMC, we could not observe any pore structures (**Figure 7.5b**). In contrast, when the Brij 58 concentration was over CMC, many spherical mesopores were formed in the films (**Figure 7.5c**). A similar situation was observed in our previous work on preparation of mesoporous Pt films with F127 system.[15] Based on these results, we can suppose that mesoporous Pt-Pd films are electrodeposited by the assembly of surfactant micelles with metal species. In the plating solution, dissolved metal ions are coordinated by water molecules to form metal-aqua complexes. Since the coordinated water molecules usually interact with ethylene oxide (EO) groups of the surfactant micelles, the dissolved Pt and Pd ions adsorb inside the external EO region of the surfactant micelles. Therefore, during the electrochemical deposition, the metal species are thought to move to the working electrode together with the surfactant micelles. Thus, the surfactant micelles can act as structural directing agents.

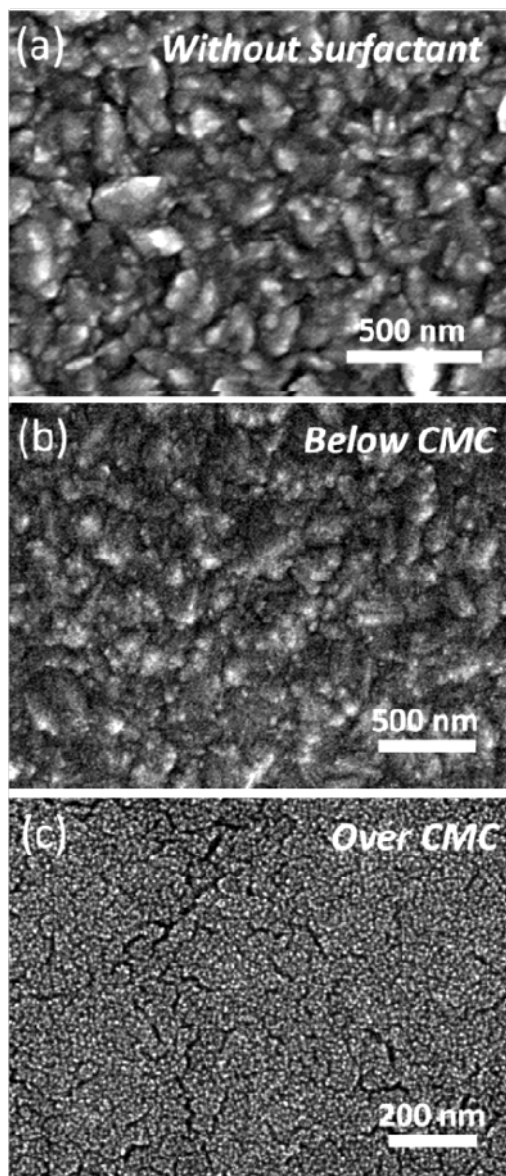


Figure 7.5 SEM images of $\text{Pt}_{57}\text{Pd}_{43}$ alloy films prepared (a) without Brij 58 and with Brij 58 whose concentration was (b) below CMC and (c) over CMC.

Figure 7.6a shows bright-field TEM image of mesoporous $\text{Pt}_{57}\text{Pd}_{43}$ alloy film (prepared from Pt : Pd = 50 : 50). This image was taken from the edge part of the obtained alloy film. It was difficult to clearly observe mesoporous structure over the large area of the film, because of the large film thickness. To make it clearer, I took a dark-field TEM image (**Figure 7.6b**). From the dark-field TEM image, it was clearly observed that the mesopores with uniform pore size about 7 nm were densely packed

each other and the mesopores were formed over the entire film. The elemental mapping images of Pt and Pd are shown in **Figure 7.6c-e**. The elemental mapping of Pt completely correspond to that of Pd, meaning that the Pt and Pd atoms were well-dispersed within the film without any phase segregation on a nanometer scale. The wide-angle XRD patterns for all the films with different compositions showed several intense peaks assignable to *fcc* structures. With the increase of the Pd contents, the high index peaks (*e.g.*, (311) peaks) were shifted very slightly to lower angle range, due to the difference of atomic size between Pt and Pd. However, unlike other alloy system (*e.g.*, Pt-Ni and Pt-Au alloys), it was very difficult to quantitatively discuss the gradual change of the peak positions based on Vegard's law, because of the fact that the lattice mismatch ratio was 0.77% for Pt/Pd.

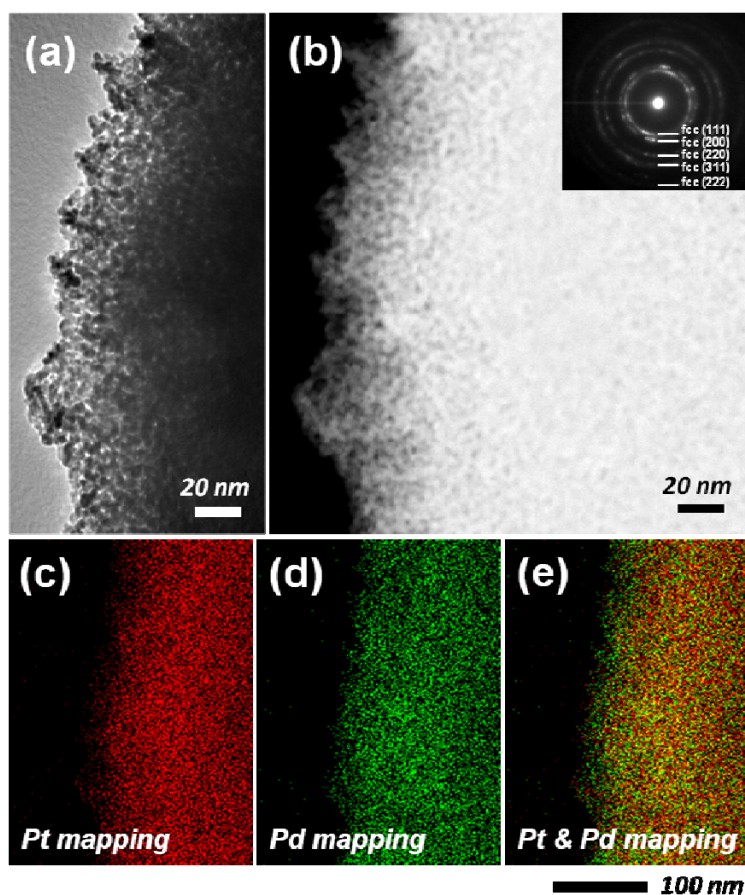


Figure 7.6 (a) Bright-field TEM image and (b) the corresponding dark-field TEM image of mesoporous Pt₅₇Pd₄₃ alloy film. (c, d, and e) Elemental mapping images of mesoporous Pt₅₇-Pd₄₃ alloy film.

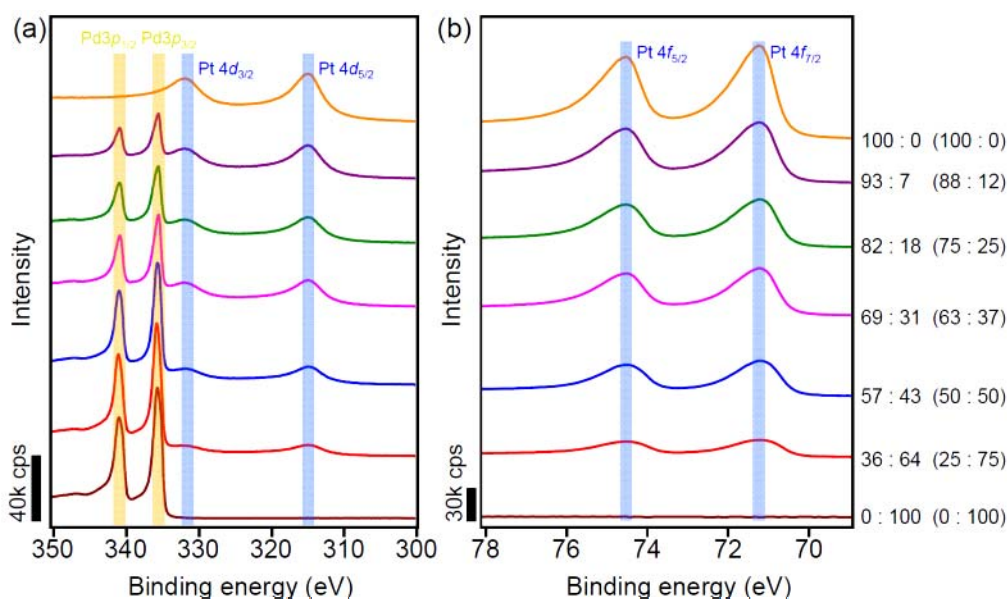


Figure 7.7 XPS spectra of mesoporous Pt_x-Pd_y alloy films with different compositional ratios. The product compositions of Pt : Pd in the films are noted. The corresponding compositional ratios of the precursor solutions are also noted in parentheses.

The surface compositions and electronic structure of all the films were characterized by XPS analysis. **Figure 7.7a** shows XPS spectra in the binding energy range from 300 eV to 350 eV. The Pd $3p_{1/2}$ (335.4 eV) and Pd $3p_{3/2}$ (340.7 eV) peaks as well as the Pt $4d_{3/2}$ (332.0 eV) and Pt $4d_{5/2}$ (314.8 eV) peaks were observed. The binding energy values for the Pd $3p$ peaks corresponded to those of Pd^0 , meaning almost all the Pd content in the films were not oxidized. Regarding the electronic states of Pt, the XPS spectra were further measured in the energy region from 69 eV to 78 eV (**Figure 7.7b**). The Pt $4f$ region presents the Pt $4f_{7/2}$ and Pt $4f_{5/2}$ peaks at 71.2 and 74.3 eV, respectively. These binding energies corresponded to that of Pt^0 . From the XPS results, with the increase of Pd content in the films, the intensity of Pd peaks was increased gradually, while the intensity of Pt peaks was decreased gradually. The surface compositions calculated by XPS data totally coincided with the product compositions characterized by ICP analysis (**Figure 7.2h**).

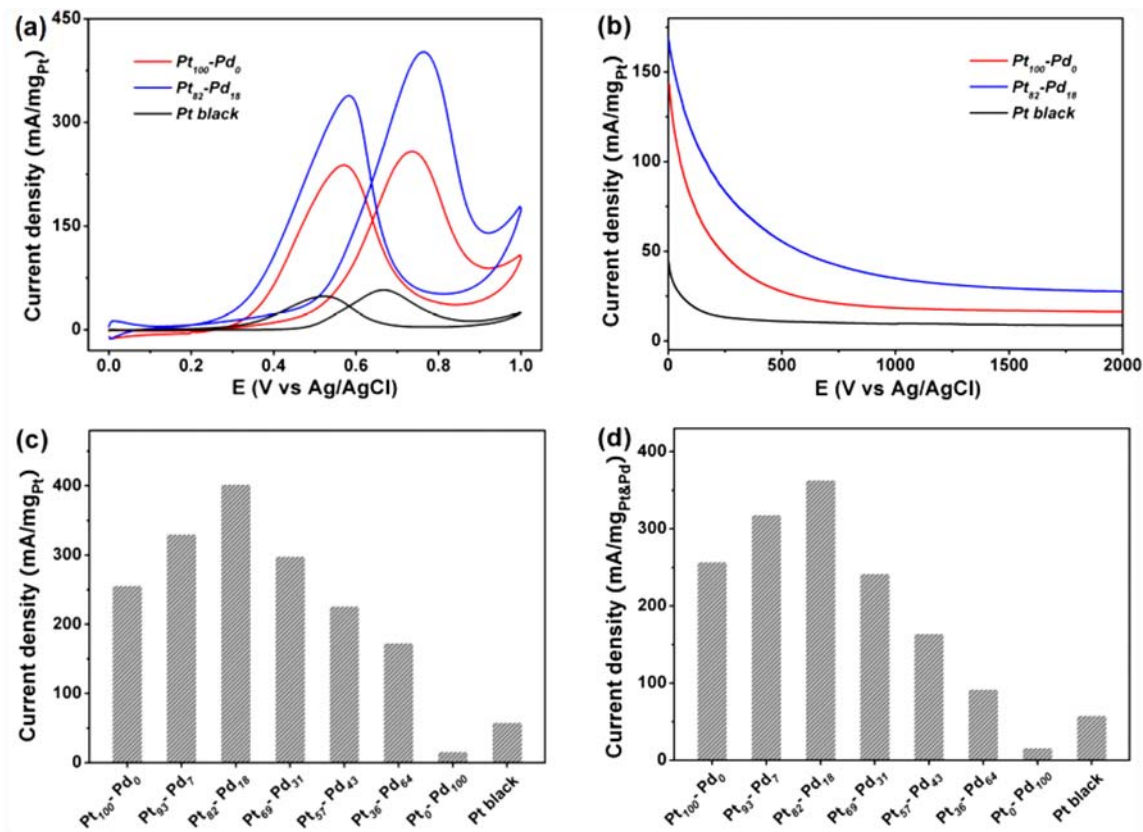


Figure 7.8 Demonstration of methanol oxidation activity of mesoporous Pt_x-Pd_y alloy films with different compositional ratios in 0.5 M H_2SO_4 containing 0.5 M CH_3OH . The product compositions of Pt : Pd in the films are noted. Pt-black is used as a reference sample. (a) Cyclic voltammogram for mesoporous Pt, mesoporous $Pt_{82}Pd_{18}$ alloy film, and Pt black, respectively. The current densities in Y-axis are normalized by the loaded Pt amounts in the films. (b) Pt mass-normalized chronoamperograms for methanol oxidation, which are recorded at 0.6 V. (c) Pt mass-normalized methanol oxidation activity for all the samples in 0.5 M H_2SO_4 and 0.5 M CH_3OH solution. (d) Pt-Pd mass-normalized methanol oxidation activity for all the samples in 0.5 M H_2SO_4 and 0.5 M CH_3OH solution. The current densities are normalized by the loaded Pt-Pd amounts in the films.

The electrocatalytic performance of the mesoporous Pt_x-Pd_y alloy films toward methanol oxidation was evaluated by cyclic voltammetry in a 0.5 M H_2SO_4 aqueous solution containing 0.5 M CH_3OH at room temperature (**Figure 7.8**). The two visible anodic peaks, occurring on the positive and negative sweeps, are typical features of the methanol oxidation process (**Figure 7.8a**). The catalytic current densities for all the

samples were normalized by the mass of Pt. Notably, mesoporous Pt-Pd alloys films showed higher mass catalytic activities for methanol oxidation reaction than the catalytic activities of commercially available Pt black catalyst (**Figure 7.8a**). Onset potential of methanol oxidation reaction is also an important parameter to evaluate the catalytic activity at low potentials for electrocatalysts. It was clearly observed that mesoporous films showed obviously negative shifted onset potential than that of commercially available Pt black catalyst. This is a further evidence for the enhanced activity of our mesoporous films for methanol dehydrogenation. Chronoamperometric curves recorded at 0.6 V for 2000 s (**Figure 7.8b**) indicated that the current density of the mesoporous Pt₈₂Pd₁₈ was the highest in the entire time range among other films, indicating a good stability of catalytic performance.

According to bimetallic Pt-Pd catalytic mechanism of methanol oxidation reaction, the first step is the adsorption of (CH₃OH)_{gas} on the Pt active sites to form (CH₃OH)_{ads}. The presence of Pd is benefit for decreasing the energy of methanol adsorption that provides favorable conditions for the further dehydrogenation of methanol to (CO)_{ads}. For pure Pt catalyst, CO is the thermodynamic sink, and CO can actively poison the surface of Pt. The Pd sites provide an oxygenated surface species by dissociating water at lower potential, in comparison with the pure Pt sites. Therefore, the surface hydroxides (OH)_{ads} are more readily formed in the presence of Pd sites, which can facilitate oxidative recombination of OH and CO to form (COOH)_{ads}. This is an important intermediate in the oxidation step for methanol oxidation system. The formation of (COOH)_{ads} leads to the accelerated CO₂ formation and decrease in the CO poisoning. Thus, the poisoning effect of CO_{ads} is efficiently reduced due to the synergic effect of Pt and Pd in the matrix.

Actually, all the mesoporous Pt and Pt-Pd alloy films showed higher electrocatalytic activities than commercial Pt black. Compared with mesoporous Pt film, the electrocatalytic activity of mesoporous Pt₉₃Pd₇ and Pt₈₂Pd₁₈ were increased by 30 % and 60 %, respectively (**Figure 7.8c**). It indicates that the co-existence of surface Pd and Pt sites are benefit for reducing the electrode poisoning by adsorbed CO species and improving the performance of methanol oxidation reaction [29-30]. With the increase of Pd atomic ratio (up to 18 %), more bimetallic sites could be formed, and that is the reason for Pt₈₂Pd₁₈ showing the higher catalytic activity. However, with the Pd atomic

ratio further increased, the activities of Pt₆₉Pd₃₁ and Pt₅₇Pd₄₃ decreased. That can be mainly ascribed to serious reduction of the mesostructural orderings in the films. In the case of mesoporous Pt film with orderly arranged mesopores, a large number of atomic steps in the mesopore walls consisting of Pt nanoparticles (with around 3 nm in diameter) provides favorable conditions for rapid methanol oxidation reaction [28]. However, with the increase of Pd content (Especially, the Pd atom ratio was over 30 %), the mesostructural orderings were seriously decreased (**Figures 7.2** and **7.4**). Therefore, the electrocatalytic activities of Pt₅₇Pd₄₃ and Pt₃₆Pd₆₄ showed lower than that of mesoporous Pt. Consequently, it can be concluded that the orderly arranged mesopores and the Pt-Pd bimetallic sites are two important factors for improving the electrocatalytic activity.

7.4. Conclusion

I successfully synthesized mesoporous Pt-Pd alloy films with different compositions by a facile electrochemical method using diluted precursor solutions with Brij 58 surfactant. Tunable controls of Pt and Pd ratios in the products were realized by changing the compositional ratios of Pt and Pd in the used precursor solutions. Due to high effective surface areas, the obtained Pt-Pd alloy films showed remarkably high catalytic activities for methanol oxidation reaction. This experimental data is a just preliminary example to confirm the superiority of mesoporous alloys and their potentials in electrocatalytic fields. In future, by further controlling the precursor compositions, we can realize many mesoporous alloy films with various compositions. We are trying to explore their novel functionalities in various fields, including electrochemical catalysis, heterogeneous catalysis, and semi-homogeneous catalysis.

References

- [1] G. W. Huber, J. W. Shabaker, and J. A. Dumesic, *Science*, **300**, 2075 (2003).
- [2] K. Koczkur, Q. Yi, and A. Chen, *Adv. Mater.*, **19**, 2648 (2007).
- [3] C. Bock, C. Paquet, M. Couillard, G. A. Botton, and B. R. MacDougall, *J. Am. Chem. Soc.*, **126**, 8028 (2004).
- [4] X. Teng, S. Maksimuk, S. Frommer, and H. Yang, *Chem. Mater.*, **19**, 36 (2007).
- [5] A. X. Yin, X. Q. Min, Y. W. Zhang, and C. H. Yan, *J. Am. Chem. Soc.*, **133**, 3816 (2011).
- [6] L. Wang, and Y. Yamauchi, *Chem. Asian J.*, **5**, 2493 (2010).
- [7] S. A. G. Evans, J. M. Elliott, L. M. Andrews, P. N. Bartlett, P. J. Doyle, and G. Denuault, *Analy. Chem.*, **74**, 1322 (2002).
- [8] P. A. Nelson, J. M. Elliott, G. S. Attard, and J. R. Owen, *Chem. Mater.*, **14**, 524 (2002).
- [9] K. C. Park, I. Y. Jang, W. Wongwiriyan, S. Morimoto, Y. J. Kim, Y. C. Jung, T. Toya, and M. Endo, *J. Mater. Chem.*, **20**, 5345 (2010).
- [10] H. Wang, H. Y. Jeong, M. Imura, L. Wang, L. Radhakrishnan, N. Fujita, T. Castle, O. Terasaki, and Y. Yamauchi, *J. Am. Chem. Soc.*, **133**, 14526 (2011).
- [11] Y. Kuroda, Y. Yamauchi, and K. Kuroda, *Chem. Commun.*, **46**, 1827 (2010).
- [12] H. Wang, M. Imura, Y. Nemoto, S. E. Park, and Y. Yamauchi, *Chem. Asian J.*, **7**, 802 (2012).
- [13] C. Albayrak, A. M. Soylu, and O. Dag, *Langmuir*, **24**, 10592 (2008).
- [14] C. Albayrak, G. Gulden, and O. Dag, *Langmuir*, **23**, 855 (2007).
- [15] A. F. Demirors, B. E. Eser, and O. Dag, *Langmuir*, **21**, 4156 (2005).
- [16] Y. Yamauchi, M. Komatsu, M. Fuziwara, Y. Nemoto, K. Sato, T. Yokoshima, H. Sukegawa, K. Inomata, and K. Kuroda, *Angew. Chem., Int. Ed.*, **48**, 7792 (2009).
- [17] A. Takai, Y. Yamauchi, and K. Kuroda, *J. Am. Chem. Soc.*, **132**, 208 (2010).
- [18] Y. Yamauchi, A. Sugiyama, R. Morimoto, A. Takai, and K. Kuroda, *Angew. Chem., Int. Ed.*, **47**, 5371 (2008).

- [19] H. Arora, Z. H. Li, H. Sai, M. Kamperman, S. C. Warren, and U. Wiesner, *Macromol. Rapid. Commun.*, **31**, 1960 (2010).
- [20] Z. H. Li, H. Sai, S. C. Warren, M. Kamperman, H. Arora, S. M. Gruner, and U. Wiesner, *Chem. Mater.*, **21**, 5578 (2009).
- [21] S. C. Warren, L. C. Messina, L. S. Slaughter, M. Kamperman, Q. Zhou, S. M. Gruner, F. J. DiSalvo, and U. Wiesner, *Science*, **320**, 1748 (2008).
- [22] E. S. Steigerwalt, G. A. Deluga, and C. M. Lukehart, *J. Phys. Chem. B*, **106**, 760 (2002).
- [23] Z. Liu, J. Y. Lee, M. Han, W. Chen, and L. M. Gan, *J. Mater. Chem.*, **12**, 2453 (2002).
- [24] X. Xue, C. Liu, W. Xing, and T. Lu, *J. Electrochem. Soc.*, **153**, E79 (2006).
- [25] W. X. Chen, J. Y. Lee, and Z. Liu, *Mater. Lett.*, **58**, 3166 (2004).
- [26] S. Tominaka, M. Shigeto, H. Nishizeko, and T. Osaka, *Chem. Commun.*, **46**, 8989 (2010).
- [27] J. Jiang, and A. Kucernak, *Chem. Mater.*, **16**, 1362 (2004).
- [28] H. Wang, L. Wang, T. Sato, Y. Sakamoto, S. Tominaka, K. Miyasaka, N. Miyamoto, Y. Nemoto, O. Terasaki, and Y. Yamauchi, *Chem. Mater.*, **24**, 1591 (2012).
- [29] A. X. Yin, X. Q. Min, W. Zhu, H. S. Wu, Y. W. Zhang, and C. H. Yan, *Chem. Comm.*, **48**, 543 (2011).
- [30] Z. C. Zhang, J. F. Hui, Z. G. Guo, Q. Y. Yu, B. Xu, X. Zhang, Z. C. Liu, C. M. Xu, J. S. Gao, and X. Wang, *Nanoscale*, **4**, 2633 (2012).

Chapter 8

General Conclusions and Future Perspective

8.1. Overview of My Achievement

Rational design of Pt-based catalysts is of considerable interest because of their unique catalytic properties. In view of the strong social demand, the creation of high performance Pt catalyst with low cost is extremely important. The engineering of the size, shape, and composition of Pt-based materials at nanoscale can lower the Pt loading and provide more active sites, thus favor the improved the utilization efficiency and enhanced catalytic performance. So far, several types of important Pt nanostructures (e.g., nanospheres, nanofibers, nanowires, and so on) with controlled sizes and shapes have been successfully prepared by using template or templateless routes (**Table 8.1**).

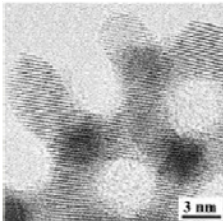
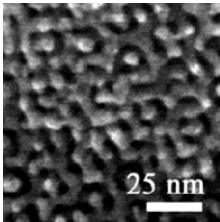
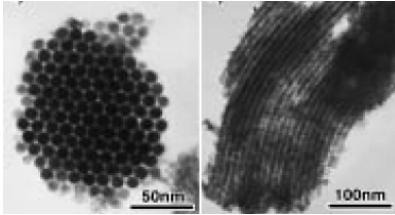
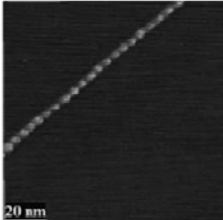
Template-less approach has been widely utilized. In almost cases, however, requisite multi-step, high reaction temperature, and long duration complicate the synthetic procedures, thus make them very difficulty to be scaled up. The development of facile and efficient strategy to produce Pt catalysts with high activity, in high yield and large quantities, is still highly desired. In general, the Pt products prepared by the template-less approach have high surface areas, but the nanopore arrangements are in random and the nanopores sizes are very broad, which is not useful for size-selective reaction.

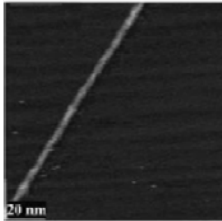
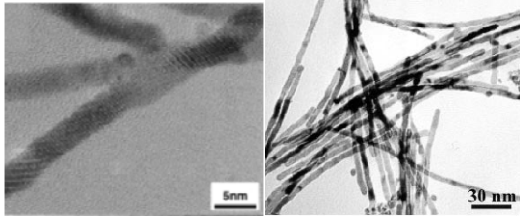
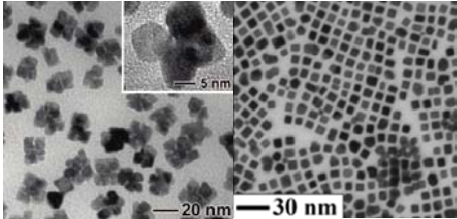
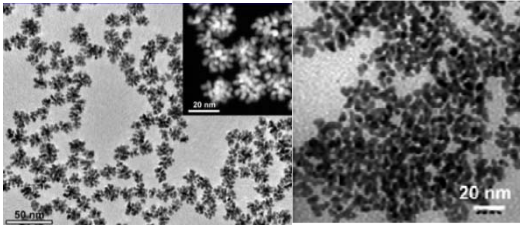
Therefore, we focused on the template approach for preparation of ordered mesoporous metals. Template approach is classified into a hard-templating method and a soft-templating method. In a hard-templating method, mesoporous silica with a robust framework and high thermal stability is used as a template to synthesize a metal replica. So far, various Pt nanostructures, such as 1D nanowires and 3D nanowire networks, have been prepared using MCM-41 (*p6mm*), SBA-15 (*p6mm*), KIT-6 (*Ia-3d*), and MCM-48 (*Ia-3d*) as hard templates. Despite those recent advances in the hard-templating method, however, the obtained morphologies of mesoporous metals have been limited to only powders with irregular morphology or films on conductive substrates. Lack of controllability of the particle sizes and morphological shapes is a serious problem for further development of mesoporous metals. The shapes and particle sizes critically determine the function and utility for applications. To bring out shape- and size-dependent physicochemical properties, it is extremely important to prepare

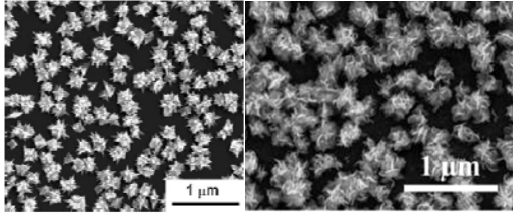
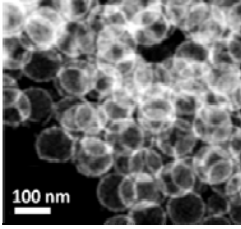
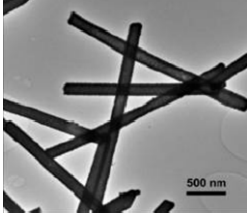
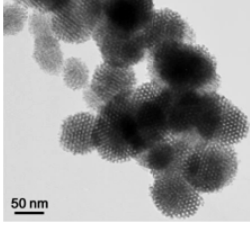
uniform-sized particles with the same shapes in high yield. In my PhD study, I have especially focused on nanoscale metal deposition behaviors inside the mesochannels. By realizing a controlled chemical reduction with appropriate reducing agent, well-defined mesoporous platinum (Pt) nanoparticles were successfully synthesized, which cannot be prepared using other means.

On the other hand, lyotropic liquid crystals made of highly concentrated surfactants or block copolymers have been utilized as a soft template. By using chemical or electrochemical reduction, ordered mesoporous metal powder or films can be respectively synthesized. However, the ordered arrangement of the rod-self assemblies in the liquid crystals is often distorted during the metal deposition process, resulting in the lack of a long-range order of mesoporous structures in the final product. In addition, the controllability of the pore sizes in mesoporous metal systems is much more limited than that in mesoporous silica systems. Therefore, the development of a highly reproducible soft-templating method is in much demand. In my PhD study, I have established new approach using extremely diluted surfactant solutions. Unlike the previous soft-templating methods, it became possible to effectively manipulate various mesopore sizes by simply changing different surfactants and adding organic expanders in the aqueous solution.

Table 8.1 Example of previous nanoporous materials.

Template	Method	Pt shape	Ref.
MCM-48	H ₂ reduction	3D network 	[1]
KIT-6	Vapor infiltration method (Dimethylaminoborane vapor)	3D network 	[2]
SBA-15	H ₂ reduction	2D hexagonally arranged nanowires 	[3]
HMM-1	Photoreduction	Necklace-like nanowires 	[4]

Template	Method	Pt shape	Ref.
FSM-16	Photoreduction	Nanowires 	[4]
MCM-41	H ₂ reduction	Nanowires 	[5],[6]
No templates	^[7] Chemical-reduction by poly(vinyl pyrrolidone) containing FeCl ₃ ^[8] Chemical-reduction by oleic acid	Cube-shaped nanoparticles 	[7],[8]
No templates	Chemical-reduction by Ascorbic Acid	Nanodendritics 	[9],[10]

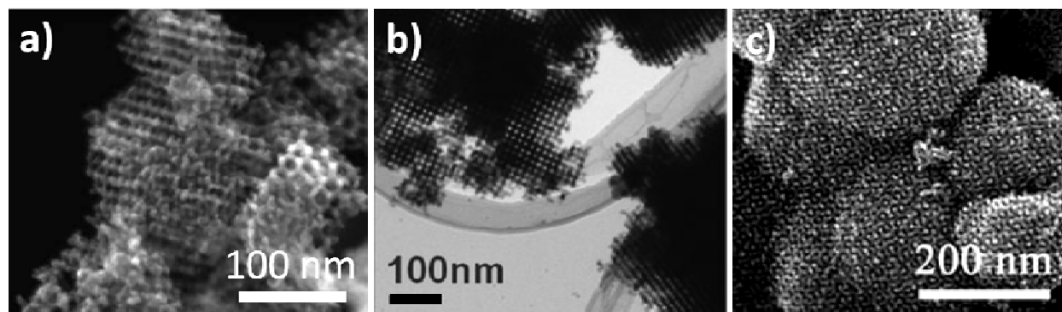
Template	Method	Pt shape	Ref.
No templates	Electro-chemical reduction	<p>Nanothorns</p> 	[11],[12]
Polystyrene beads	Photocatalytic reduction	<p>Hollow spheres</p> 	[13]
Zinc meso-tetra(4-pyridyl)porphyrin (ZnTPyP) as template	Photocatalytic reduction	<p>Nanotubes</p> 	[14]
Lyotropic liquid crystals	Chemical-reduction by DMAB vapor	<p>2D hexagonal mesoporous structure</p> 	[15]

8.2. Significant Advances in Hard-templating Method

For the previous hard-templating method, it is difficult to control the Pt deposition process inside the templates, and the shapes and particle sizes of the products are hard to be controlled. Therefore, the irregular shaped mesoporous Pt are always obtained (**Figure 8.1a-c**). In order to improve the hard-templating method, I have specially focused on the nanoscale deposition behaviors inside the mesoporous silica template. By controlling the reductive strength of the reduction agents, I have successfully synthesized monodispersed polyhedral- and olive-shaped mesoporous Pt nanoparticles with uniform particle sizes by using KIT-6 and SBA-15, respectively, as templates. (**Figure 8.1d,e**). In my approach, all of the Pt sources are introduced into the entire mesopore space and are successfully reduced inside the hard-templates without any Pt deposition outside the mesopores. The obtained particles are isolated each other and their particle-size distribution is very narrow. By further controlling the Pt reduction time, the particle sizes can be adjusted accurately. Through some comparative study, it is revealed that an appropriate reducing agent is vital for formation of mesoporous Pt nanoparticles with uniform shapes and sizes and the reaction kinetics was critical for high-quality synthesis.

Compared to the previous methods such as H₂ reduction, my method without complicated equipments is a very simple and highly reproducible route which can be highly useful for large-scale production. Well-defined morphology and uniformity in particle size will become very important aspects for the future use of mesoporous metals in a wide range of applications such as electrodes, sensors, catalysis, and drug delivery. I strongly hope that this method can provide a generic platform for the preparation of mesoporous metal nanoparticles.

Irregularly shaped mesoporous Pt by previous hard-templating method



Schuth F. *et al. J. Am. Chem. Soc.*, 2008, 9, 130.

Shon J. K. *et al. Chem. Commun.*, 2009, 650.

Doi Y. *et al. Chem. Commun.*, 2010, 46, 6365.

**Overcome
disadvantages**

Shape- and size-controlled mesoporous Pt

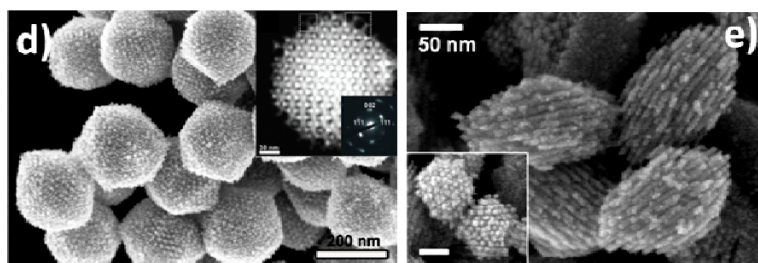


Figure 8.1 Examples of mesoporous Pt particles prepared by the hard-templating methods. (a-c) Irregularly shaped mesoporous Pt particles prepared by general hard-templating approaches. (d-e) The shape- and size-controlled mesoporous Pt particles prepared by my hard-templating method.

8.3. Significant Advances in Soft-templating Method

Lyotropic liquid crystals (LLCs) made of highly concentrated surfactants or block copolymers have been utilized as a soft template. By using chemical or electrochemical reduction, ordered mesoporous metal powder or films can be respectively synthesized. The general synthesis of mesoporous metals using LLCs is a two-step process: (1) formation of LLC and (2) reduction of metal ions in the presence of LLC. In the first stage, a large amount of surfactants is necessary to form LLC which consists of highly concentrated surfactants (normally more than 40 wt%). Ternary components (including surfactants, water, and metal species) are manually mixed, and then the mixture is heated and mixed vigorously. This process is repeated until a homogeneous mixture is obtained. LLC is thus prepared manually. In the second stage, some problems still remain. By electrochemical deposition, mesoporous metals have been generally formed as films on conductive substrate. The electrodeposition system involves a three-electrode cell consisting of a working, a reference, and a counter electrode. Mesoporous metal thin films are deposited onto conductive substrates which act as a working electrode. However, it is really difficult to set up and operate the three-electrode cell due to the high viscosity of LLC, in contrast to the conventional electrodeposition system of metals using an aqueous solution. Therefore, a new simpler and more sophisticated synthetic route is needed. So we aimed to create a procedure of synthesizing highly ordered mesoporous metals and alloys to fulfill the requirements for a wider applicability to any kinds of conductive substrates.

In contrast to the lyotropic liquid crystalline method which requires very high surfactant concentrations (over 30 wt %), as **Figure 8.2** showed, I have proposed a “electrochemical micelle assembly” approach by using diluted surfactant solutions for the preparation of flat Pt and Pt-based films with accessible pores and widely controlled the mesopore sizes by changing different surfactants and adding organic expanders. Nonionic PEO-PPO-PEO-type copolymers used in this study are good candidates as porogen of larger mesopores because of their low cost, commercial availability, and biodegradability. The mesoporous Pt films are electrodeposited by the assembly of surfactant micelles with metal species. In the plating solution, dissolved Pt ions are

coordinated by water molecules to form metal-aqua complexes, which adsorb inside the external EO region of the surfactant micelles. Therefore, during the electrochemical deposition, the Pt species are thought to move to the working electrode together with the surfactant micelles. Thus, the surfactant micelles can act as structural direct agents.

The present plating solutions can be reused several times, demonstrating high repeatability. The present process can allow easy preparation of other mesoporous Pt-based alloys, which will be important for realizing higher performance as electrodes in batteries. In Chapter 7, I extend this concept to synthesize mesoporous Pt-Pd alloy films. The Pt-Pd alloy films with various compositional ratios are successfully synthesized by changing the Pt and Pd compositional ratios in the precursor solutions. The frameworks in the obtained mesoporous films are composed of connected metal nanoparticles (around 3 nm in diameter). Interestingly, the atomic crystallinity is coherently extending across over several nanoparticles. Each nanoparticle is in an alloy state and shows a characteristic morphology with an undefined shape with higher index surface, that is, a large number of steps. Due to such unique pore walls and high effective surface areas, the obtained mesoporous films showed remarkably high catalytic activities for methanol oxidation reaction. In future, by further controlling the precursor compositions, we can realize many mesoporous alloy films with various compositions.

My soft-templating approach uses extremely diluted surfactant solutions to generate films with accessible pores and effectively manipulates different pore sizes by changing different surfactants and adding organic expanders. Such a facile electrochemical design of mesoporous metals and alloys should greatly contribute to future applications such as micro-sensors, micro-batteries, micro-bioactive materials, miniaturized devices, and beyond. Furthermore, this synthetic mechanism is expected to generate other metallic and semiconducting nanostructured films with architectures of technological importance in future.

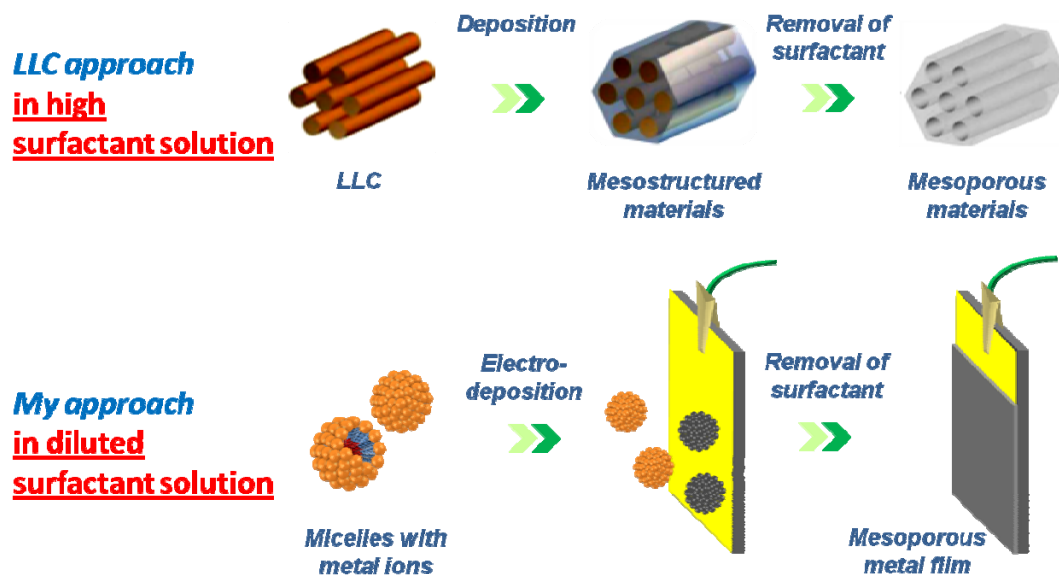


Figure 8.2 Illustration of general LLC approach and my proposed “electrochemical micelle assembly” approach.

8.4. Future Perspective

Pt is widely used as industrial catalysts and battery electrodes, due to its usefulness as a durable metal, as well as its chemical functions as catalysts in a number of reactions. In view of the strong social demand for reduced use of rare metals, I hope that my study contribute as an important technology for securing high functionality with low use of Pt by producing mesoporous structures with larger surface area.

The most common use of platinum is as a catalyst in chemical reactions. Compared with platinum black, which has been employed as catalyst since the early 19th century, the nanoscale structure endowed platinum higher surface area and more effective utilization. Fuel cell technology is widely believed to play a key role in the next generation of generation of environmentally friendly energy solutions. Over the past decade there has been significant progress towards meeting the performance and cost targets required for commercialization of proton exchange membrane fuel cells (PEMFCs). One major technical challenge in PEMFCs technology is the development of improved anode and cathode catalysts. The current industry catalyst for PEMFC is Pt nanoparticles. The activity of the catalyst is increased with an increasing specific surface area because the chemical reaction of the fuel cell takes place on the surface of the catalyst. By increasing the surface area and controlling the morphology of the nanostructured Pt materials, I hope to design novel nanoporous materials as catalysts for high-performance fuel cells. For instance, the shape- and size- controlled mesoporous Pt nanoparticles with high surface area showed much enhanced catalytic activity in methanol oxidation reaction compared with commercial Pt black.

The development of bi-metallic Pt alloys is an effective way to further improvement in specific and mass activities, and stability of the catalysts. Except the synthesis of mesoporous Pt-Pd alloy film (chapter 7), the mentioned soft-templating approach can be extend to synthesis extensive flat mesoporous Pt-based alloys films, such as Pt-Ru. Except the traditional Pt-based alloy films, currently I am trying to fabricate multi-layered mesoporous Pt/Pd films in the diluted surfactant system by utilizing “Layer-by-layer (LbL)” approach. “Layer-by-layer (LbL)” route has been

widely demonstrated for the fabrication of nanometer-level layered structures in a designable manner. The high versatility of the LbL approach has resulted in the proposal of different formation mechanisms by utilizing various interactions as well as chemical reactions [15]. In the LbL films, the fuzzy nature of the structural formation provides rather disordered interfacial structures, which is advantageous for a chemical process based on interlayer molecular diffusion, however, it is a serious problem for the formation of neat interfacial structures, such as the atomic-level contact necessary for enhanced interlayer electrical communication.

“All metal mesoporous LbL films” fabricated by electro-deposited in diluted surfactant system (**Figure 8.3**) can overcome this disadvantage in the typical LbL technology, because of both atomic-level interlayer metal-to-metal contact and facile diffusion through the mesopores in the films. Pt/Pd bimetallic alternate layers with mesopores are fabricated by combining two concepts: the LbL approach and the electrochemical deposition method. Based on the former research in chapter 6 and 7, the thickness of each layer of mesoporous Pt and Pd can be altered by simply controlling the applied deposition time due to the linearity between the deposition time and the deposition thickness of the Pt and Pd layers. The synergistic effect of the high surface area and accessible Pt/Pd hetero-interface can endow the multi-layered mesoporous films an enhanced catalytic activity in the future applications. And this synthetic concept can be applied to more complicated multi-layered mesoporous films with various metal and alloy layers. I hope that such films can be new types of integrated sensors, sequential reactors as well as electrocatalysts in future.

Currently, one of the most important applications of platinum is in automobiles as a catalytic converter. A catalytic converter is an exhaust emission control device which converts toxic chemicals in the exhaust of an internal combustion engine into less toxic substances. The role of platinum in catalytic converters is to oxidize carbon monoxide (CO) and hydrocarbons. Platinum is particularly effective at this under oxygen-excessive conditions, so is often the metal of choice for diesel applications. Compared with platinum black, our well-defined mesoporous Pt nanoparticles have afforded higher surface area and effectively avoided aggregation. And, the single crystalline nature endowed the as-prepared mesoporous Pt nanoparticles higher thermal stability.

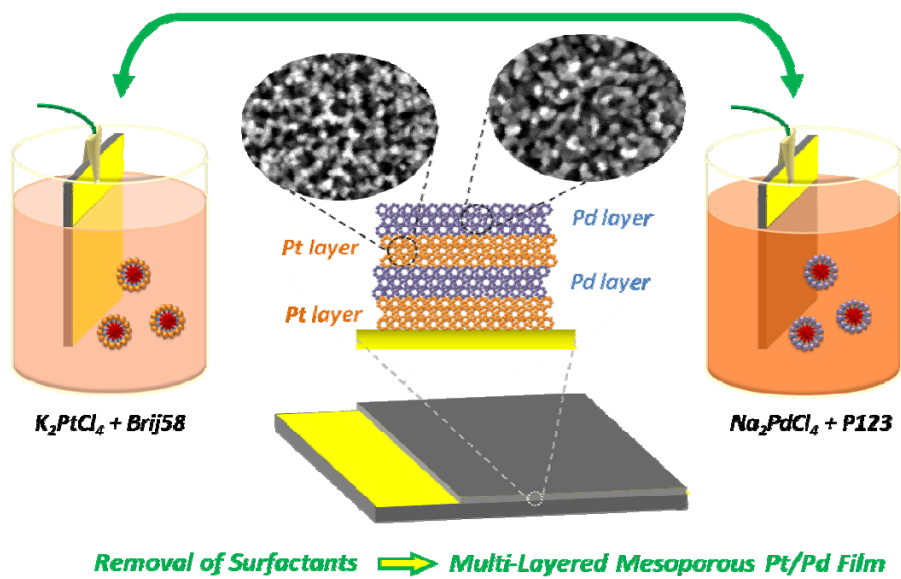


Figure 8.3 Procedure for multi-layered mesoporous Pt/Pd films by electrochemical deposition.

References

- [1] H. J. Shin, R. Ryoo, Z. Liu, and O. Terasaki, *J. Mater. Chem.*, **15**, 1560 (2005).
- [2] Z. Liu, O. Terasaki, T. Ohsuna, K. Hiraga, H. J. Shin, and R. Ryoo, *Chem. Phys. Chem.*, **2**, 229 (2001).
- [3] Y. Doi, A. Takai, Y. Sakamoto, O. Terasaki, Y. Yamauchi, and K. Kuroda, *Chem. Commun.*, **46**, 6365 (2010).
- [4] Y. Sakamoto, A. Fukuoka, T. Higuchi, N. Shimomura, S. Inagaki, and M. Ichikawa, *J. Phys. Chem. B*, **108**, 853 (2004).
- [5] Z. Liu, Y. Sakamoto, T. Ohsuna, K. Hiraga, O. Terasaki, C. H. Ko, H. J. Shin, and R. Ryoo, *Angew. Chem. Int. Ed.*, **39**, 3107 (2000).
- [6] H. J. Shin, C. H. Ko, and R. Ryoo, *J. Mater. Chem.*, **11**, 260 (2011).
- [7] B. Lim, X. Lu, M. Jiang, P. H. C. Camargo, E. C. Cho, E. P. Lee, and Y. Xia, *Nano Lett.*, **8**, 4043 (2008).
- [8] R. Loukrakpam, P. Chang, J. Luo, B. Fang, D. Mott, I. T. Bae, H. R. Naslund, M. H. Engelhard, and C. J. Zhong, *Chem. Commun.*, **46**, 7184 (2010).
- [9] L. Wang, and Y. Yamauchi, *J. Am. Chem. Soc.*, **131**, 9152 (2009).
- [10] A. Mohanty, N. Garg, and R. Jin, *Angew. Chem. Int. Ed.*, **49**, 4962 (2010).
- [11] N. Tian, Z. Y. Zhou, S. G. Sun, L. Cui, B. Ren, and Z. Q. Tian, *Chem. Commun.*, 4090 (2006).
- [12] L. Su, W. Jia, L. Zhang, C. Beacham, H. Zhang, and Y. Lei, *J. Phys. Chem. C*, **114**, 18121 (2010).
- [13] R. M. Garcia, Y. Song, R. M. Dorin, H. Wang, P. Li, Y. Qiu, F. Swol, and J. A. Shelnutt, *Chem. Commun.*, 2535 (2008).

- [14] F. Bai, Z. Sun, H. Wu, R. E. Haddad, X. Xiao, and H. Fan, *Nano Lett.*, **11**, 3759 (2011).
- [15] Y. Yamauchi, A. Takai, M. Komatsu, M. Sawada, T. Ohsuna, and K. Kuroda, *Chem. Mater.*, **20**, 1004 (2008).

List of Publications

1. Original papers

- 1) Electrochemical Synthesis of Mesoporous Pt-Ru Alloy Films as Superior Electrocatalysts
Chemistry-A European Journal, **2012**, Accepted.
Hongjing Wang and Yusuke Yamauchi*

- 2) All Metal Layer-by-Layer Films: Bimetallic Alternate Layers with Accessible Mesopores for Enhanced Electrocatalysis
Journal of the American Chemical Society, **2012**, DOI: 10.1021/ja303773z. (June 20, 2012).
Hongjing Wang, Katsuhiko Ariga, and Yusuke Yamauchi*

- 3) Synthesis of Mesoporous Pt-Pd Alloy Films by Electrochemical Plating in Aqueous Surfactant Solutions
Chemistry-An Asian Journal, **2012**, DOI: 10.1002/asia.201200316. (June 25, 2012).
Hongjing Wang and Yusuke Yamauchi*

- 4) Synthesis of Mesoporous Pt Films with Tunable Pore Sizes from Aqueous Surfactant Solutions
Chemistry of Materials, **2012**, 24, 1591-1598. (April 23, 2012)
Hongjing Wang, Liang Wang, Takaaki Sato, Yasuhiro, Sakamoto, Satoshi Tominaka, Keiichi Miyasaka, Nobuyoshi Miyamoto, Yoshihiro Nemoto, Osamu Terasaki, and Yusuke Yamauchi*

- 5) Electrochemical Synthesis of Mesoporous Pt-Au Binary Alloys with Tunable Compositions for Enhancement of Electrochemical Performance

Journal of the American Chemical Society, **2012**, 134, 5100-5109. (February 21, 2012)

Yusuke Yamauchi*, Akihisa Tonegawa, Masaki Komatsu, Hongjing Wang, Liang Wang, Yoshihiro Nemoto, Norihiro Suzuki and Kazuyuki Kuroda*

- 6) Synthesis of Olive-Shaped Mesoporous Platinum Nanoparticles (MPNs) with a Hard-Templating Method Using Mesoporous Silica (SBA-15)
Chemistry-An Asian Journal, **2012**, 7, 802-808. (February 1, 2012)
Hongjing Wang, Masataka Imura, Yoshihiro Nemoto, Sang-Eon Park, and Yusuke Yamauchi*

- 7) Shape- and Size-Controlled Synthesis in Hard Templates: Sophisticated Chemical Reduction for Mesoporous Monocrystalline Platinum Nanoparticles
Journal of the American Chemical Society, **2011**, 133, 14526-14529. (August 30, 2011)
Hongjing Wang, Hu Young Jeong, Masataka Imura, Liang Wang, Logudurai Radhakrishnan, Nobuhisa Fujita, Toen Castle, Osamu Terasaki, and Yusuke Yamacuhi*

- 8) Direct Synthesis of Nanoporous Carbon Nitride Fibers Using Al-based Porous Coordination Polymers (Al-PCPs)
Chemical Communications, **2011**, 47, 8124-8126. (June 20, 2011)
Ming Hu, Julien Reboul, Shuhei Furukawa, Logudurai Radhakrishnan, Yuanjian Zhang, Pavuluri Srinivasu, Hideo Iwai, Hongjing Wang, Yoshihiro Nemoto, Norihiro Suzuki, Susumu Kitagawa, Yusuke Yamauchi*

- 9) Mesoporous Co₃O₄ for Low Temperature CO Oxidation: Effect of Calcination Temperatures on Their Catalytic Performance
Journal of Nanoscience and Nanotechnology, **2011**, 11, 3843-3850. (May 1, 2011)
Hongjing Wang, Yonghong Teng, Logudurai Radhakrishnan, Nemoto Yoshihiro, Imura Masataka, Shimakawa Yuichi, and Yusuke Yamauchi*

- 10) Microwave-assisted Rapid Synthesis of Platinum Nanoclusters with High Surface Area
Journal of Nanoscience and Nanotechnology, **2010**, 10, 6489-6494. (October 1, 2010)
Hongjing Wang, Liang Wang, Yoshihiro Nemoto, Norihiro Suzuki, and Yusuke Yamauchi*

- 11) A High-Speed Passive-Matrix Electrochromic Display Using a Mesoporous TiO₂ Electrode with Vertical Porosity
Angewandte Chemie-International Edition, **2010**, 49, 3956-3959. (April 21, 2010)
Wu Weng, Tetsuya Higuchi, Masao Suzuki, Toshimi Fukuoka, Takeshi Shimomura, Masotoshi Ono, Logudurai Radhakrishnan, Hongjing Wang, Norihiro Suzuki, Hamid Oveisi, and Yusuke Yamauchi*

- 12) Precise Manipulation of One-Dimensional Mesochannel Alignments in Mesoporous Silica Films by Novel Rubbing Method Utilizing Lyotropic Liquid Crystals
Chemistry-An Asian Journal, **2010**, 5, 1290-1293. (April 8, 2010)
Logudurai Radhakrishnan, Hongjing Wang, and Yusuke Yamauchi*

- 13) Rapid and Efficient Synthesis of Platinum Nanodendrites with High Surface Area by Chemical Reduction with Formic Acid
Chemistry of Materials, **2010**, 22, 2835-2841. (March 25, 2010)
Liang Wang, Hongjing Wang, Yoshihiro Nemoto, and Yusuke Yamauchi*

2. Books

- 1) Chapter 6: Synthesis of Mesoporous Metal Oxides and Metals and Their Applications

“Nanoporous Materials: Synthesis and Applications (Taylor & Francis Group)”

(To be published in December, 2012)

Hongjing Wang, Xiangfen Jiang, and Yusuke Yamauchi

3. Oral & Poster presentations in Conferences/Symposiums

- 1) Design of Mesoporous Pt with Superior Electrocatalytic Activity (口頭発表)
第27回ゼオライト研究発表会, 大阪, 日本 (2011年12月1-2日)
Hongjing Wang, Hamed Atae-Esfahani, Masataka Imura, Liang Wang, Yoshihiro Nemoto, and Yusuke Yamauchi

- 2) Shape- and Size-Controlled Synthesis in Hard Templates: Sophisticated Chemical Reduction for Mesoporous Monocrystalline Pt Nanoparticles (Poster presentation)
The 3rd NIMS-Waseda International Symposium, Tokyo, Japan (November 1, 2011)
Hongjing Wang, and Yusuke Yamauchi

- 3) Mesoporous Co_3O_4 for Low Temperature CO Oxidation: Effect of Calcination Temperatures on Their Catalytic Performance (Poster presentation)
International Symposium on Photocatalysis and Environmental remediation materials, Tsukuba, Japan (January 17-19, 2011)
Hongjing Wang, and Yusuke Yamauchi

- 4) Mesoporous Co_3O_4 for Low Temperature CO Oxidation: Effect of Calcination Temperatures on Their Catalytic Performance (Poster presentation)
The 2nd NIMS-Waseda International Symposium, Tsukuba, Japan (December 1, 2010)
Hongjing Wang, Logudurai Radhakrishnan, and Yusuke Yamauchi

- 5) Rubbing Method for Mesoporous Silica Films with Uniaxially Oriented Mesochannels Based on Lyotropic Liquid Crystal Approach (Poster presentation)
JSPS A3 Foresight Seminar: Present Status and Future Prospects of Mesoporous Materials, Tokyo, Japan (September 3, 2010)
Hongjing Wang, Logudurai Radhakrishnan, and Yusuke Yamauchi

- 6) New Rubbing Method for Mesoporous Silica Films with Uniaxially Oriented Mesochannels Based on Lyotropic Liquid Crystal Approach (Poster presentation)
The 4th Global COE International Symposium on 'Practical Chemical Wisdom',
Tokyo, Japan. (January 14, 2010)
Hongjing Wang, Logudurai Radhakrishnan, and Yusuke Yamauchi

ACKNOWLEDGEMENTS

All these years of study and research at NIMS and Waseda University have been a wonderful and memorable life experience for me. I would like to take this opportunity to thank the people who helped me to make this happen.

First and foremost, I would like to express my deepest gratitude and appreciation to my supervisor, Prof. Yusuke Yamauchi, for his invaluable guidance and advices. None of the work in this thesis could have been carried out successfully without his guidance. Prof. Yamauchi set an example of excellence and integrity in science. I am fascinated by his enthusiasm for work and continuous efforts in scientific exploration. As a supervisor, he has taught me not only the vast knowledge in mesoporous materials, but also the way to try my best to complete a task.

I greatly appreciate Prof. Kazuyuki Kuroda, Prof. Toshiyuki Momma and Prof. Tetsuya Osaka, for their encouragements, advices and generous supporting. Their inspiring suggestions and critical comments during my dissertation research helped to make this thesis more profound and consistent in a scientific way. During I had a chance to learn in Prof. Kuroda lab, Dr. Azusa Takai and other students gave me a lot of help. I really would like to thank them for the kind help and experimental support.

I am grateful to Prof. Osamu Terasaki (Stockholm University) for his valuable guidance and helpful advices. And I would like to thank Dr. Hu Young Jeong, for his TEM measurement support.

I am deeply grateful to Prof. Yoshio Bando and Prof. Toyohiro Chikyo, and I highly appreciate the support from NIMS- Waseda University Joint Graduate Program.

I would like to thank all of Dr. Yamauchi's group members, Dr. Norihiro Suzuki for kindly help on my experiments, Dr. Logudurai Radhakrishnan for discussion of the results and inspired me to think more about the experiments, Dr. Hu Ming, Dr. Bishnu Bastakoti, Ms. Kimiko Takai, Miss. Xiangfen Jiang, Mr. Hamed Atae-Esfahani, Mr. Nagy L. Kamal, Dr. Taketoshi Fujita, and Mr. Yuichiro Kamachi, for their kindly help and tremendously supportive during out shared time in the lab.

I also want to give my deeply appreciate to Ms. Aki Futaesaku, Ms. Hiroko Komura, and Ms. Akemi Tateno, for their meticulous care during the past three years. And I also would like to thank all NIMS staffs for their kind help and supports in my life.

I would like to express my deepest gratitude and appreciation to my husband and my parents for their enduring love, encouragement and support during the past years when I am far away from home.

Finally, I would like to acknowledge gratefully the Waseda University for their financial support.

Hongjing Wang